Dynamics of European two–axle freight wagons

Mark Hoffmann

Kongens Lyngby 2006
IMM-PHD-2006-170

Technical University of Denmark
Informatics and Mathematical Modelling
Building 321, DK-2800 Kongens Lyngby, Denmark
Phone +45 45253351, Fax +45 45882673
reception@imm.dtu.dk
www.imm.dtu.dk

IMM-PHD: ISSN 0909-3192

Preface

This thesis is submitted to the department of Informatics and Mathematical Modelling at the Technical University of Denmark in partial fulfilment of the requirements of the Ph.D. degree. The project has been supervised by Ph.D. Hans True, Docent Per Grove Thomsen and Associate Professor Mads Peter Sørensen.

My gratitude goes to all who have contributed to this project. In particular, Hans True has been very inspiring for the research through his incredible knowhow in railway dynamics. His guiding and constructive feedback during the progress of the project is highly appreciated. Also, Per Grove Thomsen has been a tremendous help by teaching me how to simulate discontinuous dynamical systems. Our many discussions on important aspects of numerical integration have truly been beneficial for my research. Further, I am thankful to Prof. J. Piotrowski and Ph.D. A. Grzelak from the Warsaw University of Technology, Poland, for letting me investigate the mechanical characteristics of the UIC link suspension at their department. I would also like to thank Dr. H. Chollet and the railway group at INRETS, France, for sharing their deep understanding on modelling rail vehicles.

Kgs. Lyngby, September 2006

Mark Hoffmann

Summary

In this thesis the fundamental dynamic behaviour of European two–axle railway freight wagons is investigated with special attention to their unwanted hunting motion on straight track. A model of a single two–axle freight wagon running on a general curvilinear track is developed and described in detail. Essentially, the model is a system of ordinary differential equations. The nonsmooth characteristics of the interacting forces are challenging both in the modelling phase as well as in the formulation of an appropriate numerical integration strategy to extract the solution from the system of differential equations. The model is appropriately divided into states, such that the nonsmoothness in the model is defined by the switching boundaries between the states. These switching boundaries are located by the numerical integration procedure allowing one to find the solution efficiently and accurately.

The model is analysed for different parameters (wheelbase, suspension parameters, rail inclination etc.). The solution space is shown to have several attractors emphasising the intricate dynamic properties of these wagons. In summary, if the wagon is running at high speed the wheelsets are attracted to a flange–to–flange motion. This violent motion is not transferred to the carbody if the lateral excitation frequency of the wheelsets is far from the yaw eigenfrequency of the carbody. However, the two–axle freight wagon can experience a resonance motion at either low, medium or high speed when the previously mentioned frequencies coincide. Here, the wheelsets are not necessarily moving from flange to flange but the carbody has a severe lateral and yaw motion.

Resumé

I denne afhandling undersøges den grundlæggende dynamiske opførsel af europæiske to–akslet godsvogne med fokus på deres uønskede hunting bevægelse på lige spor. En model af en enkelt to–akslet godsvogn kørende på et generelt curvilineært spor er udviklet og detaljeret beskrevet. I bund og grund er modellen et system af sædvanlige differentialligninger. De ikke–glatte karakteristikker af de påvirkende kræfter er både udfordrende i modelleringsfasen, samt i formuleringen af en passende numerisk integrationsstrategi til at uddrage løsningen af differentialligningssystemet. Modellen er på passende vis inddelt i tilstande, således at modellens ikke–glatheder er defineret ved grænserne mellem tilstandene. Disse grænser lokaliseres af den numeriske løsningsprocedure, hvilket giver én mulighed for at finde løsningen effektivt og præcist.

Modellen er analyseret for forskellige parametre (akselafstand, affjedringsparametre, sporhældning etc.). Løsningsrummet vises at have flere attraktorer, hvilket understreger de kompliceret dynamiske egenskaber ved disse vogne. Sammenfattet kan det siges, hvis vognen kører med høj fart tiltrækkes hjulsættene af en flange–til–flange bevægelse. Denne voldsomme bevægelse overføres ikke til vognkassen, hvis den laterale påvirkningsfrekvens af hjulsættene er langt fra yaw egenfrekvensen af vognkassen. Dog er det muligt for den to–akslet godsvogn at komme ud for en resonansbevægelse ved enten lav, moderat eller høj hastighed, når de førnævnte frekvenser falder sammen. Her vil hjulsættene ikke nødvendigvis bevæge sig fra flange til flange, men vognkassen har en voldsom lateral og yaw bevægelse.

Contents

Chapter 1

Introduction

1.1 Project background

Transporting goods along railways has been done for many years. Even the ancient Greeks used railways in order to transport boats across the Corinth isthmus[1] in Greece in the 6th century [69]. The valuable principle of rail transport reappeared in Europe in the 16th century. Horse–drawn wagonways operating with wooden tracks were used in order to transport ore and coal from mines. The advent of the steam locomotive in 1804 made the benefits of rail transport even greater, and through the industrialisation in the 19th century the advantages of rail transport became evident worldwide. Today's rail transport still provides an economic and flexible solution to the task of land transport – both for goods and passengers. However, the increased competition from air travel and trucks continuously requires an increased payload and travelling speed on modern freight wagons. To fulfil this demand, it is necessary to ensure that the running properties still are satisfactory under these conditions. The maximum axle load on all main railway lines in Europe is 22.5 tonnes, and the maximum speed is generally 100 km/h.

The design of European freight wagons falls into three categories: 1) Two–axle freight wagons equipped with the single–axle running gear using leaf springs and double–links, Figure 1.1 and Figure 1.2. 2) Wagons having two–axle bogies with leaf springs and single–links, Figure 1.3. 3) Wagons having two–axle bogies with coil springs and friction dampers, Figure 1.4. These three designs are

[1] A narrow strip of land that is bordered on two sides by water and connects two larger land masses.

approved by the international union of railways, UIC[2]. The design of the running gear used on two–axle freight wagons became a standard in Germany in 1890 and has since then been widely used both in Europe and Japan because it is simple, cheap and robust. However, despite the simple design, the running properties of the two–axle freight wagons are highly complex and difficult to understand due to dry friction damping and motion delimiters causing impacts. Many of these wagons are likely to perform a hunting motion (lateral oscillations in the track) even at moderate speeds. This motion is unwanted and should be avoided because the goods might be damaged, and maintenance costs increase due to additional wear on the wheels and rails. A thorough analysis of the fundamental running properties of the two–axle freight wagons is the task of this thesis, and the bogie construction will not be further discussed. A picture of a typical two–axle freight wagon is shown in Figure 1.1.

Figure 1.1: A two–axle freight wagon.

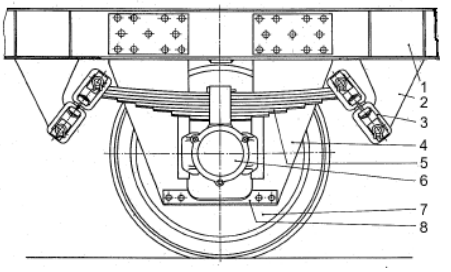

Figure 1.2: The single–axle running gear used on two–axle freight wagons. 1) Carbody 2) Suspension bracket 3) UIC links 4) Axle guidance 5) Leaf spring 6) Axle bearing 7) Wheelset 8) Connecting bar.

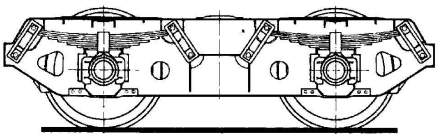

Figure 1.3: G70 bogie.

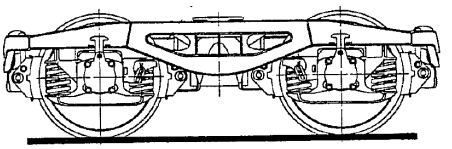

Figure 1.4: Y25 bogie.

The standard suspension system for two–axle freight wagons is called the UIC standard suspension, see Figure 1.2. Each wagon has four of these suspensions. They consist of a leaf spring and linkages. The linkages will be referred to as the UIC links. The leaf spring rests on the axle box and provides the vertical suspension. The deflection of the leaves yields the stiffness, and dissipative dry friction forces are generated in between the leaves. The carbody is connected

[2]Union internationale des chemins de fer.

with the leaf spring through the UIC links. The system of links works as a pendular suspension system with friction in the joints and they provide the horizontal suspension. The damping mechanism is solely provided by dry friction. The lateral suspension stiffness is stepwise progressive due to a clearance of 10 mm between the lower link and the suspension bracket. The pendulum length is immediately halved when this clearance is exceeded. The axle guidance restricts the relative motion between the wheelset and carbody by a simple end stop. The clearance is 22.5 mm in the longitudinal direction and 20.0 mm in the lateral direction. If one of these clearances is exceeded an impact occurs between the axle box and axle guidance. The elastic response from the axle guidance is relatively soft in the lateral direction because the axle guidance bends, and thus the overall effect is like an additional suspension stiffness. However, in the longitudinal direction the impacts are almost completely elastic due to the construction of the axle guidance.

The double–link suspension system was introduced to improve the curving performance of the two–axle freight wagons. The relatively soft horizontal suspension gives the wheelsets a larger freedom and they are more likely to position themselves radially in curves, which in general reduces wear. Moreover, the double–link suspension is used in order to have an overcritical running gear. The idea of the overcritical running gear is to avoid resonance, between the lateral excitation frequency of the wheelsets and eigenfrequencies of the carbody, in the operating speed range $60 - 120$ km/h. Instead, the resonance behaviour occurs at $35 - 40$ km/h, which makes the running properties in the operating speed range quite good [9].

To understand the fundamental running behaviour of two–axle freight wagons a mathematical model is developed. The model is a rigid multibody model having one carbody, two wheelsets and two rails, see Figure 1.5. The bodies are interconnected by forces from the UIC standard suspension and the wheel–rail contact forces.

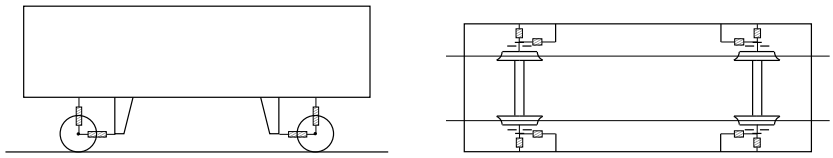

Figure 1.5: Two–axle freight wagon model.

The scientific challenge in building this model is the fact that all interacting forces are nonsmooth. The wheel–rail contact parameters (position of contact point, contact angle, size of contact patch etc.) needed in the computation of the contact forces are discontinuous functions of the lateral displacement of the wheelset for the standard wheel–rail profiles, S1002/UIC60, used in Europe.

The force–displacement characteristics of leaf springs are nonsmooth due to its dry friction damping. The forces from the horizontal suspension, governed by the UIC links, are nonsmooth due to rolling/sliding transitions and the effect of the clearance between the lower link and the suspension bracket. The impacts generated as a consequence of the axle guidance have nonsmooth characteristics as well.

So, even though the basic design of these two–axle freight wagons has been known and used for over 100 years it has eluded a thorough theoretical understanding of the fundamental behaviour, because of the complexity of the interacting forces. Moreover, simplified linear investigations of such a system have limited interest since they can not reveal anything about the existence and stability of nontrivial solutions but only the stationary solution in the centre of the track. This might lead to the following false conclusions:

- Say that the stationary solution for a given vehicle is stable until 160 km/h and that a periodic attractor exists for speeds higher than 70 km/h. From a linear analysis it is concluded that the vehicle has good running properties until 160 km/h – even though there is no guarantee about the good running properties in the speed range $70 - 160$ km/h.

- Say that a freight wagon with overcritical running gear is investigated through a linear analysis. The conclusion is that the running properties are bad for speeds higher than e.g. 35 km/h, however, due to the overcritical design the running properties are actually acceptable in the operating speed range.

In this thesis, the equilibrium states of the fully nonlinear model of a two–axle freight wagon are investigated w.r.t. uniqueness and stability in the low frequency range (below 10 Hz). The main tools in this analysis are bifurcation diagrams and time series because they do not rely on simplified approximations. The analysis is carried out for different model parameters (wheelbase, suspension parameters, rail inclination etc.) in order to clarify their sensitivity. The focus is on the motion of the wagon on a straight and level track without irregularities.

1.2 Literature review

Rail vehicles in general have been analysed theoretically for many years, and the literature on modelling rail vehicles is extensive. The books [15, 1, 103, 44, 9] each cover many fundamental as well as advanced aspects useful in any analysis of rail vehicles. The importance of the nonlinearities existing in rail vehicle models has been known and emphasised in many research studies since the 1980s, see e.g. [94, 96, 65, 38].

The research on two–axle freight wagons is less extensive due to their complex suspension system. Kämpfe [48] investigated the running properties of

a two–axle freight wagon in his thesis from 1960 using an analogue computer implementation of his model. The suspension characteristics are linearised. He finds that the motion of the wagon is sensitive to the damping in the suspension. Stichel's research on two–axle freight wagons illustrates some interesting properties of these wagons. In [80, 81] he explains the possibility of resonance between the kinematic hunting of the wheelsets and the yaw eigenmode of the carbody. The running properties of the wagon are found to be sensitive to the suspension characteristics, and it is concluded that viscous dampers might be necessary in order to achieve adequate running properties for wagons running above 130 km/h. Stichel has also observed that two–axle wagons might behave chaotically [84], and that the structural flexibility for open–sided wagons can have modes under 10 Hz influencing the running properties [83]. Piotrowski [61] has developed a model applicable for simulating the dynamics of the UIC links assuming a cylindrical (nominal) geometry of the link elements. It takes into account the nonsmooth rolling/sliding transitions present in the links during operation. A measurement method for determining the mechanical characteristics of the UIC link suspension has also been developed by Piotrowski [62]. Jönsson has in his thesis [36], that contains experimental and theoretical studies, investigated the influence of wear in the UIC links. He finds in his measurements that the rolling stiffness normally increases with wear and that new links often exhibit a very low amount of energy dissipation. He also suggests an improved design with supplementary hydraulic dampers and illustrates the improved running behaviour through simulations in the multibody simulation program GENSYS. In the thesis by Grzelak [20] the influence of wear in the link elements is also studied. He presents a sophisticated model able to take into account the real link geometry, and he finds that wear influences the stability of the stationary solution. Other research confirms the complicated running properties of two–axle wagons, see e.g. [57, 85]. Little attention is often put into the modelling of the leaf spring because the bad running properties typically find expression through lateral oscillations. However, the vertical suspension properties can influence the lateral motion of the wagon through nonlinear couplings. The work by Fancher *et al* [14] thoroughly investigates the nonlinear force–displacement characteristics and the special hysteresis damping found in leaf springs. They also present a model that can be used in order to simulate the characteristics. Derailment of freight wagons is analysed in the thesis by Lee [49]. It is emphasised that a nonlinear modelling of the leaf spring characteristics is necessary in order to get reliable results. Further details on leaf springs can be found in [7, 71].

Nonsmooth dynamical systems have been a very active research area in the last two decades. Methods are now available to analyse nonsmooth multibody systems with dry friction and impacts. Investigating unilateral contacts in terms of complementarity problems results in the elegant theory by Pfeiffer and Glocker [60, 17]. Even simple nonsmooth systems often have interesting and complex bifurcation patterns. Some modern techniques helpful in the analysis of

bifurcations in nonsmooth systems can be found in the literature [4, 10, 50, 46].

Often classical numerical integration schemes can not be applied to integrate nonsmooth systems because the basic requirements regarding the existence and continuity of the derivatives of the system are violated. Two approaches are typically found in the literature to solve this problem: 1) Event–driven methods are based on a piecewise integration procedure where each smooth section of the system is treated separately. It requires a routine that can locate the nonsmooth instants (events) during simulation, see [4, 18, 19, 77, 91, 101, 45]. 2) Time–stepping methods use velocity updates instead of accelerations in the progress of the numerical solution. As a result of this, the mechanical system does not have to be divided into different smooth states. The procedure normally requires small time steps, however, it has proved to be a valuable tool in simulating systems with many unilateral constraints, [52, 87].

1.3 Motivating example

A simple single degree of freedom system is used in order to illustrate some of the aspects needed in the modelling of the two–axle freight wagon. Consider the impact oscillator in Figure 1.6. The freight wagon analogue is a suspended axle box moving in between the axle guidance (the wall).

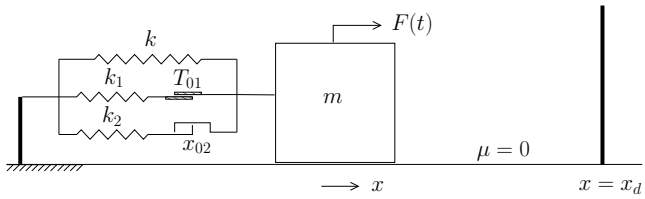

Figure 1.6: Mechanical system.

The motion of the mass is determined from

$$m\ddot{x} = -kx + F_1 + F_2 + F(t) \qquad x < x_d \quad , \quad t \geq 0 \tag{1.1}$$

where F_1 is the force from the elastic dry friction element, F_2 is the force from the dead band spring and $F(t) = A\cos(\omega t)$ is an outer harmonic excitation force. The friction slider obeys Coulomb's friction law, and the force F_1 is found through the state dependent differential equation (1.2). The state transitions are governed by the state machine in Figure (1.7). The force from the dead band spring is found by the state dependent formulation in equation (1.3) together with the state machine in Figure 1.8. The wall at $x = x_d$ is incorporated using Newton's impact law, that is $\dot{x}^+ = -\epsilon\dot{x}^-$, and the state machine for this element

is shown in Figure 1.9.

$$\dot{F}_1 = \begin{cases} -k_1\dot{x} & \text{Stick} \\ 0 & \text{SlidePos/SlideNeg} \end{cases} \tag{1.2}$$

$$F_2 = \begin{cases} 0 & \text{Idle} \\ -k_2(x - x_{02}) & \text{SpringPos} \\ -k_2(x + x_{02}) & \text{SpringNeg} \end{cases} \tag{1.3}$$

The event–driven integration strategy is used in order to integrate the equations of motion. The state partitioning of the interacting forces is necessary in order to avoid integrating across the nonsmooth points. The switching boundaries are located during simulation, and the state changes are made according to the state machines.

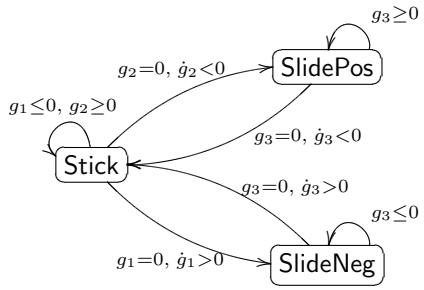

Figure 1.7: Dry friction element.

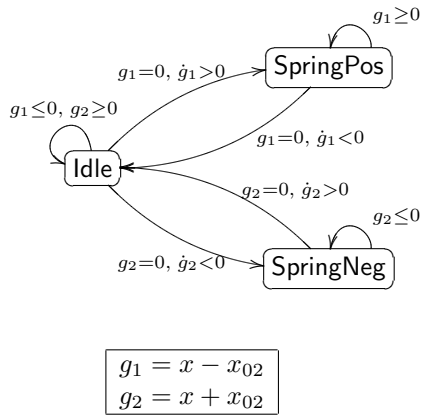

Figure 1.8: Dead band spring.

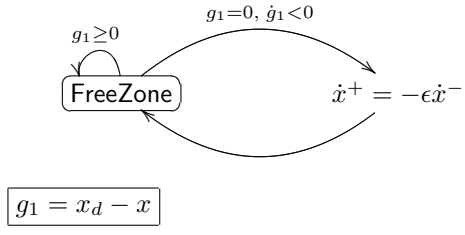

Figure 1.9: Wall.

It is noted that an impact can cause a state shift for the elastic dry friction element because the mass' velocity is reversed. Thus, it is necessary to perform

a consistency check of the current state of the elastic dry friction element after an impact. This check is done according to Algorithm 1.

if IMPACT **then**
  if (SlidePos $\wedge$ $\dot{x}^+ < 0$) $\vee$ (SlideNeg $\wedge$ $\dot{x}^+ > 0$) **then**
    State of elastic dry friction element $\leftarrow$ Stick
  end if
end if

Algorithm 1: Consistency check regarding the elastic dry friction element after an impact.

Results from a numerical simulation are illustrated in Figure 1.10 and 1.11. Further details on the simulation parameters are found in Appendix B.1. The motion of the mass is clearly restricted by the wall ($x_d = 0.02$ m), and the nonsmooth characteristics of the suspension force are illustrated by the hysteresis loop in Figure 1.11. The event–driven method assures that the force characteristics really are nonsmooth, i.e. the corners are not smoothed or rounded, and that the integration method still is efficient and accurate.

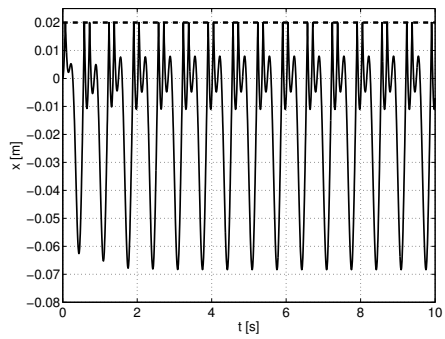

Figure 1.10: Displacement history.

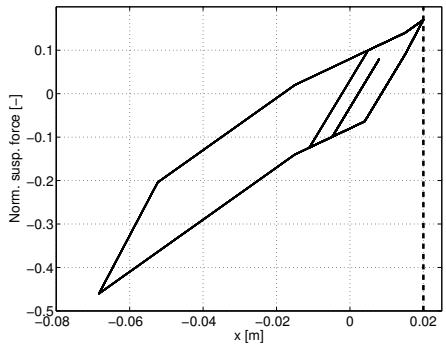

Figure 1.11: Hysteresis loop.

To emphasise the importance of locating the events consider the simulated force characteristics shown in Figure 1.12 and 1.13. The discrete solution points obtained by the numerical method are illustrated by the circles. It is clearly seen that without the event location it costs a lot of cpu–time to get past the nonsmooth corners. On the other hand, integrating with event location gets around the corners without any trouble.

1.4 Outline

The thesis is divided into 7 chapters, 5 appendices and the bibliography. The background and main motivation behind the project is given in chapter 1. The mathematical model of the European two–axle freight wagon is described in

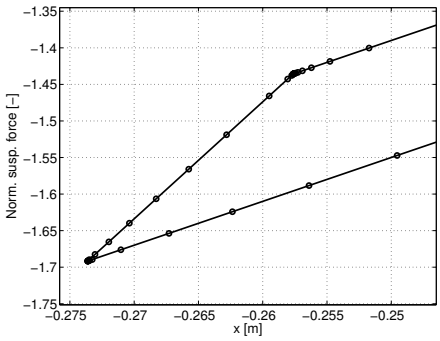

Figure 1.12: Without event location.

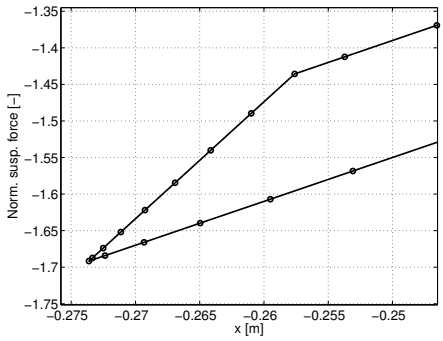

Figure 1.13: With event location.

chapter 2 together with a detailed analysis of the interacting forces. The model is essentially a system of nonsmooth ordinary differential equations. The numerical integration method used in order to extract the solution from this system is given in chapter 3. The design of the computer implementation of the model is sketched in chapter 4. The results obtained from the freight wagon model is presented and discussed in chapter 5. Future work in relation to this project is discussed in chapter 6. The conclusion is given in chapter 7.

Appendix A is devoted to give an overview of the notation and symbols used throughout the thesis. Appendix B includes four illustrative and small examples. Each of them emphasises some interesting and important aspects related to the modelling of two–axle freight wagons. The tedious derivation of the rotation matrices defining the relations between the different coordinate systems used is shown in Appendix C. Dantzig's algorithm for solving linear complementarity problems is given in Appendix D. An overview of the code developed in the project is given in Appendix E.

Chapter 2

Mathematical model

2.1 Curvilinear track

The equations of motion are of central importance in any multibody model. These equations are derived in this chapter and they are formulated on the general curvilinear track using the theory from [5]. This formulation is convenient because it allows one to analyse the vehicle on straight track, curved track and transition curves without complicating the governing equations of motion dramatically. For the analysis several coordinate systems are needed. These are presented along with the rotation matrices defining their mutual relations. A derivation of the relative kinematics is also given, resulting in the formulae needed in the analysis of the interacting forces.

2.1.1 Coordinate systems

	System	Base	Description
$R_O:$	$\{O; x, y, z\}$	$\mathbf{i}, \mathbf{j}, \mathbf{k}$	Inertial system
$R_T:$	$\{O_T; x_T, y_T, z_T\}$	$\mathbf{i}_T, \mathbf{j}_T, \mathbf{k}_T$	Track system
$R_b:$	$\{O_b; x_b, y_b, z_b\}$	$\mathbf{i}_b, \mathbf{j}_b, \mathbf{k}_b$	Body system
$R_c:$	$\{O_c; x_c, y_c, z_c\}$	$\mathbf{i}_c, \mathbf{j}_c, \mathbf{k}_c$	Wheel–rail contact system

Table 2.1: Coordinate systems.

The coordinate systems in Table 2.1 are found appropriate for the curvilinear track analysis. All coordinate systems are right hand systems.

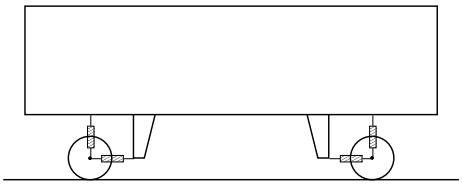

Figure 2.1: Side view of the freight wagon model.

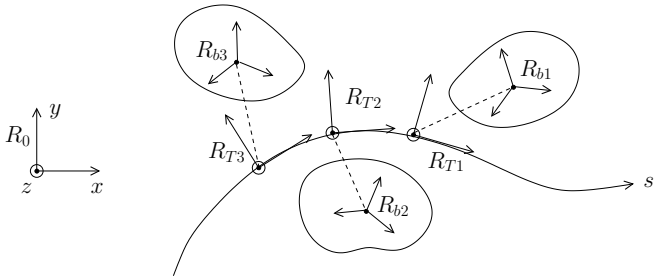

Figure 2.2: The coordinate systems for the curvilinear track analysis.

The inertial system is an absolute reference. The origin O is fixed to the beginning of the track and located in the track plane in the centre of the track. It is assumed that the track is initially straight and horizontal. x is tangent to the track centre line and points in the direction of travel. y is a horizontal axis pointing towards the left rail w.r.t. to the direction of travel. z is pointing upwards completing the right hand system.

The track system moves with the speed of the vehicle V along the track and it follows the curves and track gradients. The origin of the track systems, O_T, moves along the curvilinear abscissa s which is a coordinate axis along the track centre line. x_T (longitudinal direction) is tangent to the track centre line and points in the direction of travel. y_T (lateral direction) is a horizontal axis pointing towards the left rail w.r.t. to the direction of travel. z_T (vertical direction) is pointing upwards from the track. The body system is a local system belonging to a rigid body. The origin of the body system is located in the centre of mass, and the axes are aligned with the principal axes of the body. The wheel–rail contact system is an auxiliary coordinate system used in the formulation of the contact forces between the wheel and rail.

The freight wagon consists of two wheelsets and one carbody as illustrated in Figure 2.1. To model the freight wagon the coordinate systems shown in Figure 2.2 are used. Each body has its own body system and a corresponding track system.

2.1.2 Rotation matrices

The relation between the different coordinate systems is given by the Euler angles defined in this section. The rotation matrices are derived using successive (counter–clockwise) rotations, see Appendix C. A rotation of the angle α around the x, y, z coordinate axes, respectively, is given by the following matrices

$$\mathbf{A}_x^{(\alpha)} = \begin{bmatrix} 1 & 0 & 0 \\ 0 & \cos\alpha & -\sin\alpha \\ 0 & \sin\alpha & \cos\alpha \end{bmatrix} \quad \mathbf{A}_y^{(\alpha)} = \begin{bmatrix} \cos\alpha & 0 & \sin\alpha \\ 0 & 1 & 0 \\ -\sin\alpha & 0 & \cos\alpha \end{bmatrix} \quad \mathbf{A}_z^{(\alpha)} = \begin{bmatrix} \cos\alpha & -\sin\alpha & 0 \\ \sin\alpha & \cos\alpha & 0 \\ 0 & 0 & 1 \end{bmatrix}$$

The relation between the coordinate systems and the orientation of the axes are defined using these rotation matrices. An important property of the rotation matrices is that they are orthogonal. This means that the inverse matrix is equivalent to the transposed matrix, $\mathbf{A}^{-1} = \mathbf{A}^T$.

Inertial system to track system

1. Rotation around z by β_C (track yaw), $R_O \rightarrow R_{I1}$
2. Rotation around y_{I1} by θ_C (track gradient), $R_{I1} \rightarrow R_T$

$$\mathbf{A}_{OT} = \mathbf{A}_z^{(\beta_C)} \mathbf{A}_y^{(\theta_C)} \quad , \quad \mathbf{A}_{TO} = \mathbf{A}_{OT}^T$$

Track system to body system

1. Rotation around z_T by ψ (yaw), $R_T \rightarrow R_{I2}$
2. Rotation around y_{I2} by θ (pitch), $R_{I2} \rightarrow R_{I3}$
3. Rotation around x_{I3} by ϕ (roll), $R_{I3} \rightarrow R_b$

$$\mathbf{A}_{Tb} = \mathbf{A}_z^{(\psi)} \mathbf{A}_y^{(\theta)} \mathbf{A}_x^{(\phi)} \quad , \quad \mathbf{A}_{bT} = \mathbf{A}_{Tb}^T$$

Body system to wheel–rail contact system

1. Rotation around x_b by δ (contact angle), $R_b \rightarrow R_c$

$$\mathbf{A}_{bc} = \mathbf{A}_x^{(\delta)} \quad , \quad \mathbf{A}_{cb} = \mathbf{A}_{bc}^T$$

For a spinning body, e.g. a wheelset, the body system does not follow the rotation around the spinning axis. This means that $\theta \equiv 0$ for all time. See Table C.2 in Appendix C for an entire list of approximate rotation matrices used in the project.

2.1.3 Angular velocity of coordinate axes

The angular velocity of the track system, in reference to its own base, is

$$\boldsymbol{\Omega}_T = \left(\mathbf{A}_y^{(\theta_C)}\right)^T \begin{bmatrix} 0 \\ 0 \\ \dot{\beta}_C \end{bmatrix} + \begin{bmatrix} 0 \\ \dot{\theta}_C \\ 0 \end{bmatrix} \approx \begin{bmatrix} 0 \\ \dot{\theta}_C \\ \dot{\beta}_C \end{bmatrix}$$

The angular velocity of the body system, in reference to its own base, is

$$\boldsymbol{\Omega}_b = \mathbf{A}_{bT}\boldsymbol{\Omega}_T + \begin{bmatrix}\dot{\phi}\\0\\0\end{bmatrix} + \left(\mathbf{A}_x^{(\phi)}\right)^T \begin{bmatrix}0\\\dot{\theta}\\0\end{bmatrix} + \left(\mathbf{A}_x^{(\phi)}\right)^T \left(\mathbf{A}_y^{(\theta)}\right)^T \begin{bmatrix}0\\0\\\dot{\psi}\end{bmatrix} \approx \begin{bmatrix}\dot{\phi}\\\dot{\theta}_C + \dot{\theta}\\\dot{\beta}_C + \dot{\psi}\end{bmatrix}$$

2.1.4 Auxiliary functions

Two auxiliary functions $T_h(s)$ and $T_v(s)$ are defined as follows

$$\frac{\mathrm{d}^2 T_h(s)}{\mathrm{d}s^2} = \frac{1}{\rho_h(s)} \qquad \frac{\mathrm{d}^2 T_v(s)}{\mathrm{d}s^2} = -\frac{1}{\rho_v(s)} \tag{2.1}$$

where $1/\rho_h$ and $1/\rho_v$ are the curvatures of the track in the horizontal and vertical plane, respectively. From this definition, it is found by integration that

$$\frac{\mathrm{d}T_h(s)}{\mathrm{d}s} = \beta_C(s) \qquad \frac{\mathrm{d}T_v(s)}{\mathrm{d}s} = -\theta_C(s) \tag{2.2}$$

Furthermore, the following expressions can be derived

$$\frac{\mathrm{d}T_h(s(t))}{\mathrm{d}t} = \frac{\mathrm{d}T_h}{\mathrm{d}s}\frac{\mathrm{d}s}{\mathrm{d}t} = \beta_C V \tag{2.3}$$

$$\frac{\mathrm{d}T_v(s(t))}{\mathrm{d}t} = \frac{\mathrm{d}T_v}{\mathrm{d}s}\frac{\mathrm{d}s}{\mathrm{d}t} = -\theta_C V \tag{2.4}$$

and

$$\frac{\mathrm{d}^2 T_h(s(t))}{\mathrm{d}t^2} = \frac{\mathrm{d}(\beta_C V)}{\mathrm{d}t} = \frac{\mathrm{d}\beta_C}{\mathrm{d}s}\frac{\mathrm{d}s}{\mathrm{d}t}V + \beta_C\frac{\mathrm{d}V}{\mathrm{d}t} = \frac{V^2}{\rho_h} + \Gamma\beta_C$$

$$\frac{\mathrm{d}^2 T_v(s(t))}{\mathrm{d}t^2} = \frac{\mathrm{d}(-\theta_C V)}{\mathrm{d}t} = -\left(\frac{\mathrm{d}\theta_C}{\mathrm{d}s}\frac{\mathrm{d}s}{\mathrm{d}t}V + \theta_C\frac{\mathrm{d}V}{\mathrm{d}t}\right) = -\left(\frac{V^2}{\rho_v} + \Gamma\theta_C\right)$$

Here, V and Γ denote the speed and acceleration of the track system, respectively.

2.1.5 Relative kinematics

The position of the centre of mass of the i'th body, in reference to the track base, is

$$\mathbf{r} = \begin{bmatrix}x_i\\\bar{y}_i + y_i\\\bar{z}_i + z_i\end{bmatrix}$$

where the vector $[0, \bar{y}_i, \bar{z}_i]^T$ defines the equilibrium position. Consider the situation in Figure 2.3. P_i is a fixed point on the i'th body, and P_j is a fixed point on the j'th body. The relative displacement between P_i and P_j, in reference to the track base of the i'th body, is

$$\mathbf{r}_{ij} = \mathbf{r}_{Pj} - \mathbf{r}_{Pi} \tag{2.5}$$

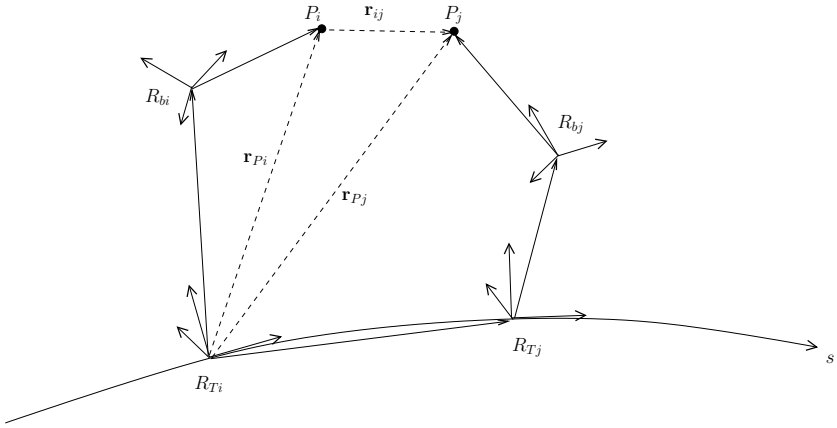

Figure 2.3: Relative displacement between P_i and P_j.

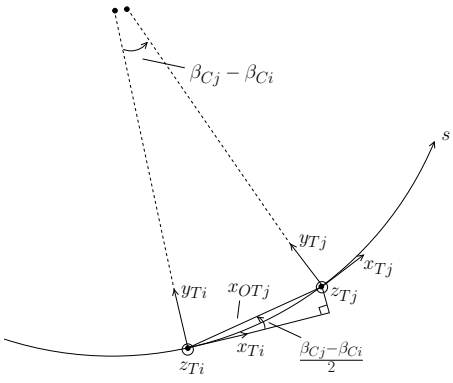

Figure 2.4: Horizontal plane.

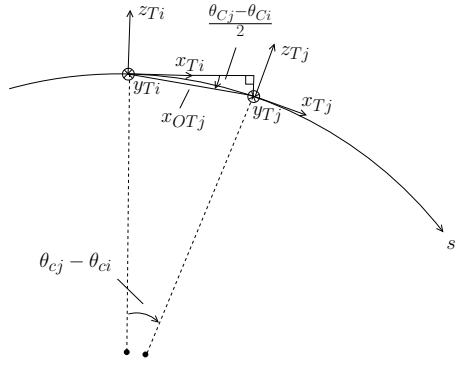

Figure 2.5: Vertical plane.

$$
\begin{aligned}
\mathbf{r}_{Pi} &= \begin{bmatrix} x_i \\ \bar{y}_i + y_i \\ \bar{z}_i + z_i \end{bmatrix} + \mathbf{A}_{Tibi} \begin{bmatrix} x_{Pi} \\ y_{Pi} \\ z_{Pi} \end{bmatrix} \\
\mathbf{r}_{Pj} &= \mathbf{A}_{TiTj} \left(\begin{bmatrix} x_j \\ \bar{y}_j + y_j \\ \bar{z}_j + z_j \end{bmatrix} + \mathbf{A}_{Tjbj} \begin{bmatrix} x_{Pj} \\ y_{Pj} \\ z_{Pj} \end{bmatrix} \right) + \begin{bmatrix} x_{OTj} \\ x_{OTj}(\beta_{Cj} - \beta_{Ci})/2 \\ -x_{OTj}(\theta_{Cj} - \theta_{Ci})/2 \end{bmatrix}
\end{aligned}
$$

where Figure 2.4 and 2.5 have been used in determining the position of O_{Tj} in reference to the track base of the i'th body. The nominal displacement between the P_i and P_j is

$$
\mathbf{r}_{ij0} = \begin{bmatrix} x_{Pj} + x_{OTj} - x_{Pi} \\ \bar{y}_j + y_{Pj} - \bar{y}_i - y_{Pi} \\ \bar{z}_j + z_{Pj} - \bar{z}_i - z_{Pi} \end{bmatrix}
$$

The *deformation* of an element between P_i and P_j is

$$
\begin{aligned}
\Delta\mathbf{r} &= \mathbf{r}_{Pj} - \mathbf{r}_{Pi} - \mathbf{r}_{ij0} \\
&= \mathbf{A}_{TiTj} \left(\begin{bmatrix} x_j \\ \bar{y}_j + y_j \\ \bar{z}_j + z_j \end{bmatrix} + \mathbf{A}_{Tjbj} \begin{bmatrix} x_{Pj} \\ y_{Pj} \\ z_{Pj} \end{bmatrix} \right) - \mathbf{A}_{Tibi} \begin{bmatrix} x_{Pi} \\ y_{Pi} \\ z_{Pi} \end{bmatrix} \\
&\quad + \begin{bmatrix} -x_i - x_{Pj} + x_{Pi} \\ x_{OTj}(\beta_{Cj} - \beta_{Ci})/2 - y_i - \bar{y}_j - y_{Pj} + y_{Pi} \\ -x_{OTj}(\theta_{Cj} - \theta_{Ci})/2 - z_i - \bar{z}_j - z_{Pj} + z_{Pi} \end{bmatrix} \\
&\approx \begin{bmatrix} [x_* - \psi_* y_{P*} + \theta_* z_{P*}]_i^j - (\beta_{Cj} - \beta_{Ci})(\bar{y}_j + y_{Pj}) + (\theta_{Cj} - \theta_{Ci})(\bar{z}_j + z_{Pj}) \\ [y_* + \psi_* x_{P*} - \phi_* z_{P*}]_i^j + (\beta_{Cj} - \beta_{Ci}) x_{Pj} + x_{OTj}(\beta_{Cj} - \beta_{Ci})/2 \\ [z_* - \theta_* x_{P*} + \phi_* y_{P*}]_i^j - (\theta_{Cj} - \theta_{Ci}) x_{Pj} - x_{OTj}(\theta_{Cj} - \theta_{Ci})/2 \end{bmatrix} \\
&= \begin{bmatrix} [x_* - \psi_* y_{P*} + \theta_* z_{P*} - \beta_{C*}(\bar{y}_* + y_{P*}) + \theta_{C*}(\bar{z}_* + z_{P*})]_i^j + A_1 \\ [y_* + \psi_* x_{P*} - \phi_* z_{P*} + \beta_{C*} x_{P*}]_i^j + x_{OTj}(\beta_{Cj} + \beta_{Ci})/2 + A_2 \\ [z_* - \theta_* x_{P*} + \phi_* y_{P*} - \theta_{C*} x_{P*}]_i^j - x_{OTj}(\theta_{Cj} + \theta_{Ci})/2 + A_3 \end{bmatrix}
\end{aligned}
$$

Here, products of small quantities have been neglected and

$$
\begin{aligned}
A_1 &= \beta_{Ci}(\bar{y}_j + y_{Pj} - \bar{y}_i - y_{Pi}) - \theta_{Ci}(\bar{z}_j + z_{Pj} - \bar{z}_i - z_{Pi}) \\
A_2 &= -\beta_{Ci}(x_{Pj} + x_{OTj} - x_{Pi}) \\
A_3 &= \theta_{Ci}(x_{Pj} + x_{OTj} - x_{Pi})
\end{aligned}
$$

Assuming a zero nominal displacement, i.e. $\mathbf{r}_{ij0} = \mathbf{0}$, makes

$$
A_1 = A_2 = A_3 = 0
$$

and thus

$$
\Delta\mathbf{r} \approx \begin{bmatrix} [x_* - \psi_* y_{P*} + \theta_* z_{P*} - \beta_{C*}(\bar{y}_* + y_{P*}) + \theta_{C*}(\bar{z}_* + z_{P*})]_i^j \\ [y_* + \psi_* x_{P*} - \phi_* z_{P*} + \beta_{C*} x_{P*}]_i^j + x_{OTj}(\beta_{Cj} + \beta_{Ci})/2 \\ [z_* - \theta_* x_{P*} + \phi_* y_{P*} - \theta_{C*} x_{P*}]_i^j - x_{OTj}(\theta_{Cj} + \theta_{Ci})/2 \end{bmatrix}
$$

A Taylor expansion of the auxiliary functions gives

$$T_h(s+a) = \sum_{n=0}^{\infty} \frac{a^n}{n!} \frac{\mathrm{d}^n T_h(s)}{\mathrm{d}s^n} \quad , \quad T_v(s+a) = \sum_{n=0}^{\infty} \frac{a^n}{n!} \frac{\mathrm{d}^n T_v(s)}{\mathrm{d}s^n}$$

The definition of the auxiliary functions says that

$$\frac{\mathrm{d}T_h(s)}{\mathrm{d}s} = \beta_C(s) \ , \ \frac{\mathrm{d}T_v(s)}{\mathrm{d}s} = -\theta_C(s) \ , \ \frac{\mathrm{d}^2 T_h(s)}{\mathrm{d}s^2} = \frac{1}{\rho_h(s)} \ , \ \frac{\mathrm{d}^2 T_v(s)}{\mathrm{d}s^2} = -\frac{1}{\rho_v(s)}$$

and by neglecting high order terms ($n \geq 3$) it is found that

$$\begin{aligned} T_h(s+a) - T_h(s) &\approx a\left[\beta_C(s) + \frac{a}{2\rho_h(s)}\right] \\ T_v(s+a) - T_v(s) &\approx -a\left[\theta_C(s) + \frac{a}{2\rho_v(s)}\right] \end{aligned}$$

Furthermore, it is valid that

$$\beta_C(s+a) - \beta_C(s) \approx \frac{a}{\rho_h} \qquad \theta_C(s+a) - \theta_C(s) \approx \frac{a}{\rho_v}$$

Using this information the following relations are found

$$\begin{aligned} T_h(s+a) - T_h(s) &\approx a\frac{\beta_C(s+a) + \beta_C(s)}{2} \\ T_v(s+a) - T_v(s) &\approx -a\frac{\theta_C(s+a) + \theta_C(s)}{2} \end{aligned}$$

and they are used to simplify the expression for the deformation, i.e.

$$\Delta\mathbf{r} \approx \begin{bmatrix} [x_* - \bar{y}_*\beta_{C*} + \bar{z}_*\theta_{C*} - y_{P*}(\psi_* + \beta_{C*}) + z_{P*}(\theta_* + \theta_{C*})]_i^j \\ [y_* + T_{h*} + x_{P*}(\psi_* + \beta_{C*}) - z_{P*}\phi_*]_i^j \\ [z_* + T_{v*} - x_{P*}(\theta_* + \theta_{C*}) + y_{P*}\phi_*]_i^j \end{bmatrix} \tag{2.6}$$

Since the components of $\Delta\mathbf{r}$ are small, it is approximately valid that the time derivative of the $\Delta\mathbf{r}$ is equal to the time derivative of its components, that is

$$\Delta\dot{\mathbf{r}} \approx \begin{bmatrix} \left[\dot{x}_* - \bar{y}_*\dot{\beta}_{C*} + \bar{z}_*\dot{\theta}_{C*} - y_{P*}(\dot{\psi}_* + \dot{\beta}_{C*}) + z_{P*}(\dot{\theta}_* + \dot{\theta}_{C*})\right]_i^j \\ \left[\dot{y}_* + \dot{T}_{h*} + x_{P*}(\dot{\psi}_* + \dot{\beta}_{C*}) - z_{P*}\dot{\phi}_*\right]_i^j \\ \left[\dot{z}_* + \dot{T}_{v*} - x_{P*}(\dot{\theta}_* + \dot{\theta}_{C*}) + y_{P*}\dot{\phi}_*\right]_i^j \end{bmatrix} \tag{2.7}$$

The expressions in equation (2.6) and (2.7) are first order approximations and it is assumed that the attachment points of the undeformed suspension element are identical in space. Note also that the vectors are expressed in reference to the track base of the i'th body.

2.1.6 Equations of motion

The equations of motion for the wheelsets and carbody are presented in this section. The derivation procedure presented is based on [5, 60]. The wheelset is treated first. For convenience, the crossproduct $\mathbf{x}\times$ is expressed by the linear operator $\tilde{\mathbf{x}}$ (see Appendix A for further details on notation). The velocity $\mathbf{v}$ and acceleration $\mathbf{a}$ of the centre of mass are expressed in reference to the track base.

$$\mathbf{v} = \begin{bmatrix} V \\ 0 \\ 0 \end{bmatrix} + \begin{bmatrix} \dot{x} \\ \dot{y} \\ \dot{z} \end{bmatrix} + \tilde{\boldsymbol{\Omega}}_T \begin{bmatrix} x \\ \bar{y}+y \\ \bar{z}+z \end{bmatrix} \approx \begin{bmatrix} V+\dot{x}+\dot{\theta}_C\bar{z}-\dot{\beta}_C\bar{y} \\ \dot{y} \\ \dot{z} \end{bmatrix} \tag{2.8}$$

$$\mathbf{a} = \begin{bmatrix} \Gamma \\ 0 \\ 0 \end{bmatrix} + \tilde{\boldsymbol{\Omega}}_T \begin{bmatrix} V \\ 0 \\ 0 \end{bmatrix} + \begin{bmatrix} \ddot{x} \\ \ddot{y} \\ \ddot{z} \end{bmatrix} + \left(\dot{\tilde{\boldsymbol{\Omega}}}_T + \tilde{\boldsymbol{\Omega}}_T^2\right) \begin{bmatrix} x \\ \bar{y}+y \\ \bar{z}+z \end{bmatrix} + 2\tilde{\boldsymbol{\Omega}}_T \begin{bmatrix} \dot{x} \\ \dot{y} \\ \dot{z} \end{bmatrix} \tag{2.9}$$

$$\approx \begin{bmatrix} \Gamma+\ddot{x}+\ddot{\theta}_C\bar{z}-\ddot{\beta}_C\bar{y} \\ \ddot{y}+V^2/\rho_h \\ \ddot{z}-V^2/\rho_v \end{bmatrix} = \begin{bmatrix} \Gamma+\ddot{x}+\ddot{\theta}_C\bar{z}-\ddot{\beta}_C\bar{y} \\ \ddot{y}+\dot{T}_h-\Gamma\beta_C \\ \ddot{z}+\dot{T}_v+\Gamma\theta_C \end{bmatrix} \tag{2.10}$$

The angular velocity of the wheelset $\boldsymbol{\Omega}$ is expressed in reference to the base of the body system. Note, that the wheelset has a spin around its lateral axis.

$$\boldsymbol{\Omega} = \begin{bmatrix} \Omega_{bx} \\ \Omega_{by}+V/r_0+\dot{\nu} \\ \Omega_{bz} \end{bmatrix} \approx \begin{bmatrix} \dot{\phi} \\ \dot{\theta}_C+\dot{\nu}+V/r_0 \\ \dot{\beta}_C+\dot{\psi} \end{bmatrix} \tag{2.11}$$

Here, $\dot{\nu}$ is a *spin perturbation* that measures the difference between the nominal and actual spin of the wheelset around its axis of revolution. The nominal spin is V/r_0, where r_0 is the nominal rolling radius.

The change in linear and angular momentum are fundamental quantities regarding the motion of a rigid body.

$$\begin{cases} \dot{\mathbf{p}} = m\mathbf{a} \\ \dot{\mathbf{L}} = \mathbf{I}_s\boldsymbol{\alpha} + \tilde{\boldsymbol{\Omega}}_b\mathbf{I}_s\boldsymbol{\Omega} \end{cases} \tag{2.12}$$

$\boldsymbol{\alpha}$ is the angular acceleration and $\mathbf{I}_s$ is the inertia tensor. The equation with the linear momentum is expressed in reference to the track base, and the equation with the angular momentum is expressed in reference to the base of the body system. Equation (2.12) is rewritten into

$$\begin{bmatrix} \dot{\mathbf{p}} \\ \dot{\mathbf{L}} \end{bmatrix} = \bar{\mathbf{M}} \begin{bmatrix} \mathbf{a} \\ \boldsymbol{\alpha} \end{bmatrix} + \begin{bmatrix} \mathbf{0} \\ \tilde{\boldsymbol{\Omega}}_b\mathbf{I}_s\boldsymbol{\Omega} \end{bmatrix} \tag{2.13}$$

where

$$\bar{\mathbf{M}} = \mathrm{diag}([m, m, m, I_{xx}, I_{yy}, I_{zz}]) \quad , \quad \mathbf{I}_s = \mathrm{diag}([I_{xx}, I_{yy}, I_{zz}])$$

The system is in dynamical equilibrium when the virtual power vanishes

$$\delta W = \begin{bmatrix} \delta\mathbf{v} \\ \delta\boldsymbol{\Omega} \end{bmatrix}^T \left(\begin{bmatrix} \dot{\mathbf{p}} \\ \dot{\mathbf{L}} \end{bmatrix} - \begin{bmatrix} \mathbf{F}_{\mathrm{ext}} \\ \mathbf{M}_{\mathrm{ext}} \end{bmatrix} \right) = 0 \tag{2.14}$$

Here, $\mathbf{F}_{\text{ext}} = [F_x, F_y, F_z]^T$ are the external forces in reference to the track base, and $\mathbf{M}_{\text{ext}} = [M_x, M_y, M_z]^T$ are the external torques in reference to the base of the body system. Combining equation (2.13) and (2.14) it is found that

$$\delta W = \begin{bmatrix} \delta\mathbf{v} \\ \delta\boldsymbol{\Omega} \end{bmatrix}^T \left(\bar{\mathbf{M}} \begin{bmatrix} \mathbf{a} \\ \boldsymbol{\alpha} \end{bmatrix} + \begin{bmatrix} \mathbf{0} \\ \tilde{\boldsymbol{\Omega}}_b \mathbf{I}_s \boldsymbol{\Omega} \end{bmatrix} - \begin{bmatrix} \mathbf{F}_{\text{ext}} \\ \mathbf{M}_{\text{ext}} \end{bmatrix} \right) = 0 \tag{2.15}$$

Introducing the generalised coordinates one can write

$$\begin{aligned} D_x &= x + \bar{z}\theta_C - \bar{y}\beta_C \\ D_y &= y + T_h \\ D_z &= z + T_v \\ D_\phi &= \phi \\ D_\theta &= \theta_C + \nu \\ D_\psi &= \beta_C + \psi \end{aligned} \qquad \mathbf{q} = \begin{bmatrix} D_x \\ D_y \\ D_z \\ D_\phi \\ D_\theta \\ D_\psi \end{bmatrix} \qquad \dot{\mathbf{q}} = \begin{bmatrix} \dot{D}_x \\ \dot{D}_y \\ \dot{D}_z \\ \dot{D}_\phi \\ \dot{D}_\theta \\ \dot{D}_\psi \end{bmatrix}$$

The linear and angular acceleration can be expressed using the generalised coordinates by

$$\begin{bmatrix} \mathbf{v} \\ \boldsymbol{\Omega} \end{bmatrix} = \mathbf{J}\dot{\mathbf{q}} + \tilde{\mathbf{j}} \quad , \quad \begin{bmatrix} \mathbf{a} \\ \boldsymbol{\alpha} \end{bmatrix} \approx \mathbf{J}\ddot{\mathbf{q}} + \bar{\mathbf{j}} \quad , \quad \begin{bmatrix} \delta\mathbf{v} \\ \delta\boldsymbol{\Omega} \end{bmatrix} = \mathbf{J}\delta\dot{\mathbf{q}}$$

where $\mathbf{J}$ is equal to the identity matrix and

$$\tilde{\mathbf{j}} = [V, -V\beta_C, V\theta_C, 0, V/r_0, 0]^T \quad , \quad \bar{\mathbf{j}} = [\Gamma, -\Gamma\beta_C, \Gamma\theta_C, 0, \Gamma/r_0, 0]^T$$

Equation (2.15) is now rewritten into

$$\delta\dot{\mathbf{q}}^T \left(\mathbf{J}^T \bar{\mathbf{M}} \mathbf{J}\ddot{\mathbf{q}} + \mathbf{J}^T \bar{\mathbf{M}} \bar{\mathbf{j}} + \mathbf{J}^T \begin{bmatrix} \mathbf{0} \\ \tilde{\boldsymbol{\Omega}}_b \mathbf{I}_s \boldsymbol{\Omega} \end{bmatrix} - \mathbf{J}^T \begin{bmatrix} \mathbf{F}_{\text{ext}} \\ \mathbf{M}_{\text{ext}} \end{bmatrix} \right) = 0$$

The linear independency in the generalised coordinates gives the following condensed formulation of the equations of motion, also known as the projected Newton-Euler equations

$$\mathbf{M}\ddot{\mathbf{q}} - \mathbf{h}(\mathbf{q}, \dot{\mathbf{q}}) = \mathbf{0} \tag{2.16}$$

where

$$\begin{aligned} \mathbf{M} &= \mathbf{J}^T \bar{\mathbf{M}} \mathbf{J} \\ \mathbf{h}(\mathbf{q}, \dot{\mathbf{q}}) &= -\mathbf{J}^T \bar{\mathbf{M}} \bar{\mathbf{j}} - \mathbf{J}^T \begin{bmatrix} \mathbf{0} \\ \tilde{\boldsymbol{\Omega}}_b \mathbf{I}_s \boldsymbol{\Omega} \end{bmatrix} + \mathbf{J}^T \begin{bmatrix} \mathbf{F}_{\text{ext}} \\ \mathbf{M}_{\text{ext}} \end{bmatrix} \end{aligned}$$

Hence, the motion of the wheelset is determined from

$$\ddot{\mathbf{q}} \approx \begin{bmatrix} -\Gamma + F_x/m \\ \Gamma\beta_C + F_y/m \\ -\Gamma\theta_C + F_z/m \\ (\dot{D}_\psi I_{yy} V/r_0 + M_x)/I_{xx} \\ M_y/I_{yy} \\ (-\dot{D}_\phi I_{yy} V/r_0 + M_z)/I_{zz} \end{bmatrix} \quad , \quad \begin{bmatrix} \ddot{D}_x \\ \ddot{D}_y \\ \ddot{D}_z \\ \ddot{D}_\phi \\ \ddot{D}_\psi \\ \dot{D}_\beta \end{bmatrix} \approx \begin{bmatrix} -\Gamma + F_x/m \\ \Gamma\beta_C + F_y/m \\ -\Gamma\theta_C + F_z/m \\ (\dot{D}_\psi I_{yy} V/r_0 + M_x)/I_{xx} \\ (-\dot{D}_\phi I_{yy} V/r_0 + M_z)/I_{zz} \\ M_y/I_{yy} \end{bmatrix}$$

where $D_\beta = \dot{D}_\theta$.

The same approach is used for the carbody. The only difference is that the carbody is a non–spinning body meaning that $\mathbf{\Omega}_b \equiv \mathbf{\Omega}$. The resulting coordinates and equations are given below.

$$\begin{array}{l} D_x = x + \bar{z}\theta_C - \bar{y}\beta_C \\ D_y = y + T_h \\ D_z = z + T_v \\ D_\phi = \phi \\ D_\theta = \theta_C + \theta \\ D_\psi = \beta_C + \psi \end{array} \qquad \mathbf{q} = \begin{bmatrix} D_x \\ D_y \\ D_z \\ D_\phi \\ D_\theta \\ D_\psi \end{bmatrix} \qquad \dot{\mathbf{q}} = \begin{bmatrix} \dot{D}_x \\ \dot{D}_y \\ \dot{D}_z \\ \dot{D}_\phi \\ \dot{D}_\theta \\ \dot{D}_\psi \end{bmatrix}$$

$$\mathbf{M}\ddot{\mathbf{q}} = -\mathbf{J}^T\bar{\mathbf{M}}\bar{\mathbf{j}} - \mathbf{J}^T \begin{bmatrix} \mathbf{0} \\ \tilde{\mathbf{\Omega}}_b \mathbf{I}_s \mathbf{\Omega} \end{bmatrix} + \mathbf{J}^T \begin{bmatrix} \mathbf{F}_{\text{ext}} \\ \mathbf{M}_{\text{ext}} \end{bmatrix} \quad , \quad \mathbf{\Omega} = \mathbf{\Omega}_b \approx \begin{bmatrix} \dot{\phi} \\ \dot{\theta}_C + \dot{\theta} \\ \dot{\beta}_C + \dot{\psi} \end{bmatrix}$$

$$\ddot{\mathbf{q}} \approx \begin{bmatrix} -\Gamma + F_x/m \\ \Gamma\beta_C + F_y/m \\ -\Gamma\theta_C + F_z/m \\ M_x/I_{xx} \\ M_y/I_{yy} \\ M_z/I_{zz} \end{bmatrix} \quad , \quad \begin{bmatrix} \ddot{D}_x \\ \ddot{D}_y \\ \ddot{D}_z \\ \ddot{D}_\phi \\ \ddot{D}_\theta \\ \ddot{D}_\psi \end{bmatrix} \approx \begin{bmatrix} -\Gamma + F_x/m \\ \Gamma\beta_C + F_y/m \\ -\Gamma\theta_C + F_z/m \\ M_x/I_{xx} \\ M_y/I_{yy} \\ M_z/I_{zz} \end{bmatrix}$$

To have a steady motion of the freight wagon the carbody is restricted to move with the motion of the track system, R_T, along the track. Hence, $x = 0$ and the carbody has no longitudinal degree of freedom. This constraint will put energy into the system. Introducing this constraint we have

$$\begin{aligned} D_x &= \bar{z}\theta_C - \bar{y}\beta_C \\ \dot{D}_x &= \bar{z}V/\rho_v - \bar{y}V/\rho_h \end{aligned}$$

and the equations are reduced to

$$\begin{bmatrix} \ddot{D}_y \\ \ddot{D}_z \\ \ddot{D}_\phi \\ \ddot{D}_\theta \\ \ddot{D}_\psi \end{bmatrix} \approx \begin{bmatrix} \Gamma\beta_C + F_y/m \\ -\Gamma\theta_C + F_z/m \\ M_x/I_{xx} \\ M_y/I_{yy} \\ M_z/I_{zz} \end{bmatrix}$$

2.1.7 Defining the track

The theoretical track is defined through its horizontal curvature $1/\rho_h(s)$ and vertical curvature $1/\rho_v(s)$. Only piecewise linear curvature functions are considered. An example of a horizontal curvature function for a left hand curve is shown in Figure 2.6. The track is divided into stages according to the linear sections of the curvatures. For the i'th stage the curvature can be represented as shown in equation (2.17), see also Figure 2.7.

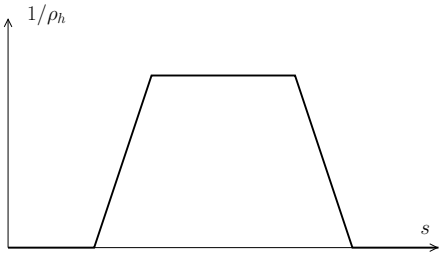

Figure 2.6: Horizontal curvature for a left hand curve.

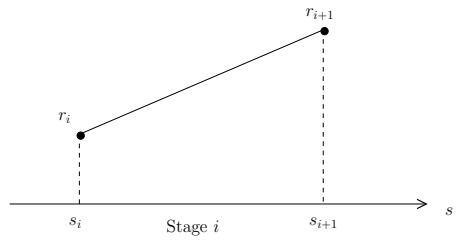

Figure 2.7: The curvature is linear.

$$\frac{1}{\rho(s)} = r_i + \frac{r_{i+1} - r_i}{s_{i+1} - s_i}(s - s_i) \qquad s_i \le s \le s_{i+1} \tag{2.17}$$

The curve parameters (β_C, θ_C, T_h and T_v) are found by integration and utilising the definition of the auxiliary functions given in equation (2.1) and (2.2). For the i'th stage ($s_i \le s \le s_{i+1}$) the theoretical curvilinear track is represented by

$$\begin{aligned}
\frac{1}{\rho_h(s)} &= P^h_{i1}(s) \\
\frac{1}{\rho_v(s)} &= P^v_{i1}(s) \\
\beta_C(s) &= \beta_C(s_i) + \int_{s_i}^{s} P^h_{i1}(s')\,\mathrm{d}s' \\
&= \beta_C(s_i) + P^h_{i2}(s) \\
\theta_C(s) &= \theta_C(s_i) + \int_{s_i}^{s} P^v_{i1}(s')\,\mathrm{d}s' \\
&= \theta_C(s_i) + P^v_{i2}(s) \\
T_h(s) &= T_h(s_i) + \beta_C(s_i)(s - s_i) + \int_{s_i}^{s} P^h_{i2}(s')\,\mathrm{d}s' \\
&= T_h(s_i) + \beta_C(s_i)(s - s_i) + P^h_{i3}(s) \\
T_v(s) &= T_v(s_i) - \left(\theta_C(s_i)(s - s_i) + \int_{s_i}^{s} P^v_{i2}(s')\,\mathrm{d}s'\right) \\
&= T_v(s_i) - (\theta_C(s_i)(s - s_i) + P^v_{i3}(s))
\end{aligned}$$

where the polynomials $P^k_{ij}(s)$ are

$$\begin{aligned}
P^k_{i1}(s) &= r^k_i + \frac{r^k_{i+1} - r^k_i}{s_{i+1} - s_i}(s - s_i) \\
P^k_{i2}(s) &= \frac{(s - s_i)(r^k_{i+1}(s - s_i) - r^k_i(s_i + s - 2s_{i+1}))}{2(s_{i+1} - s_i)} \\
P^k_{i3}(s) &= \frac{(s - s_i)^2(r^k_{i+1}(s - s_i) - r^k_i(2s_i + s - 3s_{i+1}))}{6(s_{i+1} - s_i)}
\end{aligned}$$

The track coordinates in the inertial system, R_0, are obtained from the curve parameters by integrating the following relation

$$\begin{bmatrix} \mathrm{d}x \\ \mathrm{d}y \\ \mathrm{d}z \end{bmatrix} = \mathbf{A}_z^{(\beta_C)} \mathbf{A}_y^{(\theta_C)} \begin{bmatrix} \mathrm{d}s \\ 0 \\ 0 \end{bmatrix} = \begin{bmatrix} \cos\beta_C \cos\theta_C \, \mathrm{d}s \\ \sin\beta_C \cos\theta_C \, \mathrm{d}s \\ -\sin\theta_C \, \mathrm{d}s \end{bmatrix}$$

In Figure 2.8 to 2.11 and example is shown illustrating the curve parameters for a left hand curve.

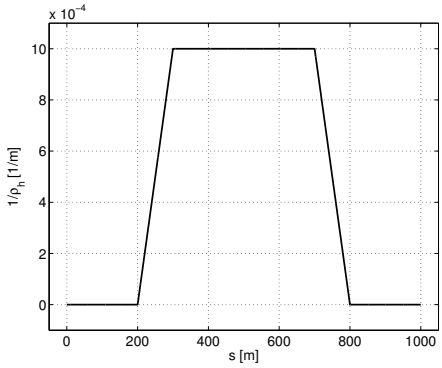

Figure 2.8: Horizontal curvature, $1/\rho_h(s)$.

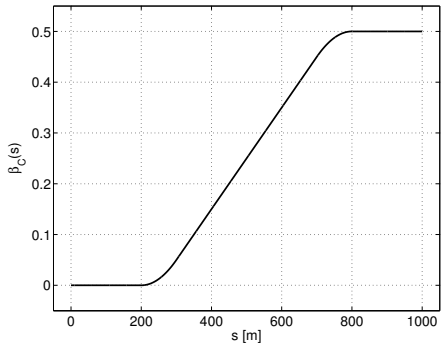

Figure 2.9: Track yaw, $\beta_C(s)$.

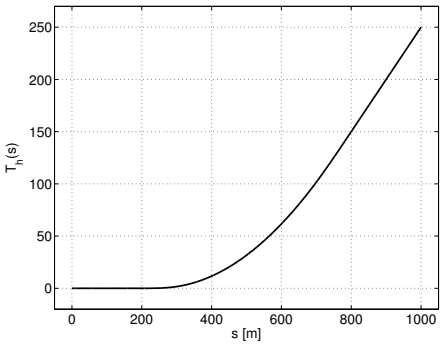

Figure 2.10: Auxiliary function, $T_h(s)$.

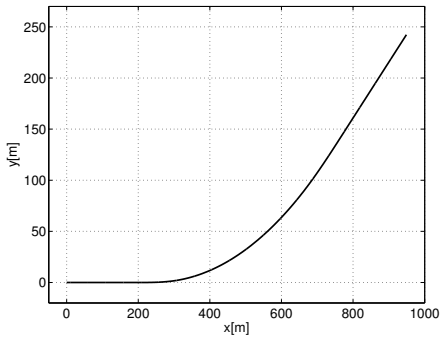

Figure 2.11: Track seen from above.

To reduce the effect of the centrifugal acceleration in curves the outer rail is often superelevated. The inner rail keeps the same level as on straight track. This track cant is modelled by adjusting the auxiliary function $T_v(s)$ [5]. The contact forces are computed using the adjusted values:

$$\begin{aligned} \Delta T_v &= |\phi_{\mathrm{SE}}(s)| b_0 \\ T_v\big|_{\mathrm{left}} &\leftarrow T_v + \Delta T_v + \phi_{\mathrm{SE}}(s) b_0 \\ T_v\big|_{\mathrm{right}} &\leftarrow T_v + \Delta T_v - \phi_{\mathrm{SE}}(s) b_0 \end{aligned}$$

where $\phi_{\mathrm{SE}}(s)$ is the superelevation and $2b_0 = 1.5$ m is the distance between the nominal rolling circles of the wheels. Linear superelevation ramps are used in this project making the shape of the superelevation function $\phi_{\mathrm{SE}}(s)$ similar to the curvature in Figure 2.6.

2.2 Wheel–rail contact

The wheel–rail contact forces have the fundamental task of guiding the rail vehicle along the track. The modelling of the wheel–rail contact forces become naturally an important aspect of any rail vehicle model. The geometry of the contacting surfaces and the elastic interaction between the bodies makes it difficult to formulate simple and accurate routines for computing the contact forces. Both wheels and rails are made of steel with the material properties: Poisson's ratio $\nu = 0.27$, Young's modulus $E = 2.1 \cdot 10^{11}$ N/m^2, and shear modulus $G = E/(2(1+\nu)) = 8.27 \cdot 10^{10}$ N/m^2. The friction coefficient between the wheel and rail is set to $\mu = 0.30$.

A conventional wheelset consists of two rigidly connected wheels. The wheel profiles can be divided into three parts: tread, root and flange. In Figure 2.12 the European standard wheel profile S1002 is shown. The wheel is usually in contact with the rail through a contact region located on the tread. The lateral distance from the centre of mass of the wheelset to the nominal rolling circle is 0.75 m. The conical shape of the tread gives the wheelset a self steering capability due to the difference in rolling radii, caused by a wheelset in any off–centred position. The flange is located on the inside of the wheel tread and improves the lateral guiding whenever necessary, e.g. in curves or during hunting. The European standard rail profile UIC60 is shown in Figure 2.13. The rails usually have an inclination inwards, see Figure 2.14, in order to match the conical wheel profile. This rail inclination is not the same throughout Europe. For instance, it is 1/40 in Germany, 1/30 in Sweden and 1/20 in France. The rail separation is defined by the track gauge which is measured 14 mm below the top of the rails. The standard track gauge of 1435 mm is used in all simulations. It is assumed that the rails are fixed to the ground without any flexibility. This flexibility has previously been investigated by Slivsgaard [79] and the effect was observed to be of minor importance regarding the dynamic behaviour of the vehicle.

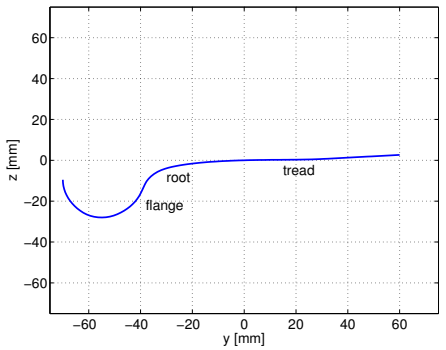

Figure 2.12: S1002 standard wheel profile.

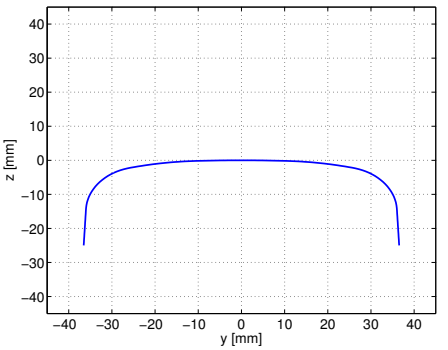

Figure 2.13: UIC60 standard rail profile.

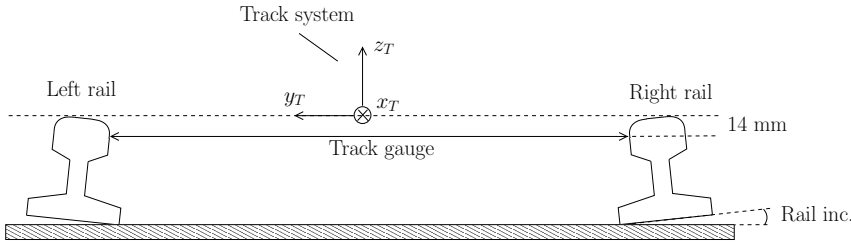

Figure 2.14: Track gauge and rail inclination.

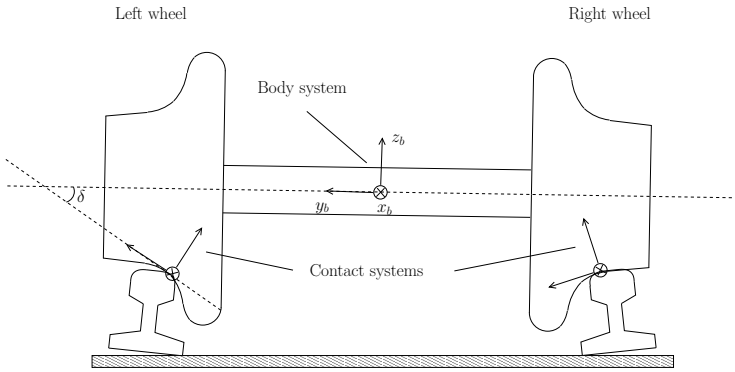

Figure 2.15: Contact systems.

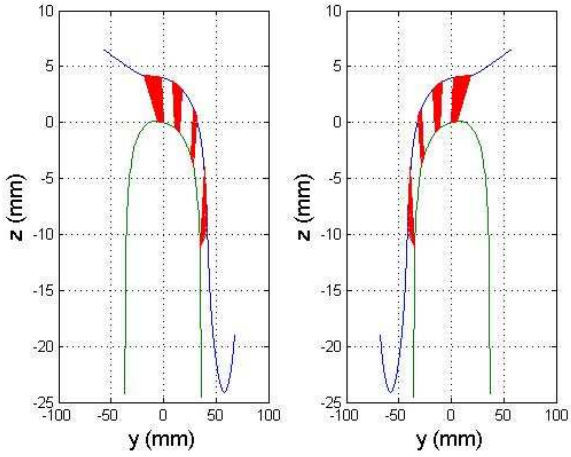

Figure 2.16: Possible contact points.

As a consequence of the shape of the wheel and rail profiles they only touch each other in certain regions of the profiles, see Figure 2.16. This makes the contact parameters, e.g. position of contact point and contact angle, discontinuous functions of the lateral position of the wheelset.

A thorough treatment of contact mechanics can be found in the work by Johnson [35], and the state–of–the–art article in [63] gives an overview of important issues and existing models regarding the wheel–rail contact.

When the wheel and rail are pressed together by a certain load, a contact region is generated as a consequence of the elasticity of the bodies. The contact region typically has the size of a finger nail. In the contact region both normal and shear stresses exist. In fact, we are dealing with a three dimensional rolling contact problem with a coupled normal and tangential problem being very difficult to solve. Through a finite element approach an accurate computation of the contact forces can be found (see e.g. [88]), however, incorporating this into the multibody model here is not really appropriate because the contact computations would be very time demanding and thereby making the wanted dynamic analysis unfeasible.

The half–space assumption is often used in the analysis of the wheel–rail contact. It says that, since the contact region is small compared to the dimensions of the wheel and rail, it is reasonable to assume that the contact stresses are not influenced by the shape of the bodies. The stresses are calculated by assuming that the contacting bodies are semi–infinite bodies limited by a straight plane. Furthermore, the contacting bodies are made of the same material and thus they are said to be quasi–identical. This leads to the convenient result that the normal– and tangential contact problem can be treated independently. Furthermore, the contact problem is considered to be quasi–static. Kalker [39] has developed the program CONTACT being able to solve contact problems with bodies described by elastic half–spaces. The program is very general and accurate, and often considered as an exact reference in comparing wheel–rail rolling contact routines. On the other hand, it is computationally very demanding and not well suited for multibody models.

To simplify the contact problem further, the contact region is approximated by an ellipse according to Hertz' theory [25]. With the Hertzian contact assumption, it is possible to formulate simplified models that are fast and still retain an adequate accuracy. Moreover, it is assumed that the contact problem is two–dimensional, i.e. neglecting the yaw of the wheelset, and that there is no longitudinal shift of the contact point on the wheel. This assumption is reasonable on straight track and curves with large radii (> 500 m), which also is the scenario of the simulations presented later on. It is also assumed that the torsional modes of the wheelset (having a frequency range of $50 - 80$ Hz) do not interfere with the low frequent modes of interest here (< 10 Hz). Due to the small contact region the wheel–rail interaction is represented as point forces in the complete vehicle model. These point forces are computed as integrals of the surface stresses over the contact region. The contact forces are formulated in a

contact system located at the corresponding contact point, see Figure 2.15.

2.2.1 Normal contact

Two methods are common when solving the normal contact problem: an elastic model or a constraint model. In the elastic model, the wheelset and rails are rigid and the normal force is computed by modelling the contact stiffness as a stiff spring using Hertz' theory [25]. The spring deformation is determined from a fictitious penetration of the wheel into the rail. In the constraint model, the wheelset and rails are also rigid, however, the contact stiffness is assumed to be infinite. The influence of the normal force is incorporated into the model through contact constraints that, typically, makes the vertical and roll motion of the wheelset to be dependent coordinates and thereby reducing the wheelsets degrees of freedom (DOF). The constraint model has been analysed and the general procedure is exemplified in Appendix B.4. The model assumes that the wheelset is supported through a unique contact point on each wheel. Having several contact points on a wheel leads to a situation were the support of the wheelset no longer has a unique solution. The elastic model does not have this restriction and it will be used for the freight wagon model.

Penetration In the elastic model, the normal force is a function of the penetration of the wheel into the rail. The vector from the contact point on the wheel to the contact point on the rail, in reference to the base of the contact system, is

$$\mathbf{R}_{\text{pen}} = \mathbf{A}_{cb} \left(\mathbf{A}_{bT} \left(\mathbf{R}_R - \mathbf{R}_C \right) - \mathbf{R}_w \right)$$

where

$$\begin{aligned} \mathbf{R}_C &= (\bar{y} + y)\, \mathbf{j}_T + (\bar{z} + z)\, \mathbf{k}_T \\ \mathbf{R}_R &= R_{Ry}\, \mathbf{j}_T + R_{Rz}\, \mathbf{k}_T \\ \mathbf{R}_w &= R_{wy}\, \mathbf{j}_b + R_{wz}\, \mathbf{k}_b \end{aligned}$$

$\mathbf{R}_C$ and $\mathbf{R}_R$ defines the position of the centre of mass of the wheelset and the position of the contact point on the rail, respectively, in reference to the base of the track system. $\mathbf{R}_w$ is the position of the contact point on the wheel in reference to the base of the body system. $\mathbf{R}_w$ and $\mathbf{R}_R$ are tabulated for different lateral displacements of the wheelset before simulation. The penetration depth, q_{pen}, is the z–component of $\mathbf{R}_{\text{pen}}$

$$\begin{aligned} q_{\text{pen}} \approx\ & -(R_{Ry} - \bar{y} - y + \phi(R_{Rz} - \bar{z}) - R_{wy}) \sin\delta \\ & +(R_{Rz} - \bar{z} - z - \phi(R_{Ry} - \bar{y}) - R_{wz}) \cos\delta \end{aligned}$$

Normal force The normal force, N, is calculated using Hertz' theory [25]. The contact region is approximated by an ellipse leading to a semi–ellipsoidal normal stress distribution. The semi–axes of the contact ellipse are denoted by a (longitudinal) and b (lateral). From the theory the following useful relations follow

$$N \propto (q_{\text{pen}})^{\frac{3}{2}} \quad , \quad a \propto N^{\frac{1}{3}} \quad , \quad b \propto N^{\frac{1}{3}} \tag{2.18}$$

By pre–calculating the reference values N_0 and $q_{\text{pen},0}$ from a static consideration of the wheelset on the rail, it is possible to compute the dynamic normal force during simulation by

$$N = N_0 \left(\frac{q_{\text{pen}}}{q_{\text{pen},0}} \right)^{\frac{3}{2}} \tag{2.19}$$

Likewise, the contact ellipse is dynamically adjusted through the use of the pre–calculated reference values a_0 and b_0.

$$\frac{a}{b} = \frac{a_0}{b_0} \quad , \quad ab = a_0 b_0 \left(\frac{N}{N_0} \right)^{\frac{2}{3}} = a_0 b_0 \frac{q_{\text{pen}}}{q_{\text{pen},0}} \tag{2.20}$$

It is worth mentioning that the Hertzian spring stiffness is very high (about 10^9 N/m) due to the hard steel to steel contact. For numerical reasons, and to some degree represent the material damping, a linear damping term is added to equation (2.19). The damping coefficient is set to $1.5 \cdot 10^5$ N s/m based on the work [54].

2.2.2 Tangential contact

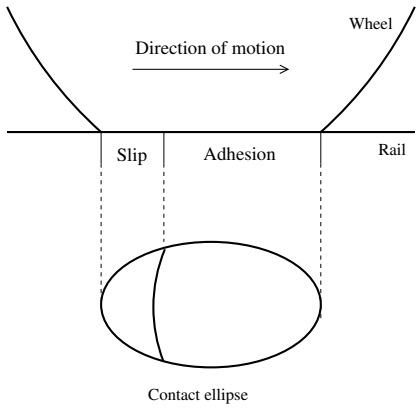

Figure 2.17: The adhesion and slip partition of the contact ellipse.

Creep The tangential contact forces (creep forces) arise because of a micro–slip between the wheel and rail. Figure 2.17 illustrates how the contact region (approximated by an ellipse) is partitioned into an adhesion part and a slip part in the simple case of purely longitudinal creepage.

The normalised rigid slip between the wheel and rail (creep) plays an important role in computing the tangential forces. The expressions used for computing the creep are derived next. From equation (2.8) and (2.11) it is seen that the linear and angular velocity of the wheelset can be formulated as

$$\mathbf{v} = \begin{bmatrix} V + \dot{D}_x \\ \dot{y} \\ \dot{z} \end{bmatrix} \quad , \quad \boldsymbol{\Omega} = \begin{bmatrix} \dot{D}_\phi \\ D_\beta + V/r_0 \\ \dot{D}_\psi \end{bmatrix}$$

The relative velocity between the wheel and rail, in reference to the base of the contact system, is

$$\begin{aligned}
\mathbf{v}_{\text{con}} &= \mathbf{A}_{cb}\left(\mathbf{A}_{bT}\,\mathbf{v} + \boldsymbol{\Omega} \times \mathbf{R}_w\right) \\
&\approx \mathbf{A}_{cb}\left(\begin{bmatrix} 1 & \psi & 0 \\ -\psi & 1 & \phi \\ 0 & -\phi & 1 \end{bmatrix}\begin{bmatrix} V + \dot{D}_x \\ \dot{y} \\ \dot{z} \end{bmatrix} + \begin{bmatrix} (D_\beta + V/r_0)R_{wz} - \dot{D}_\psi R_{wy} \\ -\dot{D}_\phi R_{wz} \\ \dot{D}_\phi R_{wy} \end{bmatrix}\right) \\
&= \mathbf{A}_{cb}\begin{bmatrix} V + \dot{D}_x + \psi\dot{y} + (D_\beta + V/r_0)R_{wz} - \dot{D}_\psi R_{wy} \\ -\psi(V + \dot{D}_x) + \dot{y} + \phi\dot{z} - \dot{D}_\phi R_{wz} \\ -\phi\dot{y} + \dot{z} + \dot{D}_\phi R_{wy} \end{bmatrix} \\
&= \begin{bmatrix} V + \dot{D}_x + \psi\dot{y} + (D_\beta + V/r_0)R_{wz} - \dot{D}_\psi R_{wy} \\ (-\psi(V + \dot{D}_x) + \dot{y} + \phi\dot{z} - \dot{D}_\phi R_{wz})/\cos\delta \\ 0 \end{bmatrix}
\end{aligned}$$

where it is assumed that bodies in contact are rigid so that the velocity in the normal direction is zero ($\mathbf{v}_{\text{con}}\big|_z = 0$). By neglecting products of small quantities and using that $V + \dot{D}_x \approx V$, it is found that

$$\mathbf{v}_{\text{con}} \approx \begin{bmatrix} V + (D_\beta + V/r_0)R_{wz} - \dot{D}_\psi R_{wy} \\ (\dot{y} - \psi V - \dot{D}_\phi R_{wz})/\cos\delta \\ 0 \end{bmatrix}$$

Inserting that $\dot{T}_h = V\beta_C$ (see equation (2.3)) one finds

$$\mathbf{v}_{\text{con}} \approx \begin{bmatrix} V + (D_\beta + V/r_0)R_{wz} - \dot{D}_\psi R_{wy} \\ (\dot{D}_y - V D_\psi - \dot{D}_\phi R_{wz})/\cos\delta \\ 0 \end{bmatrix}$$

The angular velocity of the wheelset, in reference to the base of the contact system, is

$$\mathbf{A}_{cb}\boldsymbol{\Omega} = \begin{bmatrix} \dot{D}_\phi \\ (D_\beta + V/r_0)\cos\delta + \dot{D}_\psi \sin\delta \\ -(D_\beta + V/r_0)\sin\delta + \dot{D}_\psi \cos\delta \end{bmatrix}$$

Three creep terms are defined: the longitudinal creep (ξ_x), lateral creep (ξ_y) and spin creep (ξ_s)

$$\xi_x = \frac{\mathbf{v}_{\text{con}}\big|_x}{V} = 1 + \Big((D_\beta + V/r_0)R_{wz} - \dot{D}_\psi R_{wy}\Big)/V \tag{2.21}$$

$$\xi_y = \frac{\mathbf{v}_{\text{con}}\big|_y}{V} = \Big(\dot{D}_y - V D_\psi - \dot{D}_\phi R_{wz}\Big)/(V\cos\delta) \tag{2.22}$$

$$\xi_s = \frac{(\mathbf{A}_{cb}\boldsymbol{\Omega})\,\big|_z}{V} = \Big(\dot{D}_\psi \cos\delta - (D_\beta + V/r_0)\sin\delta\Big)/V \tag{2.23}$$

Creep forces Based on the analysis by Vermeulen and Johnson [102] a heuristic model for the creep forces has been formulated by Shen–Hedrick–Elkins [78]. The model takes into account the important nonlinearity existing between the creep and creep forces. The longitudinal creep force T_x and the lateral creep force T_y are given by

$$T_x = \epsilon\tilde{F}_x \quad , \quad T_y = \epsilon\tilde{F}_y \tag{2.24}$$

$$\begin{bmatrix}\tilde{F}_x\\ \tilde{F}_y\end{bmatrix} = -Gab\begin{bmatrix}C_{11} & 0 & 0\\ 0 & C_{22} & \sqrt{ab}C_{23}\end{bmatrix}\begin{bmatrix}\xi_x\\ \xi_y\\ \xi_s\end{bmatrix}$$

$$\epsilon = |\mathbf{F}|/|\tilde{\mathbf{F}}| \quad , \quad |\tilde{\mathbf{F}}| = \sqrt{\tilde{F}_x^2 + \tilde{F}_y^2}$$

$$|\mathbf{F}| = \begin{cases}\mu N\left(u - \frac{1}{3}u^2 + \frac{1}{27}u^3\right) & u < 3\\ \mu N & u \geq 3\end{cases} \quad , \quad u = \frac{|\tilde{\mathbf{F}}|}{\mu N}$$

The coefficients C_{11}, C_{22} and C_{23} are known as Kalker's creepage coefficients. They depend on a/b and Poisson's ratio ν. Under the assumption of Hertz' theory it is true that $a/b = a_0/b_0$ (see equation 2.20), where a_0 and b_0 are the reference values found from a static consideration of the wheelset. Shen–Hedrick–Elkins' model assumes a small spin creepage and it is not appropriate for studying flange climbing for instance.

Spin moment The spin moment existing around the vertical axis of the contact system is neglected. This is found reasonable due to the simulation scenario, i.e. straight track and curves with large radii (> 500 m), where its magnitude is assumed to be insignificant compared to the other torques acting on the wheelset.

2.2.3 Contact table

Calculating the important contact parameters such as the position of the contact point, the contact angle and the size of contact ellipse is time consuming.

For efficiency reasons it is advantageous to pre–calculate and tabulate the contact parameters and then interpolate this table during simulation. The contact table is generated from a static consideration of the wheelset for different lateral positions using RSGEO [2, 42]. The contact table used has a table entry every $\Delta y = 0.2$ mm in the interval $y \in [-10.0 \text{ mm}; 10.0 \text{ mm}]$. The contact parameters contained in the contact table is shown in Table 2.2.

Column	Description
1	Lateral displacement [mm]
2	Contact angle [rad]
3	Contact point on wheel (lateral, body frame) [m]
4	Contact point on rail (lateral, track frame) [m]
5	Contact point on wheel (vertical, body frame) [m]
6	Contact point on rail (vertical, track frame) [m]
7	Penetration [m]$\cdot 10^6$
8	Normal force [N]
9	ab [m^2]$\cdot 10^6$
10	a/b [–]
11	Kalker's creepage coefficient, C11 [–]
12	Kalker's creepage coefficient, C22 [–]
13	Kalker's creepage coefficient, C23 [–]
14	Kalker's creepage coefficient, C33 [–]

Table 2.2: The parameters contained in the contact table.

In Figure 2.18 to 2.21 some of the contact parameters are shown for the profile combination S1002/UIC60 with 1/40 rail inclination. It is seen that the parameters are discontinuous functions of the lateral displacement of the wheelset.

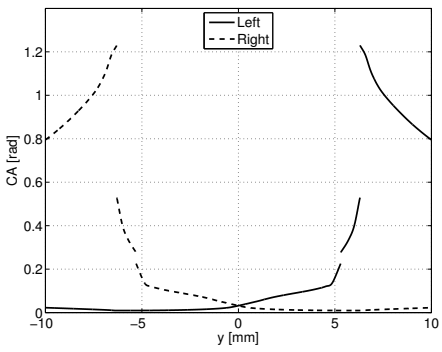

Figure 2.18: Contact angle.

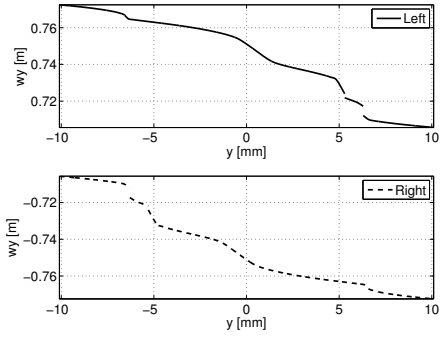

Figure 2.19: Lateral position of contact point on wheel.

The interpolation of the contact table is done using cubic splines on each continuous section of the table. The spline is found using the *Moment representation* [55]. Let x_j, $j = 0, \ldots, n$ and s_j, $j = 0, \ldots, n$ be the nodes and

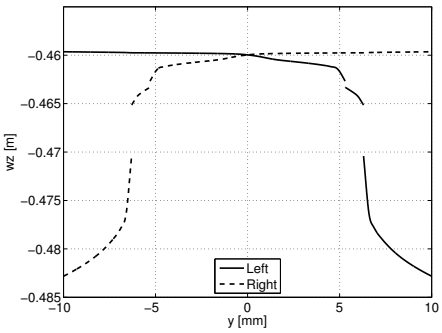

Figure 2.20: Vertical position of contact point on wheel.

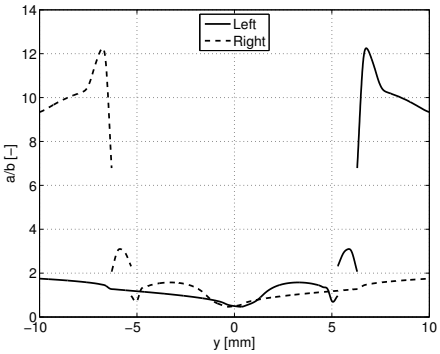

Figure 2.21: a/b

the corresponding contact parameter values, respectively. The node spacing is $h_j = x_j - x_{j-1}$. The spline interpolant is given by

$$\begin{aligned} s(x_{j-1} + h_j t) \quad &= \quad (1-t)(s_{j-1} + \frac{1}{6}h_j^2((1-t)^2 - 1)s''_{j-1}) + t(s_j + \frac{1}{6}h_j^2(t^2-1)s''_j) \\ &\quad j = 1, \ldots, n \quad , \quad 0 \le t \le 1 \end{aligned}$$

where the s''_j is the second derivative of the spline at the j'th node. Imposing natural spline conditions implies that $s''_0 = s''_n = 0$, and the remaining values are found by solving the linear system

$$\begin{bmatrix} 2(h_1+h_2) & h_2 & & \\ h_2 & 2(h_2+h_3) & h_3 & \\ & \ddots & \ddots & \ddots \\ & & h_{n-1} & 2(h_{n-1}+h_n) \end{bmatrix} \begin{bmatrix} s''_1 \\ s''_2 \\ \vdots \\ s''_{n-1} \end{bmatrix} = \begin{bmatrix} d_1 \\ d_2 \\ \vdots \\ d_{n-1} \end{bmatrix} \tag{2.25}$$

where

$$d_j \equiv 6\left(\frac{s_{j+1} - s_j}{h_{j+1}} - \frac{s_j - s_{j-1}}{h_j}\right) \quad , \quad j = 1, \ldots, n-1$$

The s''_j are also tabulated before simulation.

2.2.4 Multiple contacts

Due to the elastic properties of the wheel and rail, the discontinuities in the contact table often correspond to situations where multiple contacts on the same wheel are likely to occur. For instance, double contact is typical for a wheel approaching the flange. In this situation one contact point will be present on the tread and another on the flange. Inspired by the work of Pascal and Sauvage [70, 58] the discontinuities are treated by having an overlap region around the discontinuities in which multiple contacts occur. Most of the contact parameters in the overlap region are found by extrapolating the two splines surrounding the

discontinuity as illustrated in Figure 2.22. The extrapolation should be done with care because it might diverge rapidly far from the interpolating nodes, however, since the overlap region is small (about 0.2 mm) it is found suitable. The normal force (N_0) and the product of the semi–axes ($a_0 b_0$) should behave differently because the wheel load should be distributed between the contact points. In order to gradually transfer the load from one contact point to the other one a linear decay is imposed on these parameters in the region as shown in Figure 2.23. The contacts in the overlap region are treated separately using the models described previously and they are assumed to be independent.

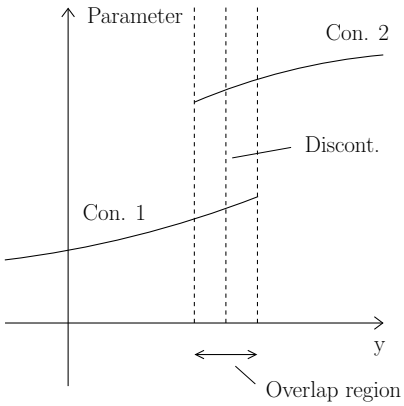

Figure 2.22: Extrapolation.

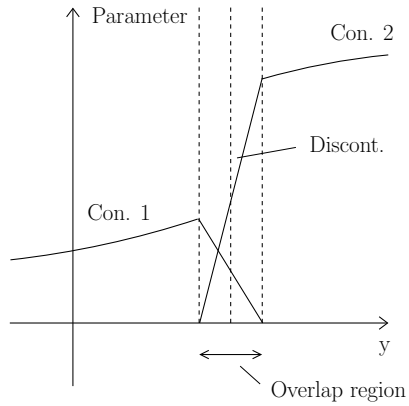

Figure 2.23: Linear decay.

The contact model is divided into states, and the discontinuous jumps in the contact parameters are located during simulation. For example, the discontinuity representing the flange would naturally lead to the following state division: a state with tread contact only, a state for the overlap region, a state with flange contact only. Generally, the i'th state is defined by $y \in [y_{i,lo}; y_{i,hi}]$ where y is the lateral position of the wheelset. The state machine for the wheel–rail contact model is shown in Figure 2.24.

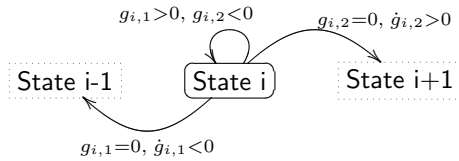

$$\boxed{\begin{aligned} g_{i,1} &= y - y_{i,lo} \\ g_{i,2} &= y - y_{i,hi} \end{aligned}}$$

Figure 2.24: Wheel–rail state machine.

2.3 UIC standard suspension

The European standard suspension system for two–axle freight wagons is called the UIC standard suspension, see Figure 2.25. It consists of a leaf spring and a link system. The deflection of the leaves yields the stiffness, and dissipative dry friction forces are generated in between the leaves. The link system works as a pendular suspension system for the horizontal motion. Dry friction in the support of the link elements provides the necessary damping for the horizontal motion. The only damping mechanism in the UIC suspension is dry friction. Motion delimiters also exist to guide the axle box. The axle guidance basically restricts the relative motion between carbody and wheelset by end stops causing impacts.

The design of this suspension system became a standard in Germany in 1890 and has since then been widely used both in Europe and Japan. It is advantageous because it is simple, cheap and robust.

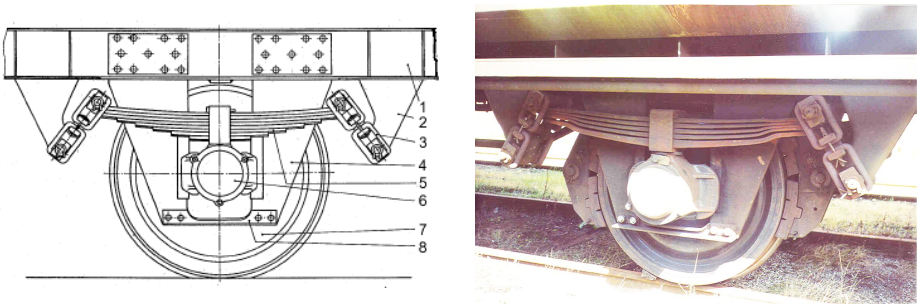

Figure 2.25: UIC standard suspension 1) Carbody 2) Suspension bracket 3) UIC links 4) Axle guidance 5) Leaf spring 6) Axle bearing 7) Wheelset 8) Connecting bar.

The motion of the freight wagon is to a high degree influenced by the suspension system. Therefore, the suspension model automatically becomes an important aspect of the multibody model. By nature, the suspension characteristics are nonlinear and even nonsmooth. This is a consequence of the dry friction and impacts present in the suspension system. In the following, the suspension model is described in detail. An appropriate and reasonable division of the suspension system is into its longitudinal, lateral and vertical characteristics. They are treated independently. The suspension elements in the multibody model are situated as illustrated in Figure 2.26 and 2.27.

2.3.1 Suspension deformation

The suspension models are formulated as a function of the suspension deformation and its derivative. The results derived previously in equation (2.6) and (2.7) can be used directly in order to express the needed quantities. It is utilised that

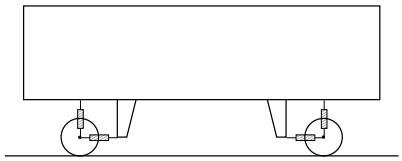

Figure 2.26: Side view.

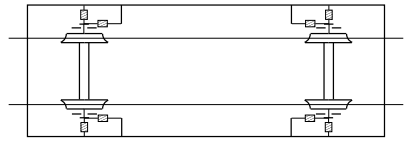

Figure 2.27: Top view.

the suspension is attached to the axle box in a position having $x_{Pw} = z_{Pw} = 0$. The deformation and its derivative are

$$\Delta\mathbf{r} \approx \begin{bmatrix} D_{xw} - y_{Pw}D_{\psi w} - (\bar{z}_{cb}\theta_{Ccb} - \bar{y}_{cb}\beta_{Ccb} - y_{Pcb}D_{\psi cb} + z_{Pcb}D_{\theta cb}) \\ D_{yw} - (D_{ycb} + x_{Pcb}D_{\psi cb} - z_{Pcb}D_{\phi cb}) \\ D_{zw} + y_{Pw}D_{\phi w} - (D_{zcb} - x_{Pcb}D_{\theta cb} + y_{Pcb}D_{\phi cb}) \end{bmatrix} \tag{2.26}$$

$$\Delta\dot{\mathbf{r}} \approx \begin{bmatrix} \dot{D}_{xw} - y_{Pw}\dot{D}_{\psi w} - (\bar{z}_{cb}V/\rho_{vcb} - \bar{y}_{cb}V/\rho_{hcb} - y_{Pcb}\dot{D}_{\psi cb} + z_{Pcb}\dot{D}_{\theta cb}) \\ \dot{D}_{yw} - (\dot{D}_{ycb} + x_{Pcb}\dot{D}_{\psi cb} - z_{Pcb}\dot{D}_{\phi cb}) \\ \dot{D}_{zw} + y_{Pw}\dot{D}_{\phi w} - (\dot{D}_{zcb} - x_{Pcb}\dot{D}_{\theta cb} + y_{Pcb}\dot{D}_{\phi cb}) \end{bmatrix} \tag{2.27}$$

Note, that the above expressions are in reference to the track base of the carbody. The suspension deformation vector, $\Delta\mathbf{r}$, is a vector from the attachment point on the carbody to the attachment point on the wheelset.

2.3.2 Leaf spring

A leaf spring is constructed by layering several leaves on top of each other. The leaves are clamped together by a simple device in the middle of the leaf spring. The curvature of the leaves are all different such that small clearances are present in between the leaves. The basic function of the leaf spring is that bending of the leaves generates the suspension stiffness while the dry friction in between the leaves provides the damping. The leaf springs found on todays freight wagons are either of the trapezoidal or parabolic type, see Figure 2.28 and 2.29. The parabolic leaf spring differs from the trapezoidal leaf spring in that the leaf design is parabolic (optimal material utilisation), it is lighter, additional spacing in between the leaves and the leaves all have the same length. The parabolic leaf spring is often used on modern freight wagons and has several advantages [71], e.g. longer lifetime, better structural design possibilities, lower weight due to better material utilisation and constant spring characteristics during its lifetime.
The parabolic leaf spring shown in Figure 2.29 is a so called two–stage parabolic leaf spring. It has an additional leaf to support heavy loads.

Modelling the leaf spring is challenging because the nonsmooth stick–slip transitions and the interaction with the additional leaf (for the two–stage type) generate the complex suspension characteristics with hysteresis known from leaf springs. An example of such a hysteresis loop is illustrated in Figure 2.30 [71].

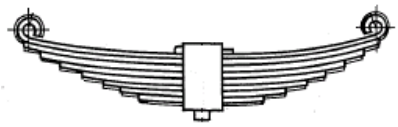

Figure 2.28: Trapezoidal.

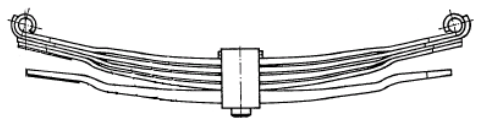

Figure 2.29: Two–stage parabolic.

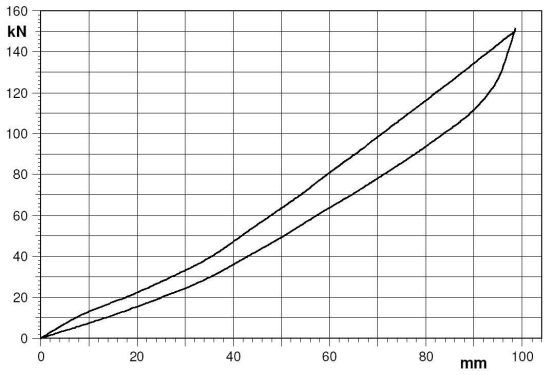

Figure 2.30: Example of a hysteresis loop for a two–stage parabolic leaf spring.

The hysteresis loop reveals that the damping and effective spring rate both depend on the excitation amplitude and nominal static load, i.e.: 1) The damping increases if either the excitation amplitude or nominal static load is increased 2) The effective spring rate decreases if the excitation amplitude is increased or the nominal static load is decreased. Another important property, which has been experimentally verified by the work in [14], is that the spring characteristics are not influenced by the excitation frequency in the range 0 to 15 Hz.

The model developed in order to simulate the above mentioned characteristics is based on the work in [14, 7]. The aim is to have a general model that can be used for both the trapezoidal leaf spring and two–stage parabolic leaf spring, and the specific type is then controlled through the model parameters. The restoring force from the leaf spring is expressed by the following differential equation [14, 7]

$$\frac{\partial F}{\partial \delta} = \frac{F_{\text{env}} - F}{\beta} \tag{2.28}$$

where F is the spring force, F_{env} is an envelope function, δ is the spring deflection and β is a decay constant. The envelope function defines the upper and lower boundaries of the hysteresis loop, and the decay constant determines how steep the transition between the boundaries should be. In other words, the *static* spring stiffness is controlled by the envelope function, and the *dynamic* spring

stiffness is controlled by the decay constant. Equation (2.28) is multiplied with $\dot{\delta}$

$$\dot{F} = \frac{F_{\text{env}} - F}{\beta}\dot{\delta} \tag{2.29}$$

which will be used in the mathematical model of the dynamics of the wagon. A proper formulation of the envelope function is found to be

$$F_{\text{env}} = \begin{cases} c_h(1+\mu_0)z + F_r & z \le z_0,\ \dot{z} \ge 0 \quad \text{(loading)} \\ c_z(1+\mu_0)(z-z_*) + F_r & z \ge z_0,\ \dot{z} \ge 0 \quad \text{(loading)} \\ c_z(1-\mu_0)(z-z_*) - F_r & z \ge z_0,\ \dot{z} \le 0 \quad \text{(unloading)} \\ c_h(1-\mu_0)z - F_r & z \le z_0,\ \dot{z} \le 0 \quad \text{(unloading)} \end{cases} \tag{2.30}$$

Here, c_h is the spring stiffness with an inactive additional leaf, c_z is the spring stiffness with an active additional leaf, μ_0 is a friction parameter, z is the deformation of the spring, z_0 is the position of the additional leaf and F_r is the residual spring force. The deflection and deformation are related by $\delta = |z|$. For two–stage leaf springs z_0 is finite, and for one–stage leaf springs $z_0 = \infty$. Furthermore, z_* is determined from

$$z_* = \begin{cases} (1 - c_h/c_z)z_0 & 0 < z_0 < \infty \\ 0 & z_0 = \infty \end{cases}$$

The leaf spring model is divided into the four natural states named and shown in Table 2.3.

State	Description
LoadingH	$z \le z_0,\ \dot{z} \ge 0$
LoadingHZ	$z \ge z_0,\ \dot{z} \ge 0$
UnloadingHZ	$z \ge z_0,\ \dot{z} \le 0$
UnloadingH	$z \le z_0,\ \dot{z} \le 0$

Table 2.3: Leaf spring states.

Hence, the envelope function becomes

$$F_{\text{env}} = \begin{cases} c_h(1+\mu_0)z + F_r & \text{LoadingH} \\ c_z(1+\mu_0)(z-z_*) + F_r & \text{LoadingHZ} \\ c_z(1-\mu_0)(z-z_*) - F_r & \text{UnloadingHZ} \\ c_h(1-\mu_0)z - F_r & \text{UnloadingH} \end{cases}$$

and the resulting model is

$$\dot{F} = \frac{\dot{z}}{\beta}\begin{cases} c_h z - F + c_h\mu_0 z + F_r & \text{LoadingH} \\ c_z(z-z_*) - F + c_z\mu_0(z-z_*) + F_r & \text{LoadingHZ} \\ -(c_z(z-z_*) - F) + c_z\mu_0(z-z_*) + F_r & \text{UnloadingHZ} \\ -(c_h z - F) + c_h\mu_0 z + F_r & \text{UnloadingH} \end{cases} \tag{2.31}$$

The right hand side of equation (2.31) is nonsmooth due to the loading / unloading transitions and the interaction with the additional leaf. In order to properly integrate past these transitions, it is necessary to locate the transition points defined by the functions $\dot{z} = 0$ and $z - z_0 = 0$. On the other hand, close to equilibrium it can be utilised that the loading / unloading transitions are approximately smooth due to

$$\begin{aligned} c_h z - F &\approx 0 \qquad z \le z_0 \quad , \quad |\dot{z}| \ll 1 \\ c_z(z - z_*) - F &\approx 0 \qquad z \ge z_0 \quad , \quad |\dot{z}| \ll 1 \end{aligned}$$

Thus, close to equilibrium it is valid that

$$\dot{F} \approx \frac{\dot{z}}{\beta} \begin{cases} c_h \mu_0 z + F_r & z \le z_0 \\ c_z \mu_0 (z - z_*) + F_r & z \ge z_0 \end{cases}$$

The measure for *close to* equilibrium is

$$\begin{aligned} |c_h z - F| &< F_{\text{tol}} \qquad z \le z_0 \\ |c_z(z - z_*) - F| &< F_{\text{tol}} \qquad z \ge z_0 \end{aligned}$$

To further enhance the performance of the numerical integration equation (2.31) is normalised with the static spring load ($m_{cb}g/4$). The state machine of the model is shown in Figure 2.31.

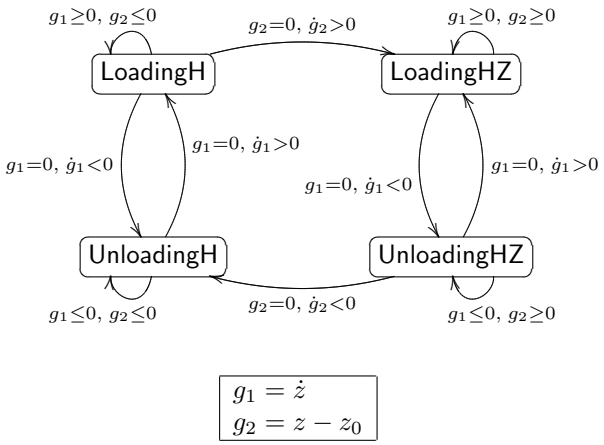

Figure 2.31: State machine of the leaf spring model.

Trapezoidal leaf spring To model the trapezoidal leaf spring the following parameters are used: $\beta = 3.0$ mm, $\mu_0 = 0.10$, $c_h = c_z = 1.1$ MN/m, $F_r = 7$ kN, $F_{\text{tol}} = 5$ kN, $z_0 = \infty$. The decay constant is chosen such that the dynamic

stiffness factor, $k_{\mathrm{dyn}}/k_{\mathrm{stat}}$, is about 5. In Figure 2.32 and 2.33 the results from a harmonic excitation are shown. The characteristic hysteresis loop from the leaf spring is modelled as expected.

A simulation of a mass (7500 kg) finding its equilibrium on the leaf spring is investigated next. The time history of the simulation is shown in Figure 2.34 together with the hysteresis loop. The hysteresis loop depicts the normalised restoring force. Note, that the events are only detected far from equilibrium (Figure 2.34), and that no additional integration steps are taken in order to pass the corners (Figure 2.35).

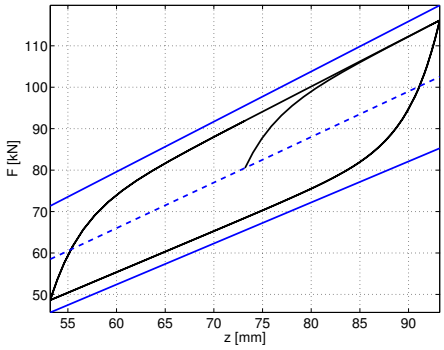

Figure 2.32: 20 mm amplitude.

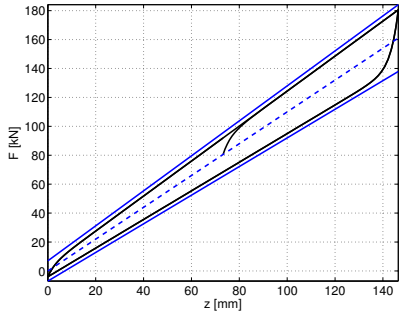

Figure 2.33: 73.2 mm amplitude.

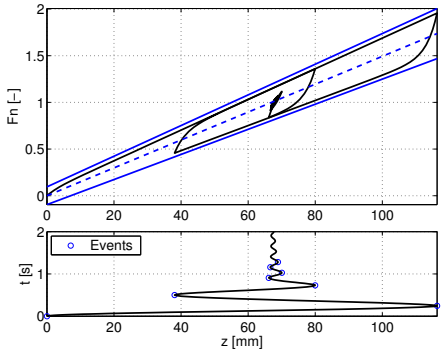

Figure 2.34: Simulation with a mass on the leaf spring.

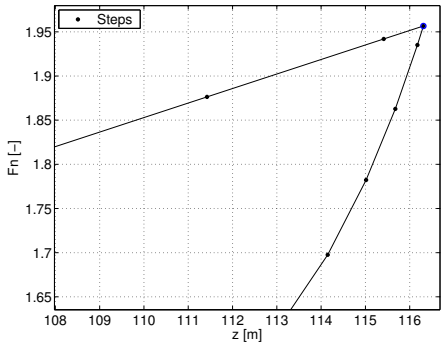

Figure 2.35: Integrating the corner.

Two–stage parabolic leaf spring The following parameters are used: $\beta = 2.0$ mm, $\mu_0 = 0.075$, $c_h = 0.65$ MN/m, $c_z = 1.82$ MN/m, $F_r = 7$ kN, $F_{\mathrm{tol}} = 5$ kN, $z_0 = 62.9$ mm. The results by simulating a mass on this spring is shown in Figure 2.36 and 2.37. The effect of the additional leaf is clearly visible. Note,

the different equilibrium positions for the two different masses. One important property that leaf springs exhibit is that small amplitude oscillations are rather poorly damped. In Figure 2.38 and 2.39 the time history by simulating the mass of 7500 kg in 6 s is shown. Note, how the large amplitude oscillations are adequately damped (Figure 2.38), and that the small amplitude oscillations sustain for a while (Figure 2.39). The physical explanation for this phenomenon is that the leaves are practically all sticking to each other and no frictional energy is released. A linear model will not resemble this because the oscillations are damped exponentially at all times.

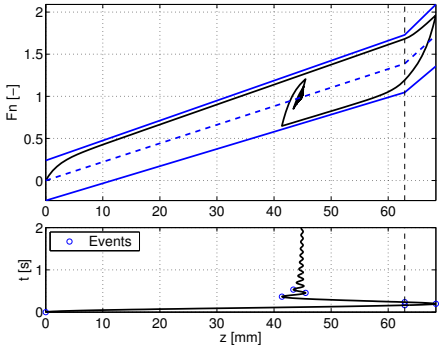

Figure 2.36: $m = 3000$ kg.

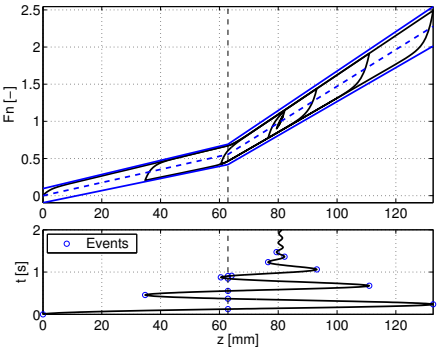

Figure 2.37: $m = 7500$ kg.

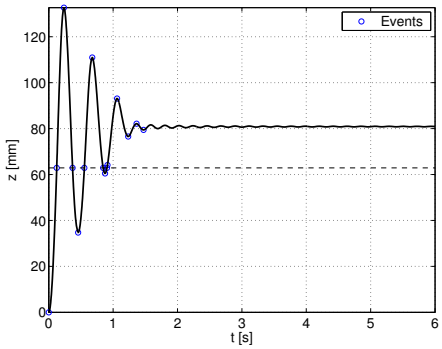

Figure 2.38: $m = 7500$ kg.

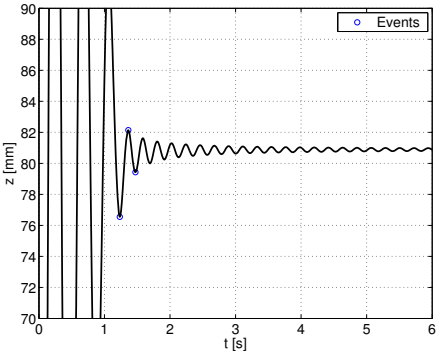

Figure 2.39: Zoomed view.

2.3.3 UIC double–link connection

The carbody is connected to the leaf spring through the UIC double–link connection (UIC links), see Figure 2.40. The link system works as a pendular suspension system with friction. The double–link type used for two–axle wagons provides a relatively soft horizontal suspension giving the wheelset a larger freedom to position itself radially in curves. The suspension damping stems from the dry friction in the joints. The clearance of 10 mm between the lower link and the suspension bracket, see Figure 2.41, makes the suspension stiffness stepwise progressive. This is due to the fact that the pendulum length is halved when the clearance is exceeded.

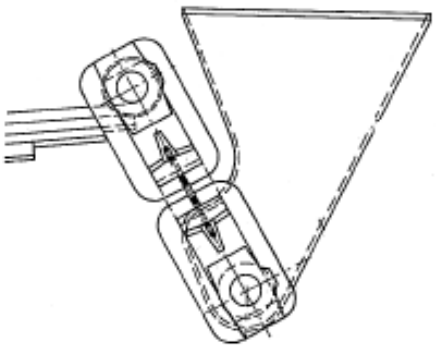

Figure 2.40: UIC links.

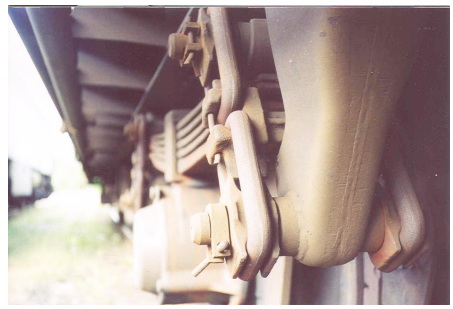

Figure 2.41: Clearance between the lower link and the suspension bracket.

The UIC double–link connection provides a very robust suspension system with low maintenance costs. The disadvantages are its sensitivity to the friction coefficient in the joints and wear of the link elements. These quantities are not easy to control and in general influenced by external factors. For instance, the current weather conditions and the amount of dirt and oil in the joints affect the friction coefficient. A high friction coefficient might prevent sliding in the joints such that no energy is dissipated. It is also reported [36] that the rolling stiffness of the links often increases by wear. This naturally also influences the suspension characteristics and eventually the dynamic performance of the wagon.

Technical pendulum The technical pendulum distinguishes itself from the mathematical pendulum in that rolling and sliding in the joint is taken into account. The UIC links can be considered as a system composed of technical pendulums. See the illustrations in Figure 2.42 to 2.44. Two variants of the technical pendulum appear in studying the UIC links: the fixed pivot type (Figure 2.45) and fixed hub type (Figure 2.46). In the longitudinal direction the end bearing is rolling over the pin (fixed pivot), and in the lateral direction the

link is rolling in the end bearing (fixed hub). It is noted that the design of the end bearings decouples the longitudinal and lateral suspension characteristics. The basic characteristics of the UIC links can be extracted by investigating the technical pendulum.

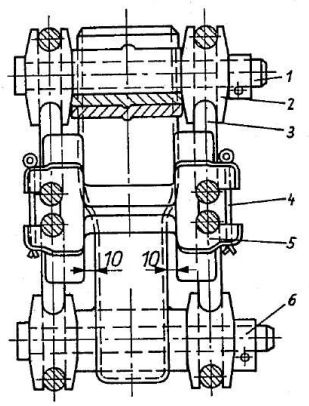

Figure 2.42: UIC links. 1) Pin 2) End bearing 3) Link 4) Split 5) Intermediate bearing 6) C–washer.

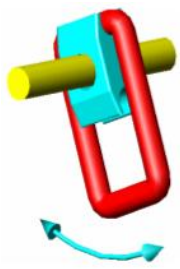

Figure 2.43: Longitudinal.

Figure 2.44: Lateral.

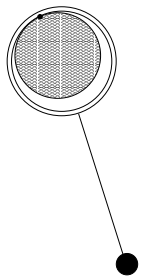

Figure 2.45: Fixed pivot.

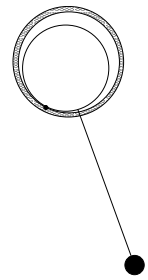

Figure 2.46: Fixed hub.

In [61] it is shown that a proper model of the technical pendulum is a linear spring in parallel with an elastic element with dry friction, see Figure 2.47. The dry friction slider obeys Coulomb's friction law (Figure 2.48). It is shown in [61] that the spring stiffnesses (k and k_1) depends only on geometry, i.e. pendulum length and radii of the elements, but not the coefficient of friction. Moreover, the break out force (T_0) is almost proportional to the coefficient of friction between the elements.

Exciting this suspension model harmonically yields the hysteresis loop shown in Figure 2.49. Starting at zero displacement the restoring force increases with

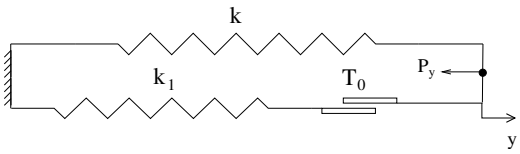

Figure 2.47: Model of the technical pendulum.

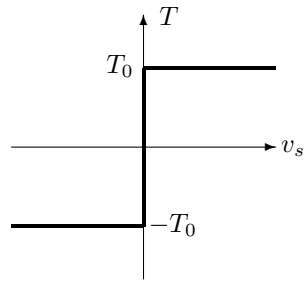

Figure 2.48: Coulomb's friction law.

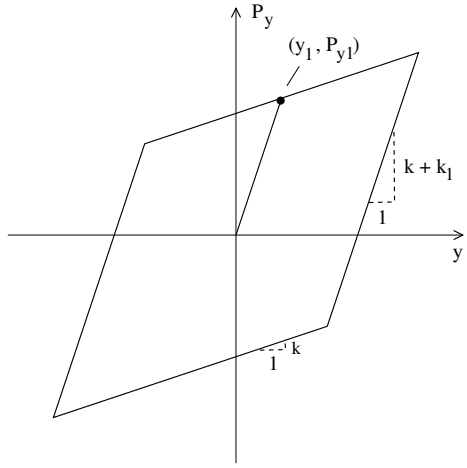

Figure 2.49: Hysteresis loop.

the gradient of $k + k_1$ because the friction slider sticks and thus both springs are working. At the point (y_1, P_{y1}) the friction limit of $T_0 = k_1 y_1$ is saturated. Hereafter, the friction slider begins to slide and the model stiffness immediately drops to k since the spring in series with the dry friction slider is inactive. As soon as the direction of the excitation is reversed the dry friction slider sticks meaning that the model stiffness is $k + k_1$ again. This pattern is then repeated over again. Note, how the model parameters easily can be identified from the hysteresis loop, i.e. the model stiffnesses are given by the gradient of the different parts of the loop and the friction limit is found by $T_0 = k_1 y_1$.

The model can be verified by measuring the hysteresis loop using the procedure described in [62]. Moreover, it also provides a simple method for identifying the model parameters. A technical pendulum is instrumented with an inertial accelerometer and a displacement sensor like in Figure 2.50 and 2.51. The output of the inertial accelerometer can be divided into two constributions: 1) The acceleration due to the motion of the mass m which is $g \tan\gamma \cos\phi$. 2) The acceleration due to the fact that the mass within the inertial accelerometer is exposed to gravity, i.e. $g \sin\phi$. The measured acceleration is therefore

$$\eta = g(\tan\gamma \cos\phi - \sin\phi)$$

The (normalised) restoring force can be computed using the identity in equation (2.32).

$$\frac{P_y}{mg} = \tan\gamma \quad , \quad \tan\gamma = \tan\phi + \frac{\eta}{g\cos\phi} \tag{2.32}$$

The sway angle ϕ is found by recording the displacement z together with the identity $\phi = \arctan(z/b)$, and η is the measured tangential acceleration. The experiment is performed by releasing the pendulum from a nonzero sway angle configuration and then recording the quantities z and η while the pendulum is freely swaying. The measured sway angle for an experiment in the longitudinal direction with real UIC elements is shown in Figure 2.52, and the measured hysteresis loop is shown in Figure 2.53.

The measurements reveal an important property of the UIC links: there is practically no damping if the elements are rolling over each other. This is the typical situation for small amplitude excitations. On the other hand, dissipative dry friction forces sets in if the amplitude exceeds a certain magnitude because the link elements are sliding.

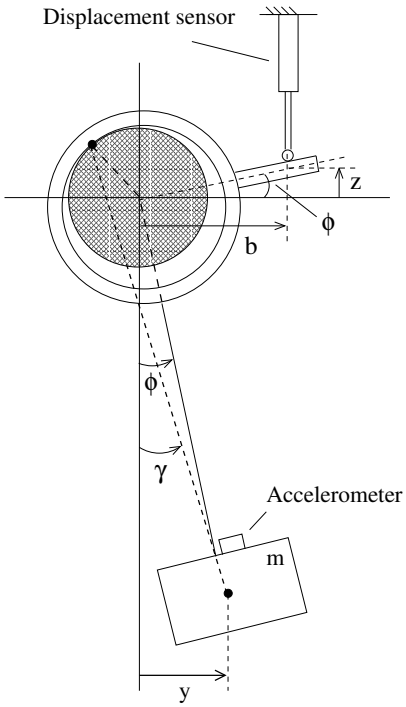

Figure 2.50: Technical pendulum (fixed pivot type).

Figure 2.51: Experimental setup.

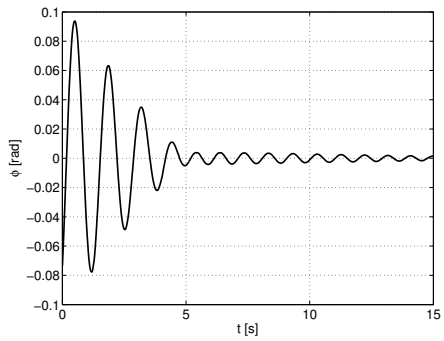

Figure 2.52: Sway angle.

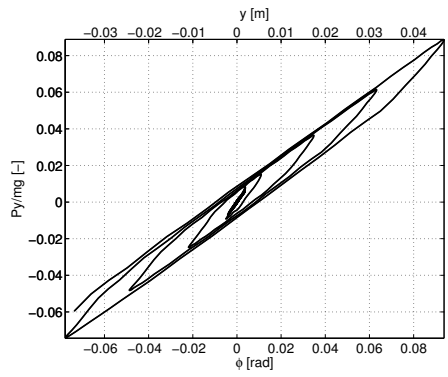

Figure 2.53: Hysteresis loop.

Cylindrical elements A proper model for the UIC links with (nominal) cylindrical geometry has been developed by Piotrowski [61]. The model is shown in Figure 2.54 and 2.55. Both longitudinally and laterally the model is characterised by a linear spring in parallel with elastic elements with dry friction. The friction sliders obey Coulomb's friction law and the coefficient of friction is assumed to be the same in all joints. In the lateral direction, the interaction with the suspension bracket is modelled by a linear spring with a dead band.

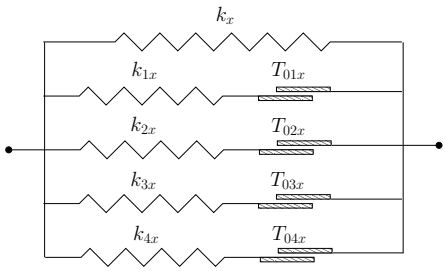

Figure 2.54: Longitudinal direction.

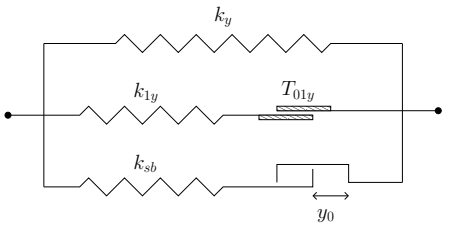

Figure 2.55: Lateral direction.

The mathematical formulation is presented in equation (2.33) and (2.34). The force from the elastic element with dry friction is determined from the state dependent differential equation shown in equation (2.35). The corresponding state machine is shown in Figure 2.56. The force from the dead band spring is found using equation (2.36) and the state machine in Figure 2.57.

$$F_x(\xi \equiv x) = -k_x\xi + \sum_{i=1}^{4} T_{ix} \tag{2.33}$$

$$F_y(\xi \equiv y) = -k_y\xi + T_{1y} + F_{sb} \tag{2.34}$$

$$\dot{T}_i(\xi) = \begin{cases} -k_i\dot{\xi} & \text{Stick} \\ 0 & \text{SlidePos/SlideNeg} \end{cases} \tag{2.35}$$

$$F_{sb}(y) = \begin{cases} 0 & \text{Idle} \\ -k_{sb}(y - y_0) & \text{SpringPos} \\ -k_{sb}(y + y_0) & \text{SpringNeg} \end{cases} \tag{2.36}$$

Measurements Measurements of the lateral characteristics have been performed on a worn suspension. The measurements were carried out at the Institute of Vehicles, Warsaw University of Technology, with the aid of Prof. J. Piotrowski and Ph.D. A. Grzelak. The complete experiment setup with instrumentation is illustrated in Figure 2.58 to 2.61. The suspension is loaded by a mass of 378.2 kg. It is assumed that the normalised suspension characteristics,

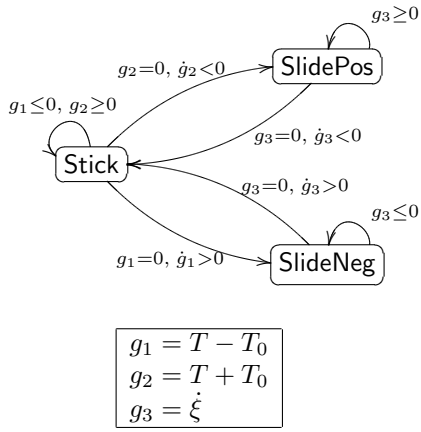

Figure 2.56: Dry friction element.

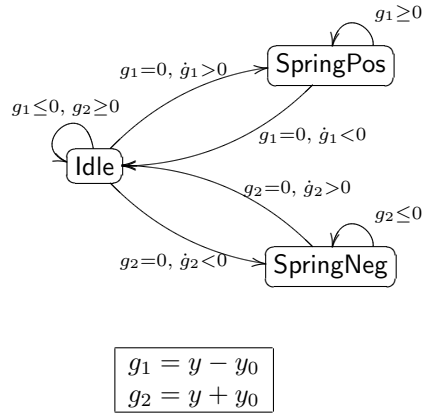

Figure 2.57: Dead band spring.

i.e. the restoring force normalised with the suspension load as a function of the suspension displacement, is independent of the excitation frequency and the suspension load. This assumption is found reasonable based on the experiments shown in [36]. Measuring the hysteresis loop directly from a freely swaying suspension, like in the case with the technical pendulum, is not appropriate here because the dissipation is strong and therefore it is not possible to get a sufficient amount of loops. Instead, the suspension is excited at its eigenfrequency (about 1 Hz) being a typical operating condition. An electrical motor provides the external excitation, $g(t)$, with constant amplitude. This excitation is transferred to the suspension mass through a spring with unknown characteristic. The suspension is then further in connection with fixed ground through the UIC links. Three quantities are measured during the experiment: the external force, F_{motor}, acceleration of the mass, η, and displacement of the mass, y. Newton's second law yields the following equation from which the restoring force, P_y, from the UIC links can be computed.

$$P_y = m\eta - F_{\text{motor}} \tag{2.37}$$

In short the procedure of the experiment is:

1. Attach the sensors such that they are measuring according to Figure 2.58.
2. If not done previously then calibrate sensors (see below).
3. Tune motor until the measured force is at minimum amplitude.
4. Start measurement.

Calibration of the displacement sensor:

- Put the system in equilibrium position.
- Set displacement sensor in appropriate position.
- Set zero for the sensor in software. *Advantech–Grapol*: Calibration/**Shift+F1**.
- Calibrate the sensor by putting the Johanson–piece (or other material of known dimensions) between the sensor and mass. Enter this state into the program. *Advantech–Grapol*: Calibration/**Shift+F2**.
- Enter the calibration distance of this sensor into the program. *Advantech–Grapol*: Calibration/**Shift+F3**.

Calibration of the (inertial) accelerometer:

- Put the accelerometer in level position (make sure that the surface is really horizontal).
- Enter the zero into program. *Advantech–Grapol*: Calibration/**Shift+F1**.
- Turn the accelerometer 90 degrees and expose it to 1 g. Enter this state into program. *Advantech–Grapol*: Calibration/**Shift+F2**.
- Enter the calibration distance into program, e.g. 1 g. Remember that this means that the acceleration is measured in g's. *Advantech–Grapol*: Calibration/**Shift+F3**.

Calibration of the force sensor:

- Put the force sensor in horizontal position without exposing it to any force, and set zero. *Advantech–Grapol*: Calibration/**Shift+F1**.
- Find some mass of known weight (it is necessary to know the weight accurately).
- Attach this mass to the sensor and put the sensor in vertical position. Enter this state into program. *Advantech–Grapol*: Calibration/**Shift+F2**.
- Enter the calibration force into program, e.g. 4 kilos, and remember that the sensor is now measuring in kilos. The force is eventually found by multiplication with g (since the calibration was done in vertical position). *Advantech–Grapol*: Calibration/**Shift+F3**.

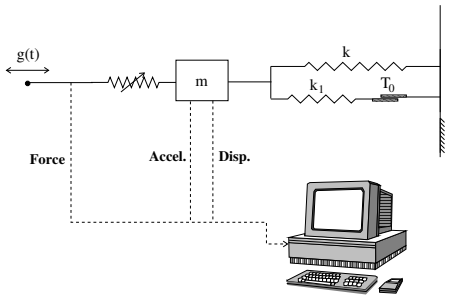

Figure 2.58: Experimental setup diagram.

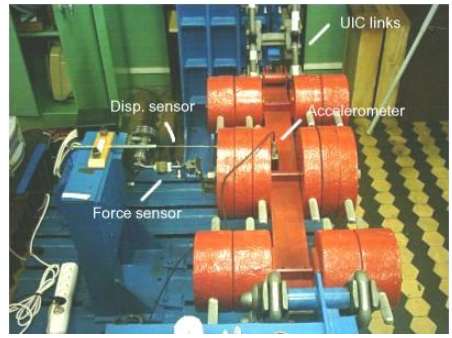

Figure 2.59: Overview.

The measured acceleration signal is slightly delayed compared to the displacement signal, see Figure 2.62. Physically, they are in phase, however, due to the internal suspension properties of the inertial accelerometer the effect will be present in the measured signal. The measurements are performed at approximately 1 Hz and the eigenfrequency of the inertial accelerometer is 19 Hz so the

Figure 2.60: Side view.

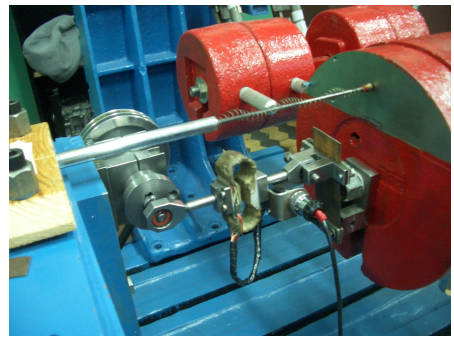

Figure 2.61: Force and displacement sensor.

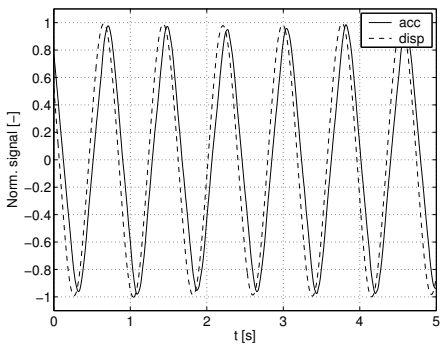

Figure 2.62: Delay in accelerometer.

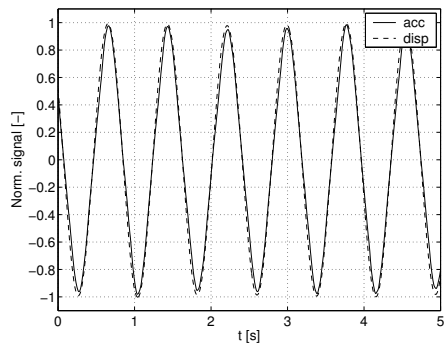

Figure 2.63: Adjusted signals.

effect is small. However, it is important to adjust the delay because the resulting hysteresis loop is sensitive to the effect. The adjusted signal is illustrated in Figure 2.63. The delay does not affect the measured hysteresis loop from the technical pendulum because it is modulated by the sway angle through the formula in equation (2.32).

The measured hysteresis loop for four different measurements is shown in Figure 2.64 to 2.67. It is seen that there is a gradual transition between rolling and sliding in the joints. An explanation of this could be a different coefficient of friction in the joints such that the link elements starts to slide at different instants. A comparison between an excitation with a small and high amplitude is shown in Figure 2.68. The measurement with the small excitation is very lightly damped resulting in the very thin hysteresis loop.

To model the measured hysteresis loop it has been found necessary to introduce several dry friction sliders in order to resemble the gradual transition from rolling to sliding in the suspension. The model is shown in equation (2.38) and Figure 2.69. A comparison between a measured hysteresis loop and a simulated one is compared in Figure 2.70.

$$F_y(\xi \equiv y) = -k_y \xi + F_{sb} + \sum_{i=1}^{4} T_{iy} \tag{2.38}$$

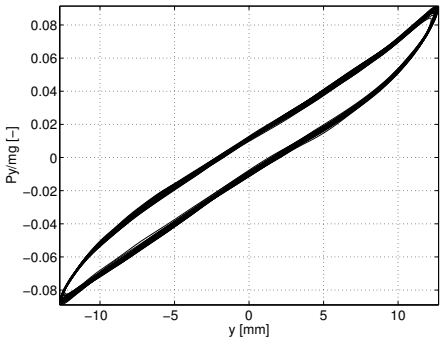

Figure 2.64: Measured hysteresis loop (1).

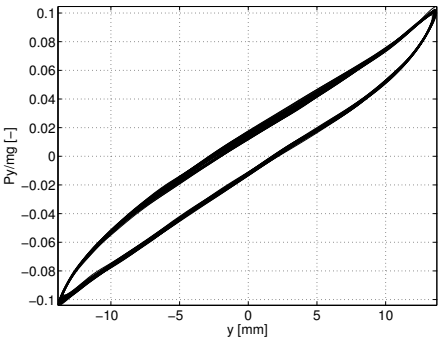

Figure 2.65: Measured hysteresis loop (2).

Suspension parameters In several studies [61, 12, 81, 36, 85] models similar to the one presented here (Figure 2.54, 2.55 and 2.69) have been used to simulate the UIC links, however, the actual parameters used in the literature are widely different. In particular, this is true for the parameters related to the elastic dry friction elements (determining the behaviour of the rolling phase of the links). A possible explanation for this is the influence of wear on the rolling stiffness.

Different parameter sets are used to be able to investigate their influence on the dynamic performance of the wagon, see Table 2.4 and 2.5. The parameters

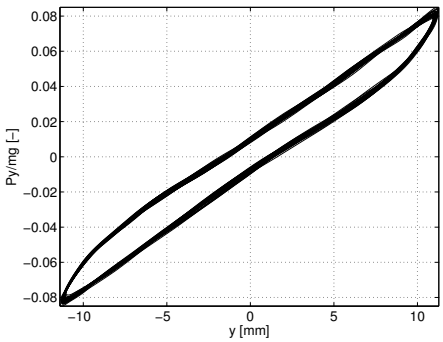

Figure 2.66: Measured hysteresis loop (3).

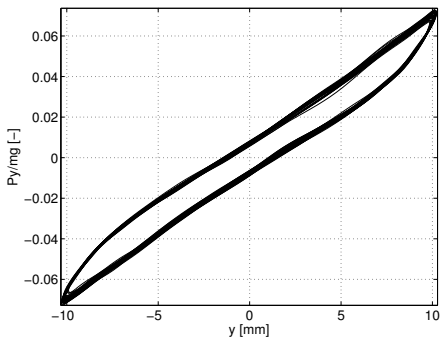

Figure 2.67: Measured hysteresis loop (4).

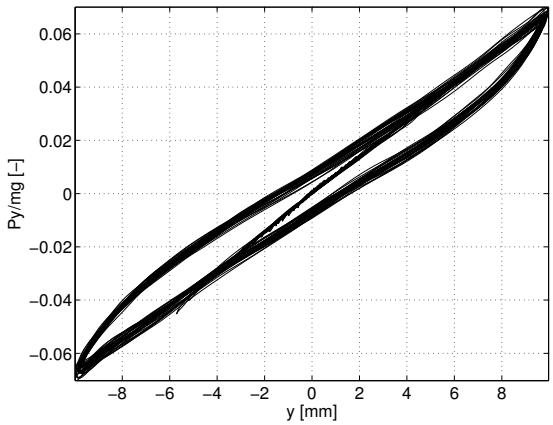

Figure 2.68: Comparison between a high and low amplitude excitation.

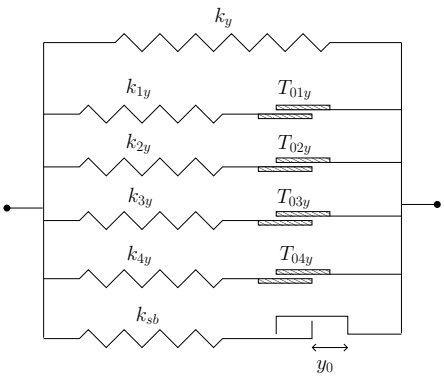

Figure 2.69: Model of the measured hysteresis loop.

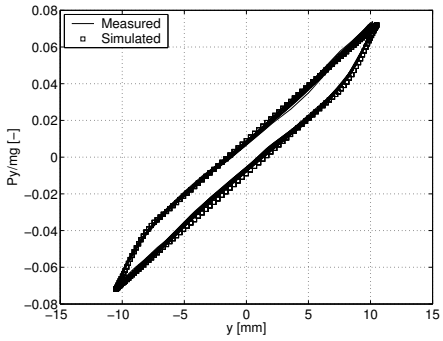

Figure 2.70: Comparison between model and measurements.

are normalised with the suspension load. The PTP set is taken from [61] and is the basic reference set. They are found from a theoretical consideration of the links with a cylindrical geometry and a friction coefficient of 0.3 between the links. It is appropriate as a reference because they model an idealised configuration with UIC elements having cylindrical geometry. The parameter set SPP is the proposed suspension characteristics from [80], the parameter set INP is from [12] and ASZ has been used in relation to the work [85]. The parameter set MP includes the previously described measured characteristics in the lateral direction, and the theoretical ones [61] are used in the longitudinal direction.

The parameter k_{sb} is put equal to k_y such that the pendulum stiffness is doubled when the clearance is exceeded, and the clearance is $y_0 = 0.01$ m.

		k [1/m]	k_1 [1/m]	k_2 [1/m]	k_3 [1/m]	k_4 [1/m]
PTP	x	5.51	3.56	1.90	0.35	1.86
	y	3.406	10.375	–	–	–
SPP	x	4.50	25.00	–	–	–
	y	4.90	20.00	–	–	–
INP	x	4.60	22.99	–	–	–
	y	4.60	13.79	–	–	–
ASZ	x	2.70	32.00	15.70	4.10	–
	y	4.00	52.00	8.00	–	–
MP	x	5.51	3.56	1.90	0.35	1.86
	y	6.00	2.00	2.00	2.00	2.00

Table 2.4: Normalised stiffness parameters.

		T_{01} [–]	T_{02} [–]	T_{03} [–]	T_{04} [–]
PTP	x	0.02103	0.01425	0.00278	0.02059
	y	0.053	–	–	–
SPP	x	0.08	–	–	–
	y	0.10	–	–	–
INP	x	0.07	–	–	–
	y	0.07	–	–	–
ASZ	x	0.016	0.037	0.020	–
	y	0.040	0.064	–	–
MP	x	0.02103	0.01425	0.00278	0.02059
	y	0.0015	0.0020	0.0025	0.0030

Table 2.5: Normalised friction limits.

2.3.4 Axle guidance

The motion of the axle box is restricted by the axle guidance, see Figure 2.71. The axle guidance works as a motion delimiter both in longitudinal and lateral direction. The longitudinal clearance is 22.5 mm and the lateral is 20.0 mm. Like the axle box, the axle guidance is made of steel. If the longitudinal clearance is exceeded, a hard steel to steel impact occurs due to the construction of the axle guidance. In the lateral direction, the axle guidance yields a relatively soft elastic response because the axle guidance bends. Hence, the lateral behaviour can be considered as an additional suspension stiffness.

The modelling of the axle guidance is described in detail below. In short, the lateral model is a unilateral dead band spring model, and the longitudinal model is Newton's impact law with a coefficient of restitution.

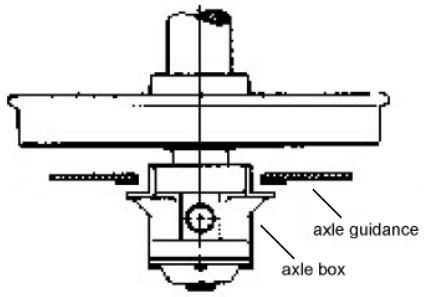

Figure 2.71: Axle guidance (top view).

Lateral A unilateral dead band spring model appropriately models the behaviour of the axle guidance in the lateral direction. This model is shown in Figure 2.72. The stiffness of the guidance is set to $k_{gl} = 1.5$ MN/m [24] and the clearance is $y_0 = 20$ mm. The mathematical formulation is presented in equation (2.39) and (2.40). The model is made state dependent due to its nonsmooth behaviour and the corresponding state machine is a simplified case of the state machine presented for the dead band spring model shown in Figure 2.57.

$$F_{gl}^{\text{right}}(y) = \begin{cases} 0 & \text{Idle} \\ -k_{gl}(y - y_0) & \text{SpringPos} \end{cases} \tag{2.39}$$

$$F_{gl}^{\text{left}}(y) = \begin{cases} 0 & \text{Idle} \\ -k_{gl}(y + y_0) & \text{SpringNeg} \end{cases} \tag{2.40}$$

Longitudinal Modelling the almost completely elastic impacts between the axle box and axle guidance in the longitudinal direction is done using Newton's

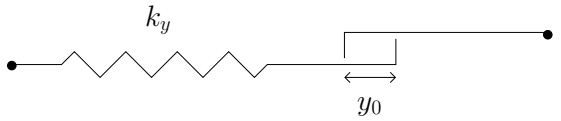

Figure 2.72: Model of axle guidance in the lateral direction.

impact law. It is noted that the unilateral dead band spring model is not appropriate here because it would require very high spring stiffnesses, which is unwanted from a numerical perspective.

The classical formulation of Newton's impact law is given in equation (2.41). The model instantaneously changes the direction of the motion along the x–coordinate. The velocity is multiplied by a coefficient of restitution, ϵ, to take into account the energy dissipation from the impact.

$$\dot{x}^+ = -\epsilon \dot{x}^- \tag{2.41}$$

This formulation of Newton's impact law can not be used directly for modelling the axle guidance because: 1) There might be multiple impacts (simultaneously). 2) The distance between the axle box and axle guidance depends on the motion of the wheelset as well as the carbody, and thus it is necessary to take into account several degrees of freedom.

An elegant formulation of the impact problem is achieved using the theory on unilateral contact problems from [60, 16]. If one or several of the longitudinal clearances are exceeded during simulation, the integration is stopped and a corresponding impact problem is solved in order to find the effect of the impact on the generalised coordinates. This impact problem is naturally formulated as a linear complementarity problem (LCP) being an optimisation problem with nonnegativity and orthogonality constraints. After solving the impact problem the integration is continued with a new initial condition that reflects the resulting effect of the impact. This formulation is more general in that it takes into account multiple impacts and it does not have the one dimensional restriction as the classical version. The basic effect of the impact is that the velocity in the normal direction at the contact point is reversed (multiplied by coefficient of restitution). In Appendix B.3, the strategy is illustrated for a 3 DOF system being slightly simpler than the axle guidance situation.

The contact problem considered here is illustrated in Figure 2.73. The two rods modelling the axle boxes can hit the axle guidance at one or several of the eight contact points. The DOF in the axle guidance model are

$$\mathbf{q} = [D_{xfw}, D_{\psi fw}, D_{xrw}, D_{\psi rw}, D_{\theta cb}, D_{\psi cb}]^T$$

and the contact points are defined by the following set

$$I_G = \{C1, C2, C3, C4, C5, C6, C7, C8\}$$

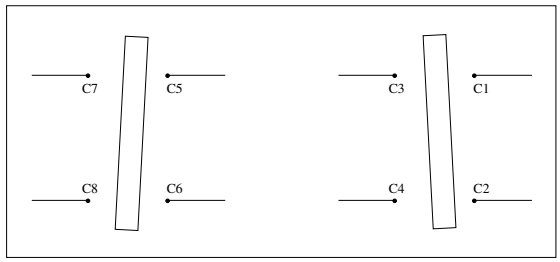

Figure 2.73: Contact points for the model of the axle guidance in the longitudinal direction.

Let $g_{Ni} \geq 0$ denote the distance between the contact point Ci to the axle box. If this distance vanish at the i'th contact point then an impact will occur. The following unilateral constraint functions are found by using the results from equation (2.26)

$$\begin{aligned}
g_{N1}(t,\mathbf{q}) &= -(R_1(\mathbf{q}) + \zeta(t)) + x_0 \\
g_{N2}(t,\mathbf{q}) &= -(R_2(\mathbf{q}) + \zeta(t)) + x_0 \\
g_{N3}(t,\mathbf{q}) &= R_3(\mathbf{q}) + \zeta(t) + x_0 \\
g_{N4}(t,\mathbf{q}) &= R_4(\mathbf{q}) + \zeta(t) + x_0 \\
g_{N5}(t,\mathbf{q}) &= -(R_5(\mathbf{q}) + \zeta(t)) + x_0 \\
g_{N6}(t,\mathbf{q}) &= -(R_6(\mathbf{q}) + \zeta(t)) + x_0 \\
g_{N7}(t,\mathbf{q}) &= R_7(\mathbf{q}) + \zeta(t) + x_0 \\
g_{N8}(t,\mathbf{q}) &= R_8(\mathbf{q}) + \zeta(t) + x_0
\end{aligned}$$

where

$$R_i = \begin{cases} D_{xfw} - y_{Pw}D_{\psi fw} + y_{Pcb}D_{\psi cb} - z_{Pcb}D_{\theta cb} & i = 1,2,3,4 \\ D_{xrw} - y_{Pw}D_{\psi rw} + y_{Pcb}D_{\psi cb} - z_{Pcb}D_{\theta cb} & i = 5,6,7,8 \end{cases}$$

and

$$\zeta(t) = -\bar{z}_{cb}\theta_{Ccb} + \bar{y}_{cb}\beta_{Ccb}$$

The quantity x_0 denotes the clearance between the axle box and axle guidance. It is reminded that the suspension attachment point on the wheelset is defined by the vector $[x_{Pw}, y_{Pw}, z_{Pw}]^T$, and that $[x_{Pcb}, y_{Pcb}, z_{Pcb}]^T$ is the corresponding vector for the carbody. The set of active constraint functions is

$$I_S = \{i \in I_G | g_{Ni} = 0; \quad \dot{g}_{Ni} \leq 0\}$$

The equations of motion can be written as

$$\mathbf{M}\ddot{\mathbf{q}} - \mathbf{h} - \sum_{i \in I_S} (\mathbf{w}_N \lambda_N)_i = 0$$

where $(\mathbf{w}_N \lambda_N)_i$ is the projection of the contact force at the i'th active contact point into the space of generalised coordinates. The vector $\mathbf{h}$ represents the sum

of the external forces. The relative velocity in the normal direction for the i'th contact is

$$\dot{g}_{Ni} = \frac{\mathrm{d}}{\mathrm{d}t}(g_{Ni}(t,\mathbf{q})) = \mathbf{w}_{Ni}^T\dot{\mathbf{q}} + \dot{\zeta}$$

where $\mathbf{w}_{Ni}$ is the generalised normal force direction for the i'th contact defined by

$$\mathbf{w}_{Ni} = \frac{\partial g_{Ni}}{\partial \mathbf{q}} = \left[\frac{\partial g_{Ni}}{\partial D_{xfw}}, \frac{\partial g_{Ni}}{\partial D_{\psi fw}}, \frac{\partial g_{Ni}}{\partial D_{xrw}}, \frac{\partial g_{Ni}}{\partial D_{\psi rw}}, \frac{\partial g_{Ni}}{\partial D_{\theta cb}}, \frac{\partial g_{Ni}}{\partial D_{\psi cb}}\right]^T$$

$$\begin{aligned}
\mathbf{w}_{N1} &= [-1, y_{C1fw}, 0, 0, z_{C1cb}, -y_{C1cb}]^T \\
\mathbf{w}_{N2} &= [-1, y_{C2fw}, 0, 0, z_{C2cb}, -y_{C2cb}]^T \\
\mathbf{w}_{N3} &= [1, -y_{C3fw}, 0, 0, -z_{C3cb}, y_{C3cb}]^T \\
\mathbf{w}_{N4} &= [1, -y_{C4fw}, 0, 0, -z_{C4cb}, y_{C4cb}]^T \\
\mathbf{w}_{N5} &= [0, 0, -1, y_{C5rw}, z_{C5cb}, -y_{C5cb}]^T \\
\mathbf{w}_{N6} &= [0, 0, -1, y_{C6rw}, z_{C6cb}, -y_{C6cb}]^T \\
\mathbf{w}_{N7} &= [0, 0, 1, -y_{C7rw}, -z_{C7cb}, y_{C7cb}]^T \\
\mathbf{w}_{N8} &= [0, 0, 1, -y_{C8rw}, -z_{C8cb}, y_{C8cb}]^T
\end{aligned}$$

In matrix–vector notation the equations of motion and the constraint functions are written as

$$\mathbf{M}\ddot{\mathbf{q}} - \mathbf{h} - \mathbf{W}_N\boldsymbol{\lambda}_N = \mathbf{0} \quad , \quad \dot{\mathbf{g}}_N = \mathbf{W}_N^T\dot{\mathbf{q}} + \dot{\boldsymbol{\zeta}}$$

For each member in I_S the associated vector $\mathbf{w}_{Ni}$ is gathered into a matrix $\mathbf{W}_N$, i.e. if $C1$ and $C3$ are the only active contact points then $\mathbf{W}_N = [\mathbf{w}_{N1}, \mathbf{w}_{N3}]$. Denote the impact time by t_A and the detachment time by t_E. Assuming that the duration of the impact is very short, one can rewrite the equations of motion on the impulse level

$$\lim_{t_E \to t_A} \int_{t_A}^{t_E} (\mathbf{M}\ddot{\mathbf{q}} - \mathbf{h} - \mathbf{W}_N\boldsymbol{\lambda}_N)\,\mathrm{d}t = \mathbf{M}(\dot{\mathbf{q}}_E - \dot{\mathbf{q}}_A) - \mathbf{W}_N\boldsymbol{\Lambda}_N = \mathbf{0}$$

where

$$\boldsymbol{\Lambda}_N = \lim_{t_E \to t_A} \int_{t_A}^{t_E} \boldsymbol{\lambda}_N\,\mathrm{d}t$$

The relative velocity in the normal direction at t_A and t_E is

$$\dot{\mathbf{g}}_{NA} = \mathbf{W}_N^T\dot{\mathbf{q}}_A + \dot{\boldsymbol{\zeta}} \quad , \quad \dot{\mathbf{g}}_{NE} = \mathbf{W}_N^T\dot{\mathbf{q}}_E + \dot{\boldsymbol{\zeta}}$$

Subtracting these two equations yields

$$\dot{\mathbf{g}}_{NE} - \dot{\mathbf{g}}_{NA} = \mathbf{W}_N^T(\dot{\mathbf{q}}_E - \dot{\mathbf{q}}_A) \tag{2.42}$$

Combining this information with the impulse formulation of the equations of motion yields

$$\dot{\mathbf{g}}_{NE} - \dot{\mathbf{g}}_{NA} = \mathbf{W}_N^T \mathbf{M}^{-1} \mathbf{W}_N \boldsymbol{\Lambda}_N \tag{2.43}$$

Newton's impact law can be expressed by the corner law in Figure 2.74, see [16], [60]. This means that

$$\dot{\mathbf{g}}_{NE} + \boldsymbol{\epsilon}_N \dot{\mathbf{g}}_{NA} \geq \mathbf{0} \quad , \quad \boldsymbol{\Lambda}_N \geq \mathbf{0} \quad , \quad (\dot{\mathbf{g}}_{NE} + \boldsymbol{\epsilon}_N \dot{\mathbf{g}}_{NA})^T \boldsymbol{\Lambda}_N = 0$$

where $\boldsymbol{\epsilon}_N = \text{diag}\{\epsilon_{Ni}\}$ contains the coefficients of restitution. A LCP can now be formulated by adding $\boldsymbol{\epsilon}_N \dot{\mathbf{g}}_{NA}$ to equation (2.43)

$$\underbrace{\dot{\mathbf{g}}_{NE} + \boldsymbol{\epsilon}_N \dot{\mathbf{g}}_{NA}}_{\boldsymbol{\xi}} = \underbrace{\mathbf{W}_N^T \mathbf{M}^{-1} \mathbf{W}_N}_{\mathbf{A}} \boldsymbol{\Lambda}_N + \underbrace{(\mathbf{I} + \boldsymbol{\epsilon}_N) \dot{\mathbf{g}}_{NA}}_{\mathbf{b}}$$

The matrix $\mathbf{I}$ is the identity matrix. In simplified notation the LCP problem is formulated as

$$\boldsymbol{\xi} = \mathbf{A}\boldsymbol{\Lambda}_N + \mathbf{b} \quad , \quad \mathbf{0} \leq \boldsymbol{\xi} \perp \boldsymbol{\Lambda}_N \geq \mathbf{0}$$

See Appendix D for a description on how to solve the LCP. The LCP is solved for $\boldsymbol{\xi}$ and $\boldsymbol{\Lambda}_N$. After solving the LCP the simulation is continued with an initial condition that is adjusted according to the velocity vector expressed in equation (2.44), which is deduced by combining equation (2.42) and (2.43).

$$\dot{\mathbf{q}}_E = \dot{\mathbf{q}}_A + \mathbf{M}^{-1} \mathbf{W}_N \boldsymbol{\Lambda}_N \tag{2.44}$$

The impact model presented above introduces a discontinuity into the system. The time instant of the impact is located during simulation and the state machine of the model is shown in Figure 2.75.

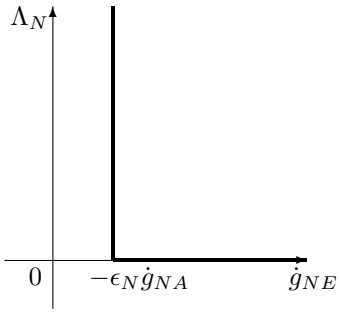

Figure 2.74: Newton's impact law.

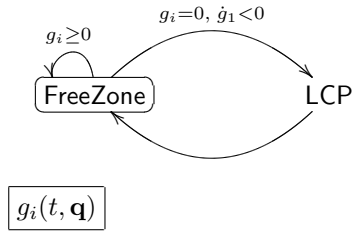

Figure 2.75: State machine.

2.4 Two–axle freight wagon model

The model used for simulating two–axle freight wagons can now be formulated. In Table 2.6 the DOF are shown. The number of DOF is 17.

DOF	Front wheelset	Rear wheelset	Carbody
Longitudinal	×	×	–
Lateral	×	×	×
Vertical	×	×	×
Roll	×	×	×
Pitch	–	–	×
Yaw	×	×	×
Spin pert.	×	×	–

Table 2.6: Degrees of freedom.

The model is essentially formulated as a system of first order ordinary differential equations. The equations of motion (see section 2.1.6) constitute of several second order differential equations. A second order equation is transformed into two first order equations by the transformation

$$\ddot{x} = f(x, \dot{x}) \quad \rightarrow \quad \begin{array}{l} x_1 \equiv x \\ x_2 \equiv \dot{x} \end{array} \quad \rightarrow \quad \left\{ \begin{array}{l} \dot{x}_1 = x_2 \\ \dot{x}_2 = f(x_1, x_2) \end{array} \right.$$

The resulting model is the 68 ODEs shown in equation (2.45).

$$\dot{\mathbf{y}} = \mathbf{f}(t, \mathbf{y}) \qquad \mathbf{y} \in \mathbb{R}^{68} \quad \mathbf{f} \in \mathbb{R}^{68} \quad t \geq 0 \tag{2.45}$$

where

$$\begin{aligned}
\mathbf{y}_{1\rightarrow 5} &= [D_{xfw}, D_{yfw}, D_{zfw}, D_{\phi fw}, D_{\psi fw}]^T \\
\mathbf{y}_{6\rightarrow 10} &= [D_{xrw}, D_{yrw}, D_{zrw}, D_{\phi rw}, D_{\psi rw}]^T \\
\mathbf{y}_{11\rightarrow 15} &= [D_{ycb}, D_{zcb}, D_{\phi cb}, D_{\theta cb}, D_{\psi rw}]^T \\
\mathbf{y}_{16\rightarrow 21} &= [\dot{D}_{xfw}, \dot{D}_{yfw}, \dot{D}_{zfw}, \dot{D}_{\phi fw}, \dot{D}_{\psi fw}, D_{\beta fw}]^T \\
\mathbf{y}_{22\rightarrow 27} &= [\dot{D}_{xrw}, \dot{D}_{yrw}, \dot{D}_{zrw}, \dot{D}_{\phi rw}, \dot{D}_{\psi rw}, D_{\beta rw}]^T \\
\mathbf{y}_{28\rightarrow 32} &= [\dot{D}_{ycb}, \dot{D}_{zcb}, \dot{D}_{\phi cb}, \dot{D}_{\theta cb}, \dot{D}_{\psi cb}]^T \\
\mathbf{y}_{33\rightarrow 40} &= [T_{1flx}, T_{2flx}, T_{3flx}, T_{4flx}, T_{1fly}, T_{2fly}, T_{3fly}, T_{4fly}]^T \\
\mathbf{y}_{41\rightarrow 48} &= [T_{1frx}, T_{2frx}, T_{3frx}, T_{4frx}, T_{1fry}, T_{2fry}, T_{3fry}, T_{4fry}]^T \\
\mathbf{y}_{49\rightarrow 56} &= [T_{1rlx}, T_{2rlx}, T_{3rlx}, T_{4rlx}, T_{1rly}, T_{2rly}, T_{3rly}, T_{4rly}]^T \\
\mathbf{y}_{57\rightarrow 64} &= [T_{1rrx}, T_{2rrx}, T_{3rrx}, T_{4rrx}, T_{1rry}, T_{2rry}, T_{3rry}, T_{4rry}]^T \\
\mathbf{y}_{65\rightarrow 68} &= [F_{flz}, F_{frz}, F_{rlz}, F_{rrz}]^T
\end{aligned}$$

$$\mathbf{f}_{1\to 15} = \begin{bmatrix} y_{16} \\ y_{17} \\ y_{18} \\ y_{19} \\ y_{20} \\ \hline y_{22} \\ y_{23} \\ y_{24} \\ y_{25} \\ y_{26} \\ \hline y_{28} \\ y_{29} \\ y_{30} \\ y_{31} \\ y_{32} \end{bmatrix} \qquad \mathbf{f}_{16\to 32} = \begin{bmatrix} -\Gamma + F_{xfw}/m_{fw} \\ \Gamma\beta_{Cfw} + F_{yfw}/m_{fw} \\ -\Gamma\theta_{Cfw} + F_{zfw}/m_{fw} \\ (\dot{D}_{\psi fw} I_{yyfw} V/r_0 + M_{xfw})/I_{xxfw} \\ (-\dot{D}_{\phi fw} I_{yyfw} V/r_0 + M_{zfw})/I_{zzfw} \\ M_{yfw}/I_{yyfw} \\ \hline -\Gamma + F_{xrw}/m_{rw} \\ \Gamma\beta_{Crw} + F_{yrw}/m_{rw} \\ -\Gamma\theta_{Crw} + F_{zrw}/m_{rw} \\ (\dot{D}_{\psi rw} I_{yyrw} V/r_0 + M_{xrw})/I_{xxrw} \\ (-\dot{D}_{\phi rw} I_{yyrw} V/r_0 + M_{zrw})/I_{zzrw} \\ M_{yrw}/I_{yyrw} \\ \hline \Gamma\beta_{Ccb} + F_{ycb}/m_{cb} \\ -\Gamma\theta_{Ccb} + F_{zcb}/m_{cb} \\ M_{xcb}/I_{xxcb} \\ M_{ycb}/I_{yycb} \\ M_{zcb}/I_{zzcb} \end{bmatrix}$$

$$\mathbf{f}_{33\to 40} \begin{bmatrix} \dot{T}_{1flx} \\ \dot{T}_{2flx} \\ \dot{T}_{3flx} \\ \dot{T}_{4flx} \\ \dot{T}_{1fly} \\ \dot{T}_{2fly} \\ \dot{T}_{3fly} \\ \dot{T}_{4fly} \end{bmatrix} \quad \mathbf{f}_{41\to 48} \begin{bmatrix} \dot{T}_{1frx} \\ \dot{T}_{2frx} \\ \dot{T}_{3frx} \\ \dot{T}_{4frx} \\ \dot{T}_{1fry} \\ \dot{T}_{2fry} \\ \dot{T}_{3fry} \\ \dot{T}_{4fry} \end{bmatrix} \quad \mathbf{f}_{49\to 56} \begin{bmatrix} \dot{T}_{1rlx} \\ \dot{T}_{2rlx} \\ \dot{T}_{3rlx} \\ \dot{T}_{4rlx} \\ \dot{T}_{1rly} \\ \dot{T}_{2rly} \\ \dot{T}_{3rly} \\ \dot{T}_{4rly} \end{bmatrix} \quad \mathbf{f}_{57\to 64} \begin{bmatrix} \dot{T}_{1rrx} \\ \dot{T}_{2rrx} \\ \dot{T}_{3rrx} \\ \dot{T}_{4rrx} \\ \dot{T}_{1rry} \\ \dot{T}_{2rry} \\ \dot{T}_{3rry} \\ \dot{T}_{4rry} \end{bmatrix} \quad \mathbf{f}_{65\to 68} \begin{bmatrix} \dot{F}_{flz} \\ \dot{F}_{frz} \\ \dot{F}_{rlz} \\ \dot{F}_{rrz} \end{bmatrix}$$

Equation 1 to 32 are the equations of motion, equation 33 to 64 are related to the friction forces in the UIC links and equation 65 to 68 are the normalised forces in the leaf springs. Note that the equations related to the spin of the wheelset, i.e. equation 21 and 27, were already expressed as first order differential equations in section 2.1.6. The external forces and torques on the two wheelsets are $(i = fw, rw)$

$$\begin{bmatrix} F_{xi} \\ F_{yi} \\ F_{zi} \end{bmatrix} = \mathbf{A}_{TiO}\mathbf{F}_{gi} + \mathbf{A}_{TiTcb}\left(\mathbf{F}_{sli} + \mathbf{F}_{sri}\right) + \mathbf{A}_{Tibi}\left[\sum_{j=1}^{n_c} \mathbf{A}_{bicj}\mathbf{F}_{cj}\right] \tag{2.46}$$

$$\begin{bmatrix} M_{xi} \\ M_{yi} \\ M_{zi} \end{bmatrix} = \tilde{\mathbf{R}}_{sl}\ \mathbf{A}_{biTcb}\mathbf{F}_{sli} + \tilde{\mathbf{R}}_{sr}\ \mathbf{A}_{biTcb}\mathbf{F}_{sri} + \sum_{j=1}^{n_c} \tilde{\mathbf{R}}_{cj}\ \mathbf{A}_{bicj}\mathbf{F}_{cj} \tag{2.47}$$

Likewise, the external forces and torques on the carbody are $(i = cb)$

$$\begin{bmatrix} F_{xi} \\ F_{yi} \\ F_{zi} \end{bmatrix} = \mathbf{A}_{TiO}\mathbf{F}_{gi} + \mathbf{F}_{sfli} + \mathbf{F}_{sfri} + \mathbf{F}_{srli} + \mathbf{F}_{srri} \tag{2.48}$$

$$\begin{bmatrix} M_{xi} \\ M_{yi} \\ M_{zi} \end{bmatrix} = \tilde{\mathbf{R}}_{sfl}\ \mathbf{A}_{biTi}\mathbf{F}_{sfli} + \tilde{\mathbf{R}}_{sfr}\ \mathbf{A}_{biTi}\mathbf{F}_{sfri} + \tilde{\mathbf{R}}_{srl}\ \mathbf{A}_{biTi}\mathbf{F}_{srli} + \tilde{\mathbf{R}}_{srr}\ \mathbf{A}_{biTi}\mathbf{F}_{srri} \tag{2.49}$$

Here, $\tilde{\mathbf{R}}$ is the linear operator $\mathbf{R}\times$.

The gravitational forces are expressed in the inertial frame

$$\mathbf{F}_{gi} = \begin{bmatrix} 0 \\ 0 \\ -m_i g \end{bmatrix}$$

The suspension forces from the UIC suspension are functions of the suspension deformation and its time derivative from equation (2.26) and (2.27), respectively. The longitudinal suspension force $F_{\mathrm{UIC,x}}$ is found through equation (2.33). It is a function of the suspension deformation Δr_x and the forces from the elastic dry friction elements T_{1x} to T_{4x}. The lateral suspension force $F_{\mathrm{UIC,y}}$ is given by equation (2.34) (cylindrical case) or by equation (2.38) (measured case). The lateral guidance model in equation (2.39) and (2.40) is also incorporated into $F_{\mathrm{UIC,y}}$. The lateral suspension force is a function of the suspension deformation Δr_y and the forces from the elastic dry friction elements T_{1y} to T_{4y}. The vertical suspension forces are found by scaling the normalised values given in y_{65}, y_{66}, y_{67}, y_{68} with the static load on the leaf spring, $m_{cb}g/4$. The suspension forces are expressed in the track system of the carbody.

$$\mathbf{F}_{sflcb} = \begin{bmatrix} -F_{\mathrm{UIC,x}}(\Delta r_{flx}, y_{33}, y_{34}, y_{35}, y_{36}) \\ -F_{\mathrm{UIC,y}}(\Delta r_{fly}, y_{37}, y_{38}, y_{39}, y_{40}) \\ m_{cb}gy_{65}/4 \end{bmatrix} \quad , \quad \mathbf{F}_{slfw} = -\mathbf{F}_{sflcb}$$

$$\mathbf{F}_{sfrcb} = \begin{bmatrix} -F_{\mathrm{UIC,x}}(\Delta r_{frx}, y_{41}, y_{42}, y_{43}, y_{44}) \\ -F_{\mathrm{UIC,y}}(\Delta r_{fry}, y_{45}, y_{46}, y_{47}, y_{48}) \\ m_{cb}gy_{66}/4 \end{bmatrix} \quad , \quad \mathbf{F}_{srfw} = -\mathbf{F}_{sfrcb}$$

$$\mathbf{F}_{srlcb} = \begin{bmatrix} -F_{\mathrm{UIC,x}}(\Delta r_{rlx}, y_{49}, y_{50}, y_{51}, y_{52}) \\ -F_{\mathrm{UIC,y}}(\Delta r_{rly}, y_{53}, y_{54}, y_{55}, y_{56}) \\ m_{cb}gy_{67}/4 \end{bmatrix} \quad , \quad \mathbf{F}_{slrw} = -\mathbf{F}_{srlcb}$$

$$\mathbf{F}_{srrcb} = \begin{bmatrix} -F_{\mathrm{UIC,x}}(\Delta r_{rrx}, y_{57}, y_{58}, y_{59}, y_{60}) \\ -F_{\mathrm{UIC,y}}(\Delta r_{rry}, y_{61}, y_{62}, y_{63}, y_{64}) \\ m_{cb}gy_{68}/4 \end{bmatrix} \quad , \quad \mathbf{F}_{srrw} = -\mathbf{F}_{srrcb}$$

The contact forces are computed in the contact coordinate system.

$$\mathbf{F}_{cj} = \begin{bmatrix} T_{xj} \\ T_{yj} \\ N_j \end{bmatrix}$$

The position of the j'th wheel–rail contact point is defined by $\mathbf{R}_{cj}$. This vector is found using the contact table.

The suspension attachment points for the bodies are defined (and fixed) relative to the body frames. For the wheelsets these points are defined by

$$\mathbf{R}_{sl} = \begin{bmatrix} 0 \\ 1 \\ 0 \end{bmatrix} \qquad \mathbf{R}_{sr} = \begin{bmatrix} 0 \\ -1 \\ 0 \end{bmatrix}$$

The suspension attachment points for the carbody are ($i = cb$)

$$\mathbf{R}_{sfl} = \begin{bmatrix} d_{wb} \\ 1 - \bar{y}_{cb} \\ -(\bar{z}_{cb} - r_0) \end{bmatrix} \quad \mathbf{R}_{sfr} = \begin{bmatrix} d_{wb} \\ -1 + \bar{y}_{cb} \\ -(\bar{z}_{cb} - r_0) \end{bmatrix}$$
$$\mathbf{R}_{srl} = \begin{bmatrix} -d_{wb} \\ 1 - \bar{y}_{cb} \\ -(\bar{z}_{cb} - r_0) \end{bmatrix} \quad \mathbf{R}_{srr} = \begin{bmatrix} -d_{wb} \\ -1 + \bar{y}_{cb} \\ -(\bar{z}_{cb} - r_0) \end{bmatrix}$$

where d_{wb} is the half wheelbase.

Wagons Three different wagons have been implemented and used for the analysis. The wagons are shown in Figure 2.76 and their corresponding wagon data are given in Table 2.7. The Hbbills 311 is a covered wagon from Germany with a long wheelbase. The vertical suspension is provided by two–stage parabolic leaf springs. The G69 is an older covered standard wagon from France with short wheel base and trapezoidal leaf springs. The Swedish Kbps is an open–sided wagon with trapezoidal leaf springs. The Kbps wagon data is taken from Stichel's work [80].

The Hbbills 311 wagon uses the modern wheelset `BA004` with the `BA381` bearings. The inertia properties for this wheelset are provided by RAFIL (Germany) [68] and shown in Table 2.8. The inertia from the wheelset bearing and the UIC suspension is incorporated into the wheelset mass in the simulations. The UIC suspension with a parabolic leaf spring weighs 147.6 kg (DSB Produktion, Denmark). Hence, the inertia properties of the simulated wheelset become

$$\begin{aligned} m/\text{kg} &= 1032.0 + 2 \cdot 81.5 + 2 \cdot 147.6 \approx 1490.0 \\ I_{xx}/\text{kg m}^2 &= 529.8 + 2 \cdot 81.5 \cdot 1^2 + 2 \cdot 147.6 \cdot 1^2 \approx 988.0 \\ I_{yy}/\text{kg m}^2 &\approx 90.0 \\ I_{zz}/\text{kg m}^2 &\approx 988.0 \end{aligned}$$

Hbbills 311

G69

Kbps

Figure 2.76: Wagon pictures.

	Unit	Hbbills 311	G69	Kbps
m_w	[kg]	1490.0	1570.0	1420.0
I_{xxw}	[kg m^2]	988.0	810.0	1040.0
I_{yyw}	[kg m^2]	90.0	112.0	154.0
I_{zzw}	[kg m^2]	988.0	810.0	1040.0
m_{cb}	[kg]	15176.0	8860.0	8610.0
I_{xxcb}	[kg m^2]	32675.0	16600.0	25000.0
I_{yycb}	[kg m^2]	422084.0	86000.0	121400.0
I_{zzcb}	[kg m^2]	413250.0	88000.0	127700.0
r_0	[m]	0.46	0.43	0.46
$\bar{y}_w$	[m]	0.0	0.0	0.0
$\bar{z}_w$	[m]	0.46	0.43	0.46
$\bar{y}_{cb}$	[m]	0.0	0.0	0.0
$\bar{z}_{cb}$	[m]	1.57	1.58	1.20
Clearance, x_0	[m]	0.0225	0.02	0.02
Clearance, y_{01}	[m]	0.01	0.01	0.01
Clearance, y_{02}	[m]	0.02	0.02	0.02
Wheelbase	[m]	10.0	5.7	8.0
COM height	[m]	1.57	1.58	1.20

Table 2.7: Wagons – inertia and details. Empty wagons.

$m_{\texttt{BA381}}$	81.5 kg
$m_{\texttt{BA004}}$	1032.0 kg
$I_{xx,\texttt{BA004}}$	529.8 kg m^2
$I_{yy,\texttt{BA004}}$	89.9 kg m^2
$I_{zz,\texttt{BA004}}$	529.8 kg m^2
r_0	460 mm
Max. axle load	23.5 t

Table 2.8: Wheelset data.

Chapter 3

Numerical integration

3.1 Integration method

A key aspect in simulating the freight wagon is the integration of the differential equation system constituting the model (see equation (2.45)). As a consequence of the system complexity (nonlinear/nonsmooth, tabulated parameters for the wheel–rail contact, system size) it is necessary to find approximate solutions by numerical integration. Fortunately, the field of numerical analysis of differential equations existed since before the prevalence of computers and the available methods today are extensive. A thorough treatment of many popular methods can be found in [22, 23, 30, 4].

The model of the freight wagon is integrated with the implicit Runge–Kutta scheme with error control from [89, 106]. To be more specific the initial value problem (IVP) in equation (3.1) is numerically approximated using the scheme in equation (3.2).

$$\dot{\mathbf{y}} = \mathbf{f}(t, \mathbf{y}) \quad , \quad \mathbf{y}(t_0) = \mathbf{y}_0 \quad , \quad \mathbf{f} : \mathbb{R} \times \mathbb{R}^m \to \mathbb{R}^m \tag{3.1}$$

$$\mathbf{y}_{n+1} = \mathbf{y}_n + h \sum_{i=1}^{4} b_i \mathbf{k}_i \tag{3.2}$$

$$\mathbf{k}_i = \mathbf{f}\left(t_n + c_i h, \mathbf{y}_n + h \sum_{j=1}^{i} a_{ij} \mathbf{k}_j \right) \tag{3.3}$$

0	0	0	0	0
5/6	5/12	5/12	0	0
10/21	95/588	−5/49	5/12	0
1	59/600	−31/75	539/600	5/12
$\mathbf{y}_{n+1}$	59/600	−31/75	539/600	5/12
$\mathbf{e}_{n+1}$	−37/600	−37/75	1813/6600	37/132

$=$

$\mathbf{c}$	$\mathbf{A}$
	$\mathbf{b}^T$
	$\mathbf{d}^T$

Table 3.1: Butcher tableau.

The local stepsize is denoted by h and the integration coefficients are shown by the Butcher tableau in Table 3.1. The method belongs to the ESDIRK[1] family of Runge–Kutta methods. Any usable numerical method should satisfy the fundamental requirement that it is convergent saying that the numerical solution tends to the true solution as the grid is refined ($h \to 0$). The order of the method tells how fast the error incurred in the numerical integration from t_n to $t_n + h$ decreases to zero with the stepsize h. A method has order p if the difference between the Taylor series for the exact solution through the point $\mathbf{y}_n$ evaluated at $\mathbf{y}(t_n + h)$ and the numerical solution $\mathbf{y}_{n+1}$ is $\mathcal{O}(h^{p+1})$. The ESDIRK method used here is of order $p = 3$. Globally the behaviour of the method is $\mathcal{O}(h^p)$.

Note that only the first stage derivative $\mathbf{k}_1 = \mathbf{f}(t_n, \mathbf{y}_n)$ is explicit. The remaining $\mathbf{k}_2, \mathbf{k}_3, \mathbf{k}_4$ are implicitly defined through equation (3.3). Newton–Raphson's iterative method is used to find the implicit $\mathbf{k}_i$, that is

$$\text{loop} \left\{ \begin{array}{rcl} \boldsymbol{\nabla}\mathbf{F}(\mathbf{k}_i^{(k)})\Delta\mathbf{k}_i = & -\mathbf{F}(\mathbf{k}_i^{(k)}) \\ \mathbf{k}_i^{(k+1)} = & \mathbf{k}_i^{(k)} + \Delta\mathbf{k}_i \end{array} \right. \quad , \quad i = 2, 3, 4$$

where

$$\begin{aligned} \mathbf{F}(\mathbf{k}_i) &= \mathbf{k}_i - \mathbf{f}\left(t_n + c_i h, \mathbf{y}_n + h\sum_{j=1}^{i} a_{ij}\mathbf{k}_j\right) \\ \boldsymbol{\nabla}\mathbf{F}(\mathbf{k}_i) &= \mathbf{I} - h a_{ii}\boldsymbol{\nabla}_{\mathbf{y}}\mathbf{f}\left(t_n + c_i h, \mathbf{y}_n + h\sum_{j=1}^{i} a_{ij}\mathbf{k}_j\right) \end{aligned}$$

and $\boldsymbol{\nabla}_{\mathbf{y}}\mathbf{f} \equiv \partial\mathbf{f}/\partial\mathbf{y}$. The identical diagonal elements in ESDIRK methods can be exploited to achieve an efficient solver because a single factorisation of the matrix $\boldsymbol{\nabla}\mathbf{F}(\mathbf{k}_i)$ is often sufficient in each integration step [23].

The stepsize h is adaptively controlled using the error estimate in equation (3.4), see [89, 22] for further details. This local error estimate is obtained

[1] Explicit singly diagonally implicit Runge–Kutta

by comparing the numerical solution with an embedded method of order 4.

$$\mathbf{e}_{n+1} = h \sum_{i=1}^{4} d_i \mathbf{k}_i \tag{3.4}$$

Systems characterised by solutions having modes at considerably different time scales will cause problems for the numerical stability for some methods. These systems are called stiff systems. Therefore, in order to properly integrate stiff systems it is necessary to use an integration scheme with certain stability properties. The system modelling the freight wagon is stiff because the high contact stiffness between the wheel and rail generate modes on a different time scale compared to modes induced by the suspension system. The stability of numerical methods is investigated through the scalar linear test equation [23, 30]

$$y' = \lambda y \quad , \quad t \geq 0 \quad , \quad y(0) = 1 \tag{3.5}$$

The stability region $\mathcal{D}$ of a numerical method is defined by all numbers $h\lambda \in \mathbb{C}$ such that $\lim_{n\to\infty} y_n = 0$. To avoid numerical instabilities it is required that in the n'th step the eigenvalues of the Jacobi matrix $(\boldsymbol{\nabla}_{\mathbf{y}}\mathbf{f})$ should satisfy

$$h\lambda_{n,1}, h\lambda_{n,2}, \ldots, h\lambda_{n,d} \in \mathcal{D} \tag{3.6}$$

The well known Euler scheme is characterised by having a stability region being the interior of a complex disc with unit radius, centred at $z = -1$. For stiff systems the method is unsuitable because some eigenvalues will be very distant from the stability region, and in order to avoid numerical instability, it is necessary to force the stepsize down such that equation (3.6) is obeyed. In practice, it is only possible to reduce the stepsize until a certain level, and moreover small steps makes the method inefficient. The stability region regarding the ESDIRK method in equation (3.2) is found next. By a straight forward application of the integration scheme it is found that

$$y_{n+1} = y_n + h \sum_{i=1}^{4} b_i k_i \quad , \quad k_i = \lambda \left(y_n + h \sum_{j=1}^{i} a_{ij} k_j \right)$$

Letting

$$\mathbf{k} = [k_1, k_2, k_3, k_4]^T \quad , \quad \mathbf{b} = [b_1, b_2, b_3, b_4]^T \quad , \quad \mathbf{1} = [1, 1, 1, 1]^T$$

it is found that

$$y_{n+1} = y_n + h\mathbf{b}^T\mathbf{k} \quad , \quad \mathbf{k} = \lambda(y_n + h\mathbf{A}\mathbf{k})$$

Hence

$$y_{n+1} = R(h\lambda) y_n \quad , \quad R(z) = 1 + z\mathbf{b}^T(\mathbf{I} - z\mathbf{A})^{-1}\mathbf{1} \tag{3.7}$$

From this equation it is seen that $y_n = [R(h\lambda)]^n$, $n = 0, 1, \ldots$ and therefore the stability region is

$$\mathcal{D} = \{z \in \mathbb{C} : |R(z)| < 1\}$$

Inserting the coefficients from the Butcher tableau in Table 3.1 gives

$$R(z) = \frac{1 - \frac{1}{4}z - \frac{11}{48}z^2 - \frac{17}{1728}z^3}{\left(1 - \frac{5}{12}z\right)^3} \quad , \quad z \in \mathbb{C}$$

Figure 3.1 and 3.2 illustrates the stability region of the ESDIRK method. The fact that

$$\mathbb{C}^- = \{z \in \mathbb{C} : \mathrm{Re}(z) < 0\}$$

belongs to the stability region $\mathcal{D}$ provides a good stability property of the numerical scheme. The method is said to be A–stable. It basically means that the stability of the method does not require that the stepsize should be below a certain level, and hence the stepsize can be chosen on accuracy considerations only.

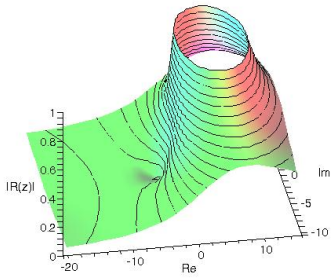

Figure 3.1: Illustrating the stability region, $|R(z)| < 1$.

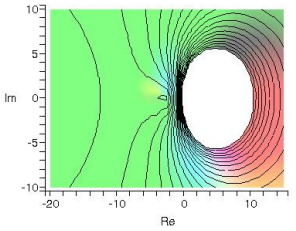

Figure 3.2: Top view. The white patch indicates the region where the method is not stable, i.e. $|R(z)| \geq 1$.

The construction of a so called continuous extension is useful for several purposes: generation of dense output, provide a good initial guess for the Newton–Raphson's method in determining the stage derivatives, and event location. The continuous extension is basically the polynomial $\mathbf{y}_c(t_n + \theta h)$ approximating the true solution between $\mathbf{y}_n$ and $\mathbf{y}_{n+1}$.

$$\mathbf{y}_c(t_n + \theta h) = \mathbf{y}_n + h \sum_{i=1}^{4} \bar{b}_i(\theta)\mathbf{k}_i \quad , \quad \theta \in [0; 1] \tag{3.8}$$

The coefficients $\bar{b}_i(\theta)$ are found through satisfying the 3. order conditions [23, 45]

$$\bar{\mathbf{b}}^T\mathbf{C}^{k-1}\mathbf{1} = \frac{\theta^k}{k} \qquad k = 1,2,3 \qquad , \qquad \bar{\mathbf{b}}^T\mathbf{AC1} = \frac{\theta^3}{6}$$

where $\mathbf{C} = \mathrm{diag}(c_1, c_2, c_3, c_4)$ and $\mathbf{1} = [1,1,1,1]^T$. These conditions can be written in matrix–vector notation as

$$\begin{bmatrix} 1 & 1 & 1 & 1 \\ 0 & c_2 & c_3 & 1 \\ 0 & c_2^2 & c_3^2 & 1 \\ 0 & \gamma c_2 & a_{32}c_2 + \gamma c_3 & b_2c_2 + b_3c_3 + \gamma \end{bmatrix} \begin{bmatrix} \bar{b}_1 \\ \bar{b}_2 \\ \bar{b}_3 \\ \bar{b}_4 \end{bmatrix} = \begin{bmatrix} \theta \\ \theta^2/2 \\ \theta^3/3 \\ \theta^3/6 \end{bmatrix} \tag{3.9}$$

The linear system in equation (3.9) is singular with one degree of freedom. By letting $\bar{b}_1 = b_1\theta$ the following coefficients have been found

$$\begin{aligned} \bar{b}_1(\theta) &= \frac{59}{600}\theta \\ \bar{b}_2(\theta) &= -\frac{541}{75}\theta + \frac{62}{5}\theta^2 - \frac{28}{5}\theta^3 \\ \bar{b}_3(\theta) &= \frac{26509}{6600}\theta - \frac{49}{10}\theta^2 + \frac{98}{55}\theta^3 \\ \bar{b}_4(\theta) &= \frac{541}{132}\theta - \frac{15}{2}\theta^2 + \frac{42}{11}\theta^3 \end{aligned}$$

It is seen that the continuous extension interpolates the numerical solution at both end points, i.e.

$$\bar{b}_i(0) = 0 \quad , \quad \bar{b}_i(1) = b_i \qquad , \quad i = 1,2,3,4 \tag{3.10}$$

An important remark is that the construction of the continuous extension is done efficiently because it is based on the same $\mathbf{k}_i$ that already are computed in the progress of the numerical solution. Hence, additional function calls of $\mathbf{f}$, typically being very expensive, are not necessary.

3.2 Event system

In the solution procedure for the freight wagon model yet another challenge appears: the function $\mathbf{f}$ in the IVP in equation (3.1) is nonsmooth. The nonsmoothness is due to the nature of the interacting forces, i.e. stick–slip transitions in the suspension model, impacts between the axle box and axle guidance, discontinuities in the contact parameters for the wheel–rail contact. Classical numerical methods are all based on the existence of the derivatives of $\mathbf{f}$. Generally speaking this nonsmoothness tends to have the following effects on the numerical method: 1) The numerical solution is simply inaccurate because the progress of the solution is based on non–existing derivatives of $\mathbf{f}$. This is a common situation for constant stepsize integration schemes. 2) The simulation time

is unacceptably high because the stepsize is forced down near the nonsmooth points in order to satisfy the error tolerance specified. This happens when integration schemes with variable stepsize and error control are applied but it is due to the lack of smoothness of the local error.

To avoid these numerical problems an *event system* is formulated. Each nonsmoothness of $\mathbf{f}$ defines a so called *event*. The solution to the IVP is found by a piecewise integration strategy where each smooth section is integrated separately. The isolated events are located during the simulation and treated independently. In the freight wagon model, a typical action for such an event is a state change in one of the suspension elements.

Central in the event system is locating of the nonsmooth instants during the simulation. These points can be expressed as a root finding problem of the *event functions* defining the switching boundaries between the different states of the model. The event location procedure is discussed next [77, 101, 13, 89]. Consider the time integration from $\mathbf{y}_n$ to $\mathbf{y}_{n+1}$, and let

$$g_i(t, \mathbf{y}) \qquad i = 1, 2, \ldots, N$$

be the complete set of event functions. If any of these event functions become active, i.e. has a root within the time step, then the continuous extension from equation (3.8) is constructed. The first occurred event is of interest because it defines the time instant when it is necessary to take action. The time t^* of this event is defined by

$$t^* = t_n + \theta^* h \qquad , \quad \theta^* = \min_{i \in I_G} \{\theta_i | g_i(t_n + \theta_i h, \mathbf{y}_c(t_n + \theta_i h)) = 0\} \tag{3.11}$$

where I_G is the set of active event functions. It is important that the continuous extension interpolates the numerical solution exactly at both end points, i.e. the property defined by equation (3.10), otherwise it might happen that an event is defined by $\theta^* \notin [0; 1]$. For instance, consider the integration from $\mathbf{y}_n$ to $\mathbf{y}_{n+1}$ and assume that the event function g_j is having $g_j(t_n, \mathbf{y}_n) < 0$ and $g_j(t_{n+1}, \mathbf{y}_{n+1}) > 0$, i.e. a root within the time step. Assume also that the numerical method is of order q and the event is located using a continuous extension of order $q + 1$. This means that $\mathbf{y}_{n+1} - \mathbf{y}_c(t_{n+1}) = \mathcal{O}(h^{q+1})$. If the root is sufficiently close to the right end point then it is possible that $g_j(t_{n+1}, \mathbf{y}_c(t_{n+1})) < 0$, or in other words the event has not happened yet. So, even though the continuous extension is locally more accurate it would cause the event system to be inconsistent.

The root of the nonlinear equation $g(t_n + \theta h, \mathbf{y}_c(t_n + \theta h)) = 0$ can be found with a few iterations of Newton–Raphson's method using the good initial guess in equation (3.12). This initial guess is derived directly from the linear interpolant between the two solution points surrounding the event.

$$\theta_0 = \frac{g(t_n, \mathbf{y}_n)}{g(t_n, \mathbf{y}_n) - g(t_{n+1}, \mathbf{y}_{n+1})} \tag{3.12}$$

The Newton–Raphson's method is shown below

$$\theta_{k+1} = \theta_k - G(\theta_k)/G'(\theta_k)$$

where

$$\begin{aligned} G(\theta) &\equiv g(t_n + \theta h, \mathbf{y}_c(t_n + \theta h)) \\ G'(\theta) &\equiv g_t h + g_{\mathbf{y}} \mathbf{y}'_c(t_n + \theta h) \end{aligned}$$

The derivative of the continuous extension w.r.t. θ is required for the Newton–Raphson's method. From the definition of the continuous extension (see equation (3.8)) the following is found

$$\mathbf{y}'_c(t_n + \theta h) = h \sum_{i=1}^{4} \bar{b}'_i(\theta) \mathbf{k}_i$$

The polynomial $\bar{b}'_i(\theta)$ is given by

$$\begin{aligned} \bar{b}_i(\theta) &= \bar{b}_{i,1}\theta + \bar{b}_{i,2}\theta^2 + \bar{b}_{i,3}\theta^3 \\ \bar{b}'_i(\theta) &= \bar{b}_{i,1} + 2\bar{b}_{i,2}\theta + 3\bar{b}_{i,3}\theta^2 \end{aligned}$$

The resulting event location algorithm is shown in Algorithm 2. Before simulation a list containing a reference to all submodels with nonsmooth properties is generated, see Table 3.2. If an event occurs in the i'th submodel it is located and put into an event queue. This queue always contains the first occurred event. If another event has the same value of θ (say with in a tolerance of 10^{-8}) it will be appended to the event queue. After running through the complete event list the necessary state changes of the submodels specified in the event queue are executed.

The overall integration procedure can now be illustrated by the flow diagram in Figure 3.3. Visualising the state changes for a specific simulation is helpful for understanding the event system, see Figure 3.4. The top figure gives the time history of the front wheelset, and the bottom figure indicates the state changes in some of the submodels. It is seen that the wagon starts near the centre of the track and eventually ends up in an oscillating motion. The legends and general interpretation of the bottom figure is described in the following:

DFE refers to an elastic *dry friction element* used in the modelling of the UIC links. Such an element has three different states: Stick (no peak), SlidePos (small peak), SlideNeg (high peak). An identifier such as **FLY** says that the element is positioned in the model of the *front left* suspension in the *lateral* direction. **DBS** is the *dead band spring* modelling the suspension bracket in the UIC links. The corresponding states are: Idle (no peak), SpringPos (small peak), SpringNeg (high peak). **WR** is a *wheel–rail contact module*. This element can have several states depending on the amount of discontinuities in the contact

$\theta_{\min} = 1.0$
event = **false**
for $i \in$ `EVTLIST` **do**
  call state machine of the i'th event for $\theta = 1$
  if i'th event is active **then**
    $\theta = g_i(t_n, \mathbf{y}_n)/(g_i(t_n, \mathbf{y}_n) - g_i(t_{n+1}, \mathbf{y}_{n+1}))$
    iter = 1
    repeat
      $\theta = \theta - g_i(t_n + \theta h, \mathbf{y}_c)/(g_{i,t}h + g_{i,\mathbf{y}}\mathbf{y}'_c)$
    until $|g_i(t_n + \theta h, \mathbf{y}_c)| <$ tol $\vee$ iter++ > maxiter
    if $\theta \in [0; 1]$ **then**
      event = **true**
      if $\theta < \theta_{\min}$ **then**
        clear `EVTQUEUE`
        insert i'th event into `EVTQUEUE`
        $\theta_{\min} = \theta$
      else if $\theta - \theta_{\min} < 10^{-8}$ **then**
        insert i'th event into `EVTQUEUE`
      end if
    end if
  end if
end for
for $i \in$ `EVTQUEUE` **do**
  call action command on the i'th event.
end for

Algorithm 2: Event location.

Index	Description
0	Dry friction element (FLX)
1	Dry friction element (FLX)
2	Dry friction element (FLX)
3	Dry friction element (FLX)
4	Dry friction element (FLY)
5	Dry friction element (FLY)
6	Dry friction element (FLY)
7	Dry friction element (FLY)
8	Dry friction element (FRX)
9	Dry friction element (FRX)
10	Dry friction element (FRX)
11	Dry friction element (FRX)
12	Dry friction element (FRY)
13	Dry friction element (FRY)
14	Dry friction element (FRY)
15	Dry friction element (FRY)
16	Dry friction element (RLX)
17	Dry friction element (RLX)
18	Dry friction element (RLX)
19	Dry friction element (RLX)
20	Dry friction element (RLY)
21	Dry friction element (RLY)
22	Dry friction element (RLY)
23	Dry friction element (RLY)
24	Dry friction element (RRX)
25	Dry friction element (RRX)
26	Dry friction element (RRX)
27	Dry friction element (RRX)
28	Dry friction element (RRY)
29	Dry friction element (RRY)
30	Dry friction element (RRY)
31	Dry friction element (RRY)

Index	Description
32	Suspension bracket (FLY)
33	Suspension bracket (FRY)
34	Suspension bracket (RLY)
35	Suspension bracket (RRY)
36	Axle guidance (FRY)
37	Axle guidance (RRY)
38	Axle guidance (FLY)
39	Axle guidance (RLY)
40	Leaf spring (FLZ)
41	Leaf spring (FRZ)
42	Leaf spring (RLZ)
43	Leaf spring (RRZ)
44	Track event (FW)
45	Track event (RW)
46	Track event (CB)
47	Axle guidance (FLX, C1)
48	Axle guidance (FRX, C2)
49	Axle guidance (FLX, C3)
50	Axle guidance (FRX, C4)
51	Axle guidance (RLX, C5)
52	Axle guidance (RRX, C6)
53	Axle guidance (RLX, C7)
54	Axle guidance (RRX, C8)
55	Wheel–rail (FL)
56	Wheel–rail (FR)
57	Wheel–rail (RL)
58	Wheel–rail (RR)

Table 3.2: Event list.

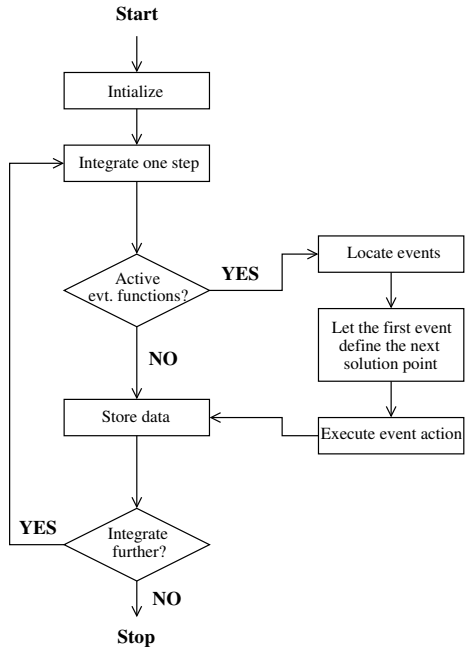

Figure 3.3: Flow diagram.

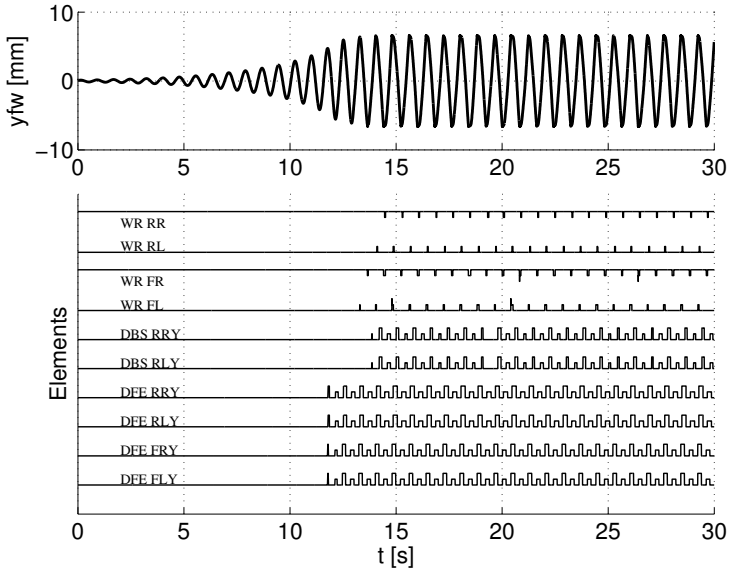

Figure 3.4: Event system illustration.

parameters for the specific wheel–rail profiles used. Typically, these discontinuities are found near the flange, and hence the diagram tells if the wheel is flanging. For the left wheels this causes one or several peaks upwards, and for the right wheels the peaks will be pointing downwards.

It is interesting to see how all the elements start out in their corresponding idle states and then, as the oscillations reach a certain amplitude, begin to change state – that is the suspension elements are sliding, the rear suspension bracket clearances are exceeded, and the wheels are oscillating from flange to flange.

3.3 Jacobi matrix

The Newton–Raphson's method used for calculating the stage derivatives (equation (3.3)) needs the Jacobi matrix $\boldsymbol{\nabla}_{\mathbf{y}}\mathbf{f}$. The (i, j)'th entry in the Jacobi matrix are numerically estimated using the central difference estimate

$$\frac{\partial f_i}{\partial y_j} \approx \frac{f_i(t, y_1, \ldots, y_j + \Delta y, \ldots, y_n) - f_i(t, y_1 \ldots, y_j - \Delta y, \ldots, y_n)}{2\Delta y} \tag{3.13}$$

where Δy is a small perturbation. Regarding the system modelling the freight wagon, the Jacobi matrix is a sparse matrix with $68 \cdot 68 = 4624$ elements. Any unnecessary computations should be avoided in approximating the Jacobi matrix because the resulting simulation time is highly dependent on this. In particular, the following optimisations are important to take into account:

- The Jacobi matrix is sparse and there is no need to numerically approximate the zeros. The dependencies of the function $\mathbf{f}$ are identified before simulation (see page 74). These dependencies yield the pattern in Figure 3.5 illustrating the nonzero entries.

- The relative kinematics and interacting forces are functions of $\mathbf{y}$. Computing the entries in the Jacobi matrix in a columnwise fashion is beneficial because the relative kinematics and interacting forces computed for the two perturbations related to y_j can be reused for all nonzero elements in the j'th column.

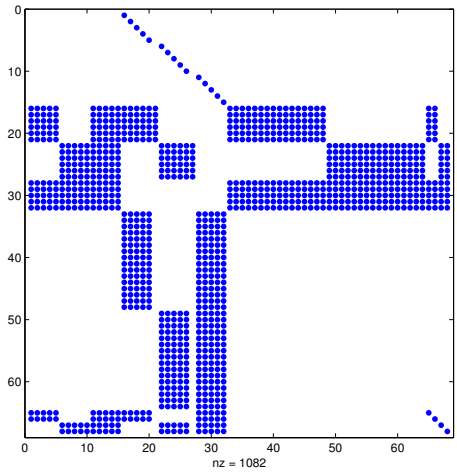

Figure 3.5: Nonzero entries in the Jacobi matrix.

$$\mathbf{f}_{1\to 15} = \left[\begin{array}{c} f_1(y_{16}) \\ f_2(y_{17}) \\ f_3(y_{18}) \\ f_4(y_{19}) \\ f_5(y_{20}) \\ \hline f_6(y_{22}) \\ f_7(y_{23}) \\ f_8(y_{24}) \\ f_9(y_{25}) \\ f_{10}(y_{26}) \\ \hline f_{11}(y_{28}) \\ f_{12}(y_{29}) \\ f_{13}(y_{30}) \\ f_{14}(y_{31}) \\ f_{15}(y_{32}) \end{array}\right] \qquad \mathbf{f}_{16\to 32} = \left[\begin{array}{c} f_{16}(y_{1\to 5}, y_{11\to 21}, y_{33\to 48}, y_{65\to 66}) \\ f_{17}(y_{1\to 5}, y_{11\to 21}, y_{33\to 48}, y_{65\to 66}) \\ f_{18}(y_{1\to 5}, y_{11\to 21}, y_{33\to 48}, y_{65\to 66}) \\ f_{19}(y_{1\to 5}, y_{11\to 21}, y_{33\to 48}, y_{65\to 66}) \\ f_{20}(y_{1\to 5}, y_{11\to 21}, y_{33\to 48}, y_{65\to 66}) \\ f_{21}(y_{1\to 5}, y_{11\to 21}, y_{33\to 48}, y_{65\to 66}) \\ \hline f_{22}(y_{6\to 15}, y_{22\to 27}, y_{49\to 64}, y_{67\to 68}) \\ f_{23}(y_{6\to 15}, y_{22\to 27}, y_{49\to 64}, y_{67\to 68}) \\ f_{24}(y_{6\to 15}, y_{22\to 27}, y_{49\to 64}, y_{67\to 68}) \\ f_{25}(y_{6\to 15}, y_{22\to 27}, y_{49\to 64}, y_{67\to 68}) \\ f_{26}(y_{6\to 15}, y_{22\to 27}, y_{49\to 64}, y_{67\to 68}) \\ f_{27}(y_{6\to 15}, y_{22\to 27}, y_{49\to 64}, y_{67\to 68}) \\ \hline f_{28}(y_{1\to 15}, y_{33\to 68}) \\ f_{29}(y_{1\to 15}, y_{33\to 68}) \\ f_{30}(y_{1\to 15}, y_{33\to 68}) \\ f_{31}(y_{1\to 15}, y_{33\to 68}) \\ f_{32}(y_{1\to 15}, y_{33\to 68}) \end{array}\right]$$

$$\mathbf{f}_{33\to 40} = \left[\begin{array}{c} f_{33}(y_{16\to 20}, y_{28\to 32}) \\ f_{34}(y_{16\to 20}, y_{28\to 32}) \\ f_{35}(y_{16\to 20}, y_{28\to 32}) \\ f_{36}(y_{16\to 20}, y_{28\to 32}) \\ f_{37}(y_{16\to 20}, y_{28\to 32}) \\ f_{38}(y_{16\to 20}, y_{28\to 32}) \\ f_{39}(y_{16\to 20}, y_{28\to 32}) \\ f_{40}(y_{16\to 20}, y_{28\to 32}) \end{array}\right] \qquad \mathbf{f}_{41\to 48} = \left[\begin{array}{c} f_{41}(y_{16\to 20}, y_{28\to 32}) \\ f_{42}(y_{16\to 20}, y_{28\to 32}) \\ f_{43}(y_{16\to 20}, y_{28\to 32}) \\ f_{44}(y_{16\to 20}, y_{28\to 32}) \\ f_{45}(y_{16\to 20}, y_{28\to 32}) \\ f_{46}(y_{16\to 20}, y_{28\to 32}) \\ f_{47}(y_{16\to 20}, y_{28\to 32}) \\ f_{48}(y_{16\to 20}, y_{28\to 32}) \end{array}\right]$$

$$\mathbf{f}_{49\to 56} = \left[\begin{array}{c} f_{49}(y_{22\to 26}, y_{28\to 32}) \\ f_{50}(y_{22\to 26}, y_{28\to 32}) \\ f_{51}(y_{22\to 26}, y_{28\to 32}) \\ f_{52}(y_{22\to 26}, y_{28\to 32}) \\ f_{53}(y_{22\to 26}, y_{28\to 32}) \\ f_{54}(y_{22\to 26}, y_{28\to 32}) \\ f_{55}(y_{22\to 26}, y_{28\to 32}) \\ f_{56}(y_{22\to 26}, y_{28\to 32}) \end{array}\right] \qquad \mathbf{f}_{57\to 64} = \left[\begin{array}{c} f_{57}(y_{22\to 26}, y_{28\to 32}) \\ f_{58}(y_{22\to 26}, y_{28\to 32}) \\ f_{59}(y_{22\to 26}, y_{28\to 32}) \\ f_{60}(y_{22\to 26}, y_{28\to 32}) \\ f_{61}(y_{22\to 26}, y_{28\to 32}) \\ f_{62}(y_{22\to 26}, y_{28\to 32}) \\ f_{63}(y_{22\to 26}, y_{28\to 32}) \\ f_{64}(y_{22\to 26}, y_{28\to 32}) \end{array}\right]$$

$$\mathbf{f}_{65\to 68} = \left[\begin{array}{c} f_{65}(y_{1\to 5}, y_{11\to 20}, y_{28\to 32}, y_{65}) \\ f_{66}(y_{1\to 5}, y_{11\to 20}, y_{28\to 32}, y_{66}) \\ f_{67}(y_{6\to 15}, y_{22\to 26}, y_{28\to 32}, y_{67}) \\ f_{68}(y_{6\to 15}, y_{22\to 26}, y_{28\to 32}, y_{68}) \end{array}\right]$$

Chapter 4

Implementation

4.1 Analysis and design

The freight wagon model is implemented in `C++` providing an excellent environment for efficient object oriented programs. The program structure is described in the following.

Bodies For each body in the model an object is instantiated holding the characteristic quantities defining the body, i.e. mass, inertia around the principal axes, equilibrium position of centre of mass. These quantities are defined in a common super class `body`. Derived from this class is the `wheelset` and `carbody` classes that besides the characteristic quantities mentioned above includes the position and orientation coordinates for the wheelset and carbody, respectively. The position and orientation of the wheelset is defined through: $D_x, D_y, D_z, D_\phi, D_\psi, D_\beta$. Likewise, for the carbody: $D_y, D_z, D_\phi, D_\theta, D_\psi$. See Figure 4.2 for an illustration. The source code related to the above mentioned classes are found in `bodies.h`, `wheelset.cpp` and `carbody.cpp`.

Event system The event system is built around the abstract interface `evt_base` having the virtual functions and variables shown in Figure 4.1. All submodels of the nonsmooth interacting forces are implemented as classes derived from the `evt_base`. The virtual declaration is beneficial because the implementation of the function is to be specified in the derived classes. Regarding the event system the state machine function, `sm(...)`, event function, `g(...)` and

action command function, `action(...)`, are all basic functions with model specific implementations. The boolean `active` indicates whether or not an event has occurred within the time step, and the variable `state` holds the state of the element.

```
virtual void sm(double tn, double hn, double theta) = 0;
virtual double g(double tn, double hn, double theta, int i) = 0;
virtual void action(DVector &y) = 0;

bool active;
int state;
```

Figure 4.1: The abstract interface `evt_base`.

The dead band spring, elastic dry friction element, longitudinal guidance model, leaf spring, track and wheel–rail contact are all implemented as classes derived from the abstract interface `evt_base`, and they are gathered into the event list (see Table 3.2) declared by `evt_base *evtlist[59]`. See Figure 4.3 for an illustration. The event location algorithm (Algorithm 2) is found in `evtdet.cpp`. The source code related to the event system is found in `events.h`, `evtdet.cpp`, `events_base.cpp`, `events_dbs.cpp`, `events_dfe.cpp`, `events_gl.cpp`, `events_ls.cpp`, `events_tr.cpp` and `events_wr.cpp`.

Auxiliary objects The nodes and function values of the track curvatures and the superelevation are defined by constructing a track object. The object contains an interface for the formulas in section 2.1.7 in order to find the curvilinear parameters. The `track` object is implemented in `track.h`, `track.cpp`.

As described in section 2.2.3 the contact table is divided into continuous sections. The contact parameters regarding a specific section is stored in a `section` object. Besides holding the contact parameters this object also provides a function through which the table can be interpolated given the lateral displacement of the wheelset. The `section` object is implemented in `section.h`, `section.cpp`.

Freight wagon model The entire freight wagon model is built using a `wagon` object. This object provides a convenient interface for the relative kinematics, interacting forces and equations of motion. The class is defined in `freightwagon.h` (see Figure 4.4), the basic functions related to the `wagon` object are found in `freight_main.cpp`, the resultant forces and torques acting on the bodies are computed in `freight_forces.cpp`, the initial condition of the freight wagon is specified in `freight_ic.cpp`, solution output from the model are implemented in `freight_io.cpp`, and the model parameters for the different wagons investigated in this project are found in `freight_wagons.cpp`.

Integration method The ESDIRK implementation by Østergaard [106] is used. The ESDIRK library is accessed through the creation of a `Sdirk` object. The code has been extended so it is possible to externally access the continuous extension which is needed for the event system. The ESDIRK code needs an implementation of the right hand side function $\mathbf{f}$ and its corresponding Jacobi matrix $\partial\mathbf{f}/\partial\mathbf{y}$. These are implemented in `system.cpp`.

Simulation scripts The `main` function of the program and the basic integration loop regarding the initial value problem are found in `integrate.cpp`. A `wagon` object and a `Sdirk` object are created. They provide the needed references to the freight wagon model and the ESDIRK library. See Figure 4.5 for an illustration. Interfacing the `C++` code from Java is also possible using function declarations according to the Java Native Interface (JNI). This feature is made available in `integrate_jni.cpp` which basically is a clone of `integrate.cpp`.

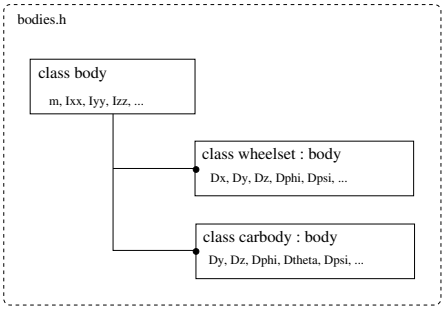

Figure 4.2: Bodies.

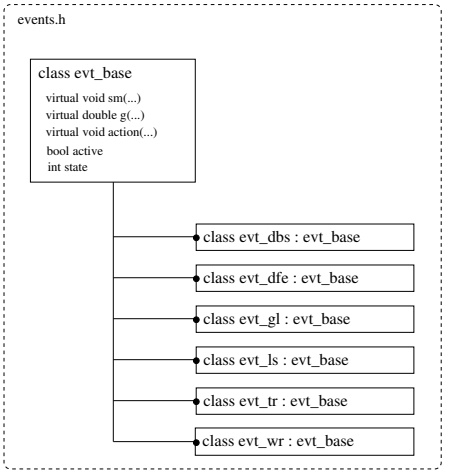

Figure 4.3: Event system.

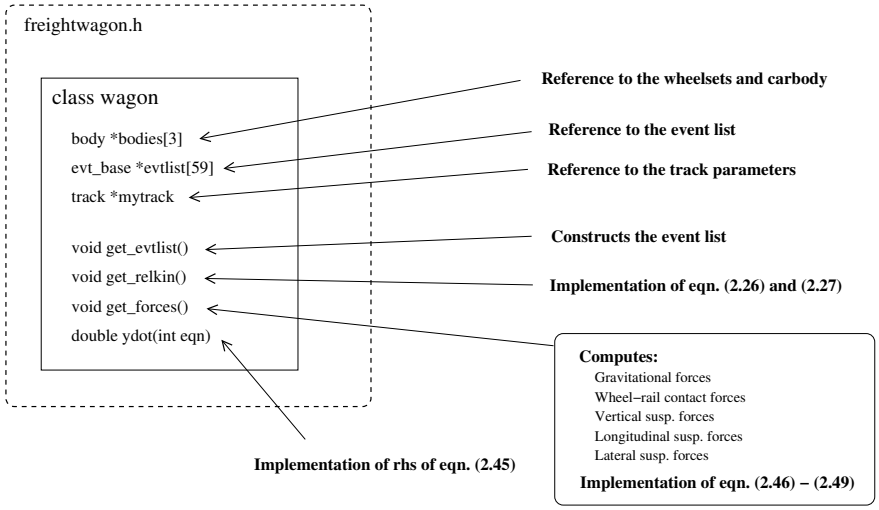

Figure 4.4: Freight wagon.

```
integrate.cpp (simulation script)

  Sdirk *solver
  wagon *wag

  void simulate() {
    solver = new Sdirk(...)
    wag = new wagon(...)
    Set initial condition
    do {
      Integrate one step
      Check for events (Algorithm 2)
    } while (t < tend)

  }
```

Figure 4.5: Simulation script.

4.2 TAFWA code

A graphical user interface is created on top of the freight wagon model. The GUI is programmed in Java and is integrated with the model using the Java Native Interface (JNI) [33]. This framework constitutes the TAFWA[1] program and has been used to analyse the two–axle freight wagons in this project. TAFWA provides a simple interface for simulating and analysing the wagons, and complicated model details are hidden from the user. Screen–shots from TAFWA are shown in Figure 4.6 and 4.7. The `solve` pane contains the wagon simulator. A simulation is simply started by selecting a wagon from the list and then clicking `start`. The `C++` model is then activated in its own thread such that it will not lock the entire program during simulation. After the simulation has ended the results can be analysed using the utilities found in the `visualise` pane. Here a general purpose plotting program is found. For a quick analysis, click `load` to specify the solution file and use the `Quick plot` features (`1` is time history of the lateral motion of the bodies, `2` is longitudinal suspension analysis, `3` is lateral suspension analysis, `4` is vertical suspension analysis, and `5` is wheelset analysis).

In order to simulate a new wagon using the TAFWA code we execute the following steps:

1. Make a new function with the wagon data in `freight_wagons.cpp` (e.g. by copy–paste an old one)
2. Make a prototype of this function in `freightwagon.h`
3. Update the wagon list in `freight_main.cpp`
4. Find the equilibrium position of the new wagon using `get_z` function in `integrate.cpp`
5. To be able to select the wagon using the GUI it is necessary to update the wagon list in `SolveControlPanel.java` and to put a `html` description file in the `html` directory

The program is most easily compiled and started using the `Makefile` provided. Compile by `make`, and start TAFWA by `make run`. The model can also be used without the GUI by `make cpponly` and `make runcpp`. On the Solaris system use `gmake` instead of `make`. It might be necessary to modify the JNI path in the `Makefile` in order to match the Java installation directory on the system used.

[1] Two–axle freight wagon analyser

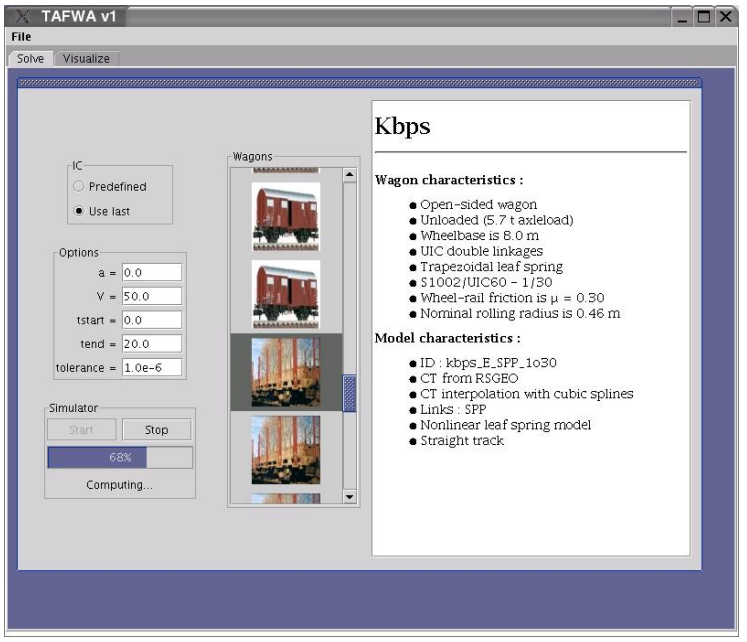

Figure 4.6: The simulator.

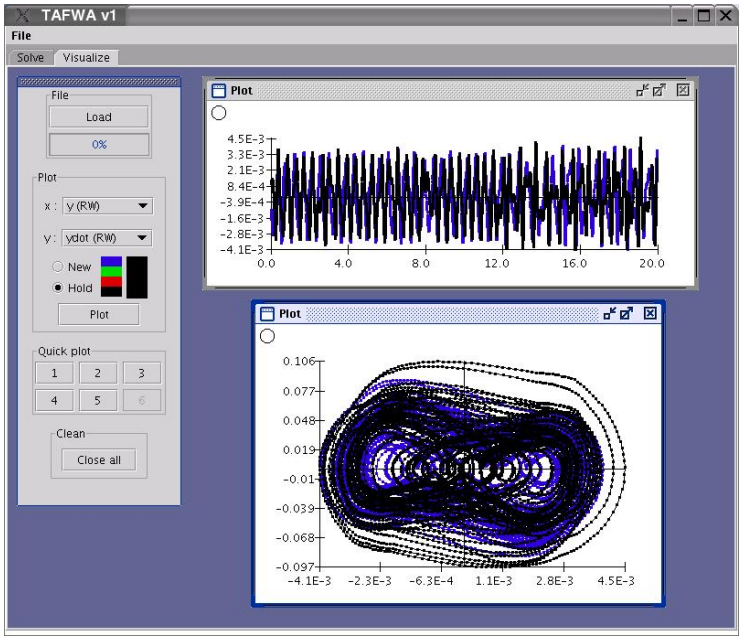

Figure 4.7: The visualising toolbox.

Chapter 5

Results

The running properties of two–axle freight wagons are not always satisfactory on straight track due to the well known and unwanted hunting motion. Using the model developed, it is possible to shed some light on the complex dynamic behaviour of these wagons.

Time domain simulations and bifurcation diagrams provide the basic approach of analysis because they do not rely on simplified formulations of the model. A bifurcation diagram is a convenient tool in the analysis of nonlinear dynamical systems. It shows the long–term behaviour of the system as a function of a (bifurcation) parameter. An equilibrium state for which the system evolves after long enough time is called an attractor. A hallmark of dissipative nonlinear systems like the freight wagon model presented here is that multiple attractors might coexist for the same parameter value [94, 86].

5.1 Stability on straight track

The running properties of rail vehicles are sensitive to the contact geometry between the wheel and rail, and the two–axle freight wagon is no exception to this. All results presented here are based on the European standard wheel–rail profile combination S1002/UIC60. The rail inclination (see Figure 2.14) is not the same throughout Europe, for instance it is 1/40 in Germany, 1/30 in Sweden and 1/20 in France. For the two–axle freight wagons the rail inclination has an important qualitative influence on the running properties. The bifurcation diagrams in Figure 5.1 to 5.3 illustrate this for the Hbbills 311 wagon using the

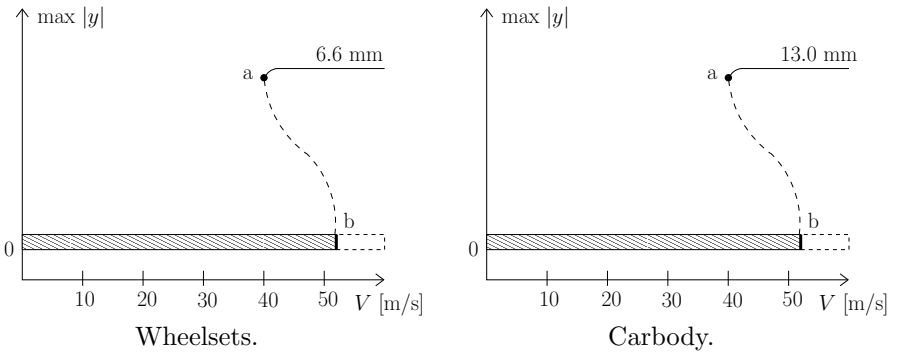

Figure 5.1: Attractors, 1/20 rail inclination.

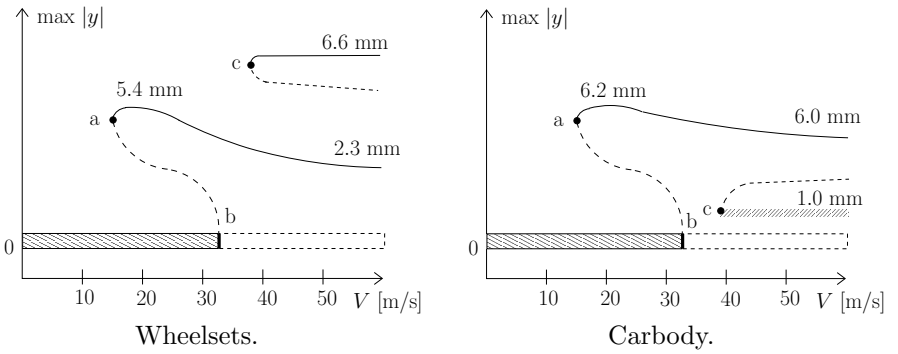

Figure 5.2: Attractors, 1/30 rail inclination.

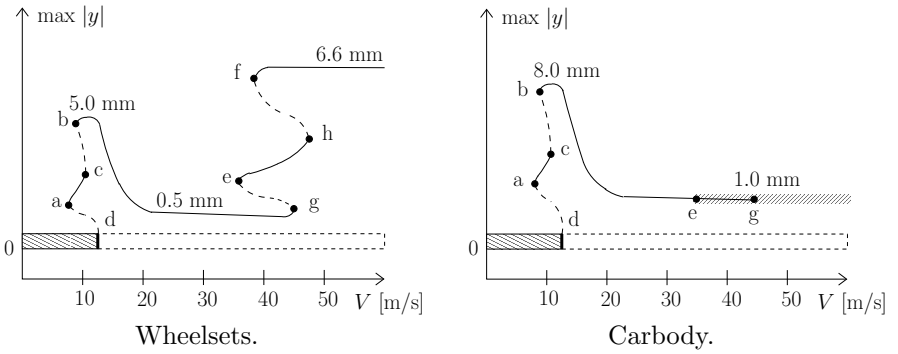

Figure 5.3: Attractors, 1/40 rail inclination.

PTP suspension parameters. The two other wagons have the same qualitative behaviour. The speed is the bifurcation parameter and the ordinate indicates the maximum lateral displacement of the bodies measured in the track system. Stable and unstable equilibrium states are shown by solid and dashed lines, respectively.

The *stationary solution* in the centre of the track is not well defined due to the dry friction in the UIC links. This is shown by giving the stationary solution a finite width. This width depends on the instantaneous friction parameters in the suspension. The rail inclination is seen to have a strong influence on the stability of the stationary solution. In the case with 1/20 rail inclination the stability is lost at high speed whereas it is lost at very low speed for 1/40 rail inclination. The stability of the stationary solution is lost in a subcritical Hopf–bifurcation.

The nonlinearity in the system is responsible for the fact that multiple attractors coexist. A high amplitude attractor appears for the wheelsets at high speeds. It will be denoted the *flange–to–flange attractor* because the wheelsets moves from flange to flange. The wheel flanges are limiting the lateral motion of the wheelset, and the amplitude is basically the distance to the flange. If the wheelsets are on this attractor, the carbody responds with a violently oscillating motion in the 1/20 rail inclination case. This is in contrast to the motion found with the 1/30 and 1/40 rail inclinations where the carbody has a small amplitude oscillation around 1 mm with an irregular pattern.

In the case with 1/30 and 1/40 rail inclinations, there exists also a periodic *medium amplitude attractor* with increasing amplitude for decreasing speed. The sudden increase in amplitude is a consequence of a resonance motion of the wagon. As suggested by Stichel in [80, 81] a resonance between the lateral excitation frequency of the wheelsets and the yaw eigenfrequency of the carbody might occur. These frequencies can be approximated by the formulas in equation (5.1). The wheelset lateral excitation frequency is approximated by Klingel's formula.

$$f_{yaw} = \frac{1}{2\pi}\sqrt{\frac{4a^2 k_y}{I_{zz}}} \qquad , \qquad f_w = \frac{V}{2\pi}\sqrt{\frac{\lambda}{b_0 r_0}} \tag{5.1}$$

Here, a is the half wheelbase, k_y is the lateral suspension stiffness, I_{zz} is the yaw moment of inertia of the carbody, V is the speed, λ is a wheel conicity, $2b_0$ is the distance between the nominal rolling circles and r_0 is the nominal rolling radius. The nonlinearities in the suspension as well as the wheel–rail geometry make k_y and λ dependent on the current configuration of the system. Estimating the suspension stiffness using the PTP parameters with a deformation of 10 mm and letting the conicity be defined by the equivalent conicity (see e.g. Table 7–8 in [1]) the relations depicted in Figure 5.4 can be found for the Hbbills 311 wagon. From the figure it is seen that the excitation frequency of the wheelsets coincide with the yaw eigenfrequency of the carbody at 12 m/s, 18 m/s and 49

m/s for 1/40, 1/30 and 1/20 rail inclination, respectively.

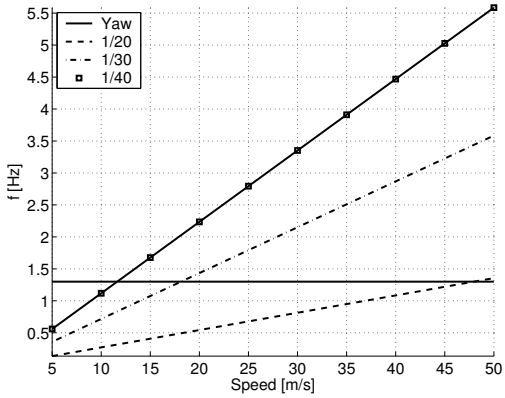

Figure 5.4: Comparing the eigenfrequency of the yaw mode of the carbody with Klingel's estimate of the lateral excitation frequency of the wheelsets.

Even though this estimate of resonance is an approximate one, it actually helps interpreting the bifurcation diagrams. The peaks of the medium amplitude attractor in the 1/30 and 1/40 case are due to this resonance. There is no medium amplitude attractor in the 1/20 case, however, the resonance still occurs at 49 m/s as predicted – but in the speed interval for which the wheelsets are on the flange–to–flange attractor. The carbody also oscillates dramatically in this case.

The fact that the nonlinearity in the link suspension characteristics is of the softening type, i.e. the suspension stiffness decreases when sliding sets in (Figure 2.49), could explain why all the resonance curves are bending to the left [41]. It is further noted that the resonance attractor disappears in a saddle–node bifurcation for all three rail inclinations.

On the flange–to–flange attractor, in the case with 1/30 and 1/40, the lateral excitation frequency of the wheelsets are far beyond the yaw eigenfrequency of the carbody, hence no resonance occurs and the result is a weak carbody response. The spectral analysis shown in Figure 5.5 and 5.6 highlights the different frequencies found in the lateral motion of the front wheelset on the flange–to–flange attractor in case 1/20 and 1/40. The frequency is 1.3 Hz for the 1/20 rail inclination and 6.4 Hz for the 1/40 rail inclination. Although, the amplitude of the flange–to–flange attractor is almost constant (and equal to the distance to the flange) the width of the peaks in the power spectrum reveals that the flange–to–flange motion is actually aperiodic. The abrupt guiding force from the flange is held responsible for this behaviour.

The attractors can be illustrated by starting out at high speed and then decelerate until the stationary solution is the only stable attractor left. This is done for the three rail inclinations with the Hbbills 311 wagon using the

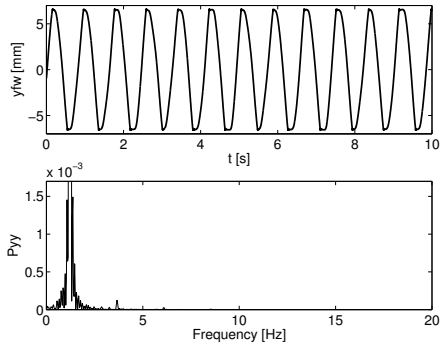

Figure 5.5: Hbbills 311 (empty, PTP, 1/20) running at 50 m/s.

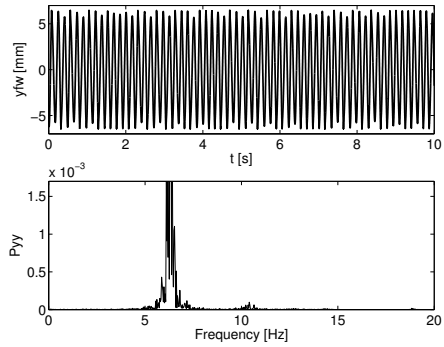

Figure 5.6: Hbbills 311 (empty, PTP, 1/40) running at 45 m/s.

PTP parameters and the results are shown in Figure 5.7 to 5.9. The figures to the left show the contact angle as a function of the lateral displacement of the wheelset. The time series of the speed, lateral position of front wheelset and lateral position of carbody are shown in the figures to the right. The contact angle helps in interpreting the amplitude of the different attractors related to the wheelsets. It is interesting to watch how the oscillation of the carbody suddenly increases in amplitude due to the bifurcation c in the situation with 1/30 rail inclination.

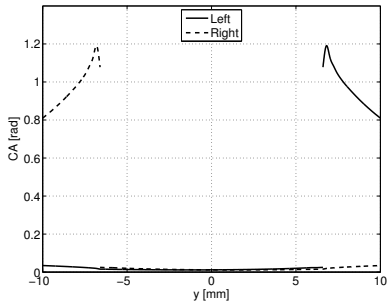

Contact angle.

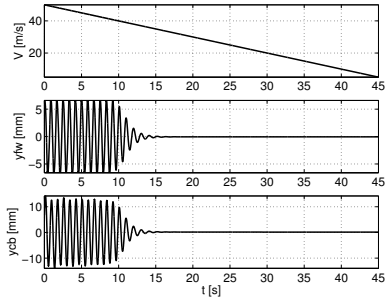

Decelerating from 50 m/s.

Figure 5.7: Shadowing attractors by decelerating from 50 m/s to 5 m/s.

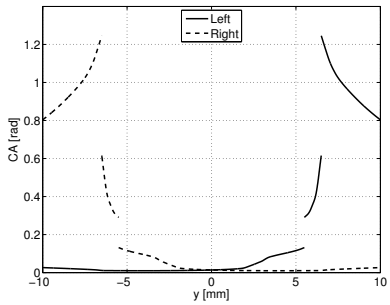

Contact angle.

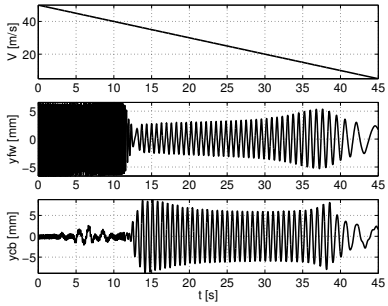

Decelerating from 50 m/s.

Figure 5.8: Shadowing attractors by decelerating from 50 m/s to 5 m/s.

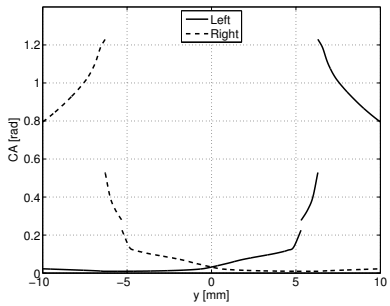

Contact angle.

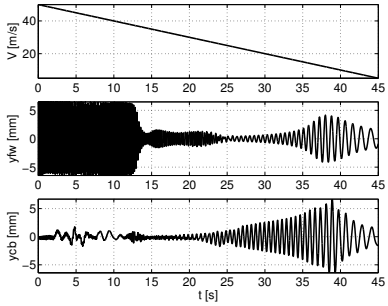

Decelerating from 50 m/s.

Figure 5.9: Shadowing attractors by decelerating from 50 m/s to 5 m/s.

The resonance in the carbody yaw mode is confirmed in the illustration of the yaw angles shown in Figure 5.10. This plot is obtained from the same simulation as in Figure 5.9. The yaw motion of the carbody is seen to increase towards the resonance at 12 m/s. Figure 5.11 depicts the special situation of the Hbbills 311 wagon running at 40 m/s with 1/40 rail inclination where three coexisting attractors are present. They are illustrated here through time series of the front wheelset.

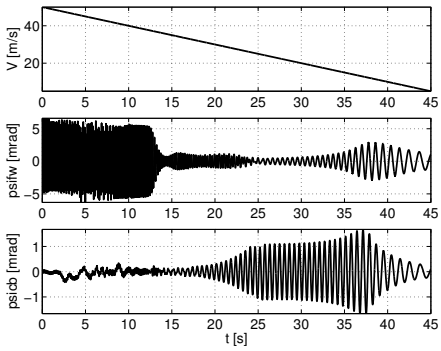

Figure 5.10: Time series of yaw angles. Hbbills 311 (empty, PTP, 1/40).

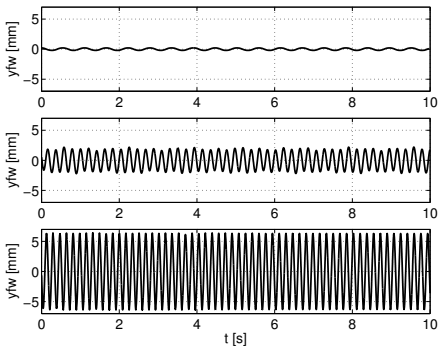

Figure 5.11: Three coexisting attractors at 40 m/s. Hbbills 311 (empty, PTP, 1/40).

The parameters used for the model of the UIC links influence the simulation results. The PTP parameters provide a good reference because they are theoretically found using the (idealised) nominal cylindrical geometry of the UIC links. As indicated by the parameters in Table 2.4 (section 2.3.3) the rolling stiffness is often very different from measurement to measurement. In the work by Jönsson [36] it is also noted that the rolling stiffness typically increases with wear. The results in Figure 5.12 are obtained from the Hbbills 311 wagon with 1/40 rail inclination but using the SPP parameters. These parameters differ from the PTP by having a more stiff rolling phase. A quantitative difference is observed by comparing with the reference case (Figure 5.9). The flange–to–flange attractor disappears at 66 m/s instead of 38 m/s. Furthermore, the stiffer lateral suspension increases the yaw eigenfrequency of carbody, see equation (5.1), hence the resonance motion occurs at higher speed, i.e. 18 m/s.

Simulating with the experimentally identified parameters MP generates the results in Figure 5.13. The parameters are characterised by a short rolling phase due to a low break out force in the links. The sliding phase is pronounced and dissipation occurs at small displacements. This clearly influences the amplitude of the oscillations at resonance speed which are seen to be small. The flange–to–flange attractor is also moved slightly to lower speeds such that it exists until 35 m/s.

Breaking the symmetry in the suspension parameters has an interesting ef-

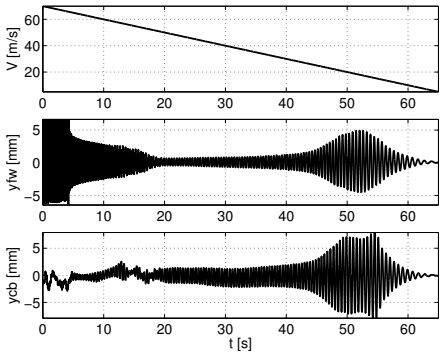

Figure 5.12: Stiff rolling phase. Hbbills 311 (empty, SPP, 1/40).

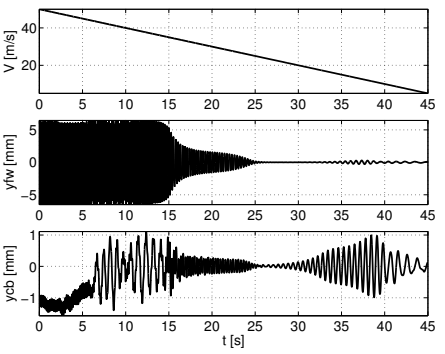

Figure 5.13: Low break out force. Hbbills 311 (empty, MP, 1/40).

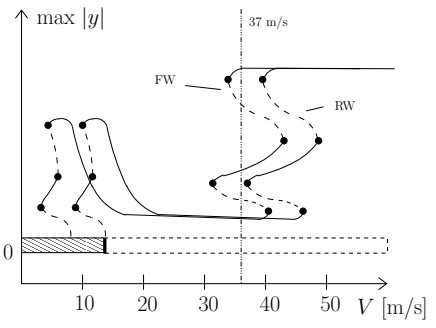

Figure 5.14: Asymmetric suspension parameters breaks the symmetry in the wheelset attractors.

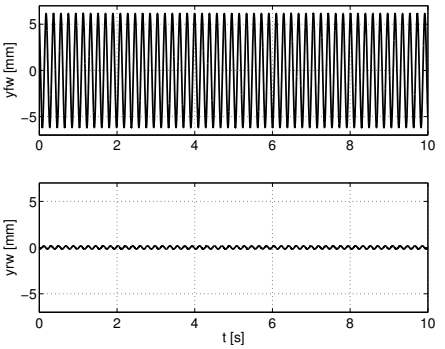

Figure 5.15: Simulation at 37 m/s with asymmetric suspension parameters.

fect on the wheelset attractors. This is illustrated by the results in Figure 5.14 obtained with UIC link parameters having different friction coefficients and assuming the cylindrical geometry [61]. The friction coefficients used are

$$f_{FL} = 0.1 \quad , \quad f_{FR} = 0.3 \quad , \quad f_{RL} = 0.5 \quad , \quad f_{RR} = 0.2$$

where FL, FR, RL, RR denote the front left, front right, rear left, rear right horizontal suspension model, respectively. The broken symmetry in the suspension parameters break the symmetry in the wheelset attractors as well. Running at e.g. 37 m/s, the special scenario occurs where the front wheelset is on the flange–to–flange attractor and the rear wheelset is not, see Figure 5.15.

According to the formula of the yaw eigenfrequency of the carbody in equation (5.1) an increased yaw moment of inertia should decrease the yaw eigenfrequency of the carbody. This is also confirmed by the results of an analysis that is shown in Figure 5.16. However, the effect is weak due to the square root in the formula for the eigenfrequency, see equation (5.1).

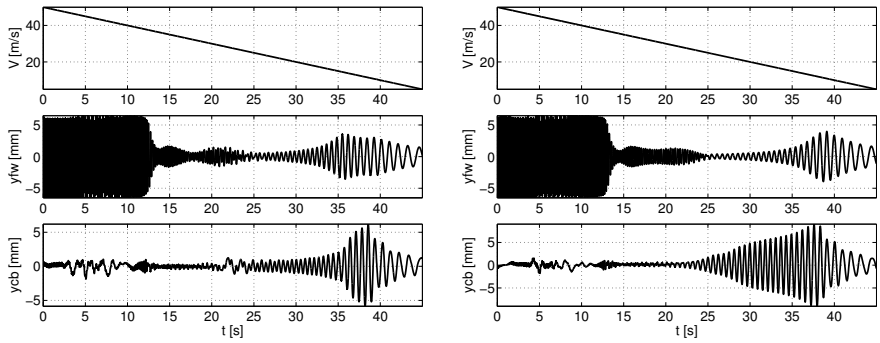

$I_{zz} - 20\%$. $I_{zz} + 20\%$.

Figure 5.16: A demonstration of the influence of the yaw moment of inertia of the carbody on the dynamics. Hbbills 311 (empty, PTP, 1/40).

Next, the Hbbills 311 wagon is simulated in a loaded configuration (22.5 t axle load). The mass and inertia of the carbody are changed to

$$m_{cb} = 41176.0 \text{ kg} \qquad I_{xxcb} = 66492.0 \text{ kg m}^2$$
$$I_{yycb} = 993040.0 \text{ kg m}^2 \qquad I_{zzcb} = 986832.0 \text{ kg m}^2$$

These inertias are found by assuming that the load is a homogeneous box of 26 t with dimensions $(l, w, h) = (16.01, 2.90, 2.35)$ m. The simulation results are shown in Figure 5.17 and 5.18 for two different heights of the centre of mass. In both cases the flange–to–flange motion only exists for speeds higher than 60 m/s. The resonance motion still occurs at low speed (12 m/s) despite the fact that the yaw moment of inertia of the carbody is significantly bigger compared to the empty wagon. The reason for this is that the stiffness of the pendular suspension system is correspondingly more stiff such that the yaw eigenfrequency of the carbody is almost the same, see equation (5.1).

Regarding the motion of the loaded wagon with the high centre of mass, it is noted that in a speed interval around 33 m/s the amplitude of the attractor increases. The explanation for this is that a roll mode of the carbody is excited. The eigenfrequency of the roll motion can be approximated by equation (5.2).

$$f_{roll} = \frac{1}{2\pi}\sqrt{\frac{4(L_1^2 k_z + L_2^2 k_y)}{I_{xx}}} \tag{5.2}$$

where $L_1 = 1.0$ m and $L_2 = \bar{z}_{cb} - r_0$ are the lateral and vertical distances between the centre of mass and the UIC suspension, respectively. The lateral suspension stiffness k_y is estimated as described for the yaw eigenfrequency and k_z reflects the dynamic stiffness of the leaf spring. For the empty wagon, the roll eigenfrequency is actually about the same as the yaw eigenfrequency, however, the roll mode is not excited because, typically, the wheelsets are oscillating with a phase difference, which prevents a severe roll motion of the carbody. For the loaded wagon, the roll eigenfrequency is changed to about 3.3 Hz primarily due to the stepwise progressive suspension stiffness of the two–stage parabolic leaf spring. This roll mode can get excited if the wheelsets are moving at 30 m/s (see Figure 5.4) without a phase shift, and this is exactly the situation for the loaded wagon with the high centre of mass.

Figure 5.19 and 5.20 illustrate how the motions of the wheelsets differ when the yaw and roll modes are excited. At 14 m/s the wheelsets oscillate with a phase shift and the yaw mode is excited, and at 33 m/s the wheelsets oscillate in phase and the roll mode is excited.

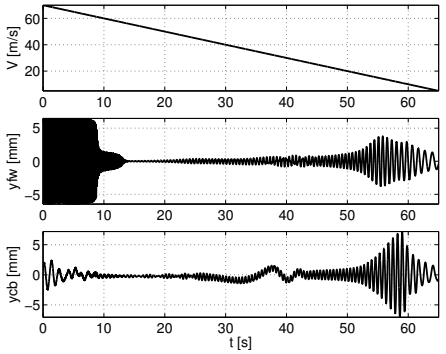

Figure 5.17: A simulation of a loaded wagon. Hbbills 311 (loaded, PTP, 1/40). Centre of mass is 1.6 m above track plane.

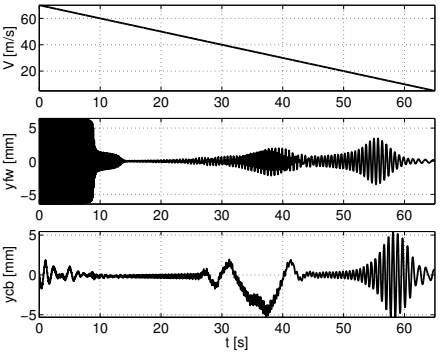

Figure 5.18: A simulation of a loaded wagon. Hbbills 311 (loaded, PTP, 1/40). Centre of mass is 2.1 m above track plane.

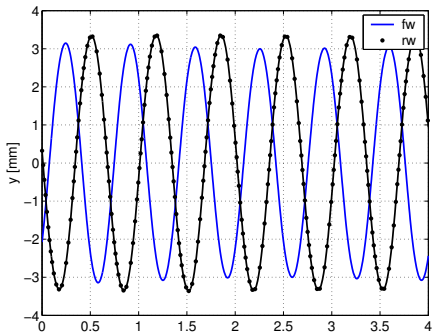

Figure 5.19: A simulation of a loaded wagon. Hbbills 311 (loaded, PTP, 1/40) at 14 m/s. Centre of mass is 2.1 m above track plane.

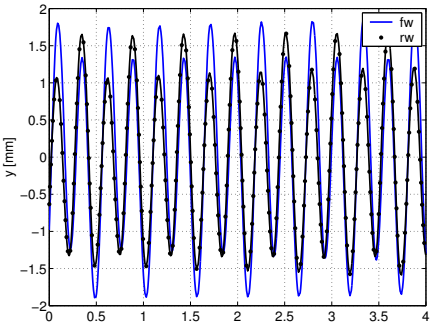

Figure 5.20: A simulation of a loaded wagon. Hbbills 311 (loaded, PTP, 1/40) at 33 m/s. Centre of mass is 2.1 m above track plane.

5.2 Comparing wagons

The Kbps and G69 wagons from Table 2.7 have been simulated for comparison reasons and the results are presented in Figure 5.21 to 5.24. Qualitatively, the Kbps and G69 wagons behave as predicted by the bifurcation diagrams in Figure 5.1 to 5.3, i.e. the rail inclination basically determines the existence and amplitude of the attractors. On the other hand, quantitative differences are found in the simulations of the Kbps and G69 wagons. Note how the flange–to–flange attractor for the G69 in Figure 5.23 exists until 22 m/s due to its short wheel base, and that the medium amplitude attractor of the Kbps wagon in Figure 5.22 has an irregular pattern at high speeds ($35 - 55$ m/s).

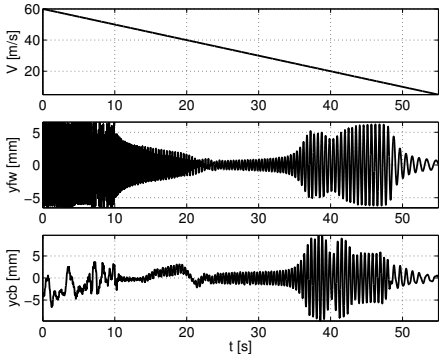

Figure 5.21: Kbps (empty, SPP, 1/40).

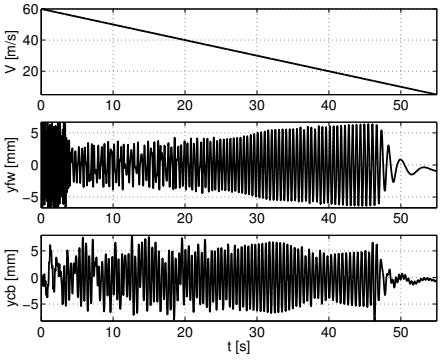

Figure 5.22: Kbps (empty, SPP, 1/30).

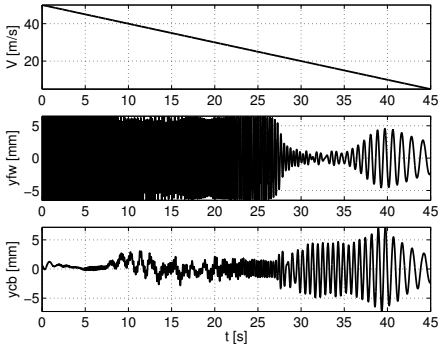

Figure 5.23: G69 (empty, PTP, 1/40).

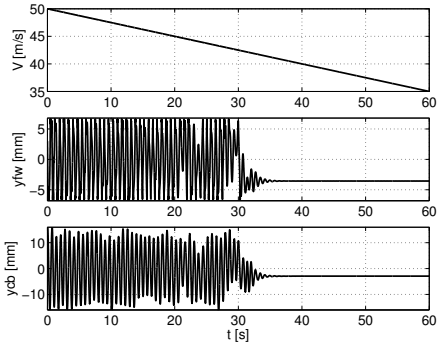

Figure 5.24: G69 (empty, INP, 1/20).

The irregular motion of the Kbps wagon in Figure 5.22 is analysed in further detail. A spectral analysis of the lateral motion of the front wheelset at 55 m/s reveals a broad spectrum of frequencies indicating a chaotic motion, see

Figure 5.25. The chaotic motion is further confirmed by the phase portrait in Figure 5.26. A sensitivity in the initial condition has to be present if the attractor is truly chaotic. This is investigated through two simulations (Sim 1 and Sim 2) starting at $t = 0$ with identical initial conditions except that $y_{fw}^{\text{sim2}} \equiv y_{fw}^{\text{sim1}} + 10^{-6}$. The solutions diverge from each other and after 15 seconds their motions are completely different, see Figure 5.27.

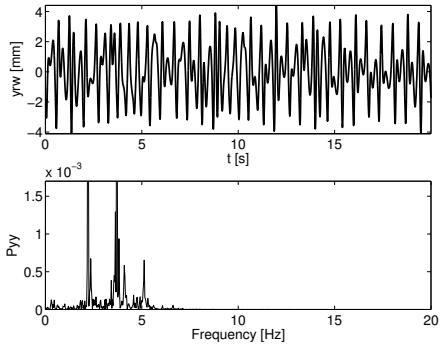

Figure 5.25: Kbps (empty, SPP, 1/30) running at 55 m/s.

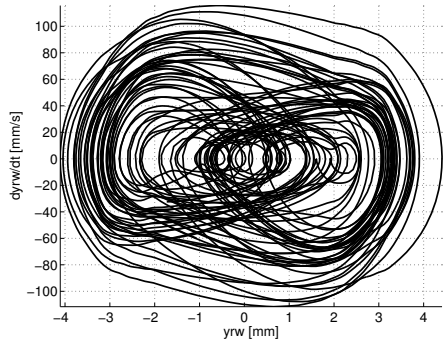

Figure 5.26: Phase portrait ($\dot{y}_{rw}$ vs y_{rw}) of the chaotic motion at 55 m/s. Kbps (empty, SPP, 1/30).

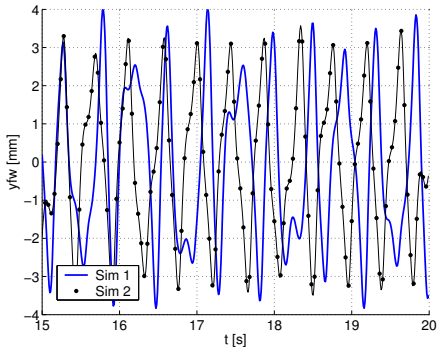

Figure 5.27: Kbps (empty, SPP, 1/30) running at 50 m/s. The chaotic attractor exhibits a sensitivity to the initial condition.

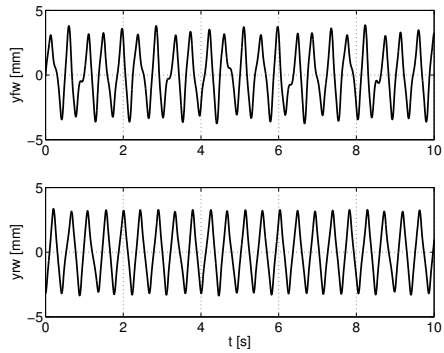

Figure 5.28: Wheelset behaviour at 43 m/s.

It is now investigated how the periodic medium amplitude attractor (at low speed) bifurcates into the chaotic attractor (at high speed) regarding the Kbps wagon. The numerical bifurcation diagrams in Figure 5.29 to 5.31 illustrate this. The bifurcation diagrams are obtained using the steps:

1. Simulate the transient for 20 s.
2. Continue simulation and extract the next 20 maxima from the time series of the lateral displacement.
3. Change the speed by 0.2 m/s (either up or down) and goto 1.

In the speed range $30 - 34$ m/s the 20 maxima defines a single point in the diagram, and hence it is a periodic motion with constant amplitude. At 34 m/s it bifurcates into another motion. The motion is no longer periodic but has a chaotic motion imposed on top of it. It is noted that there is a periodic window in the range 39 m/s to 41 m/s which is typical for systems with chaotic behaviour. At 46 m/s another bifurcation occurs that results in a chaotic attractor for speeds greater than 46 m/s.

Regarding the front wheelset, it is observed that peaks exist near the centre of the track in the range 40 m/s to 45 m/s. The stationary solution is found to be stable until 49 m/s for the Kbps wagon with the SPP parameters and the 1/30 rail inclination. The coexisting attractors (stationary and chaotic) both seem to influence the bifurcation diagram in this speed range. The local extrema near the centre of the track are also visible in the time series shown in Figure 5.28.

The diagrams are made for increasing speed as well as decreasing speed in order to reveal any possible hysteresis in relation to the bifurcations. The periodic attractor ($30 - 34$ m/s) has a minor jump, and hysteresis is found in relation to this jump. Apart from this, no hysteresis is observed.

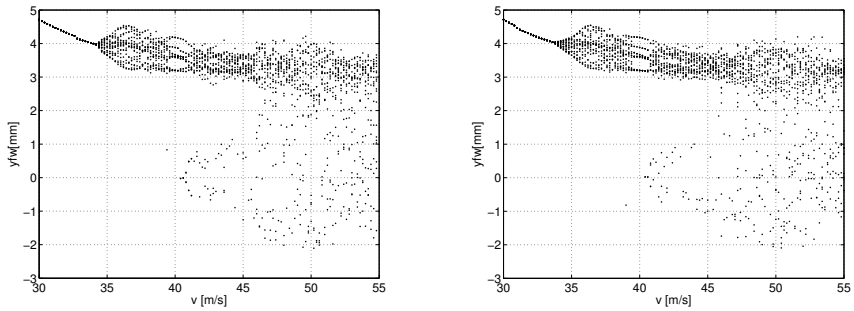

Increasing speed. Decreasing speed.

Figure 5.29: Bifurcation diagram of the front wheelset. Kbps (empty, SPP, 1/30).

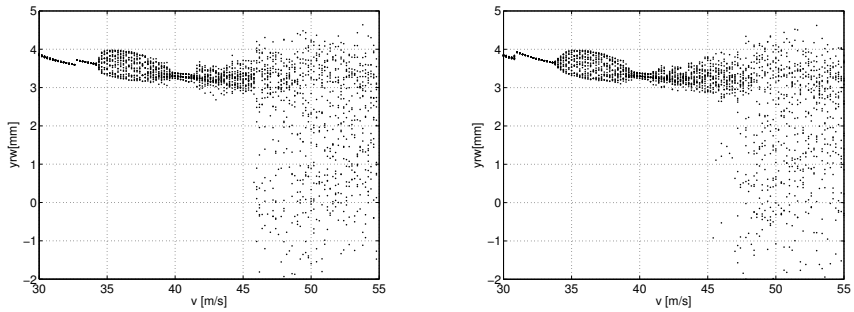

Increasing speed. Decreasing speed.

Figure 5.30: Bifurcation diagram of the rear wheelset. Kbps (empty, SPP, 1/30).

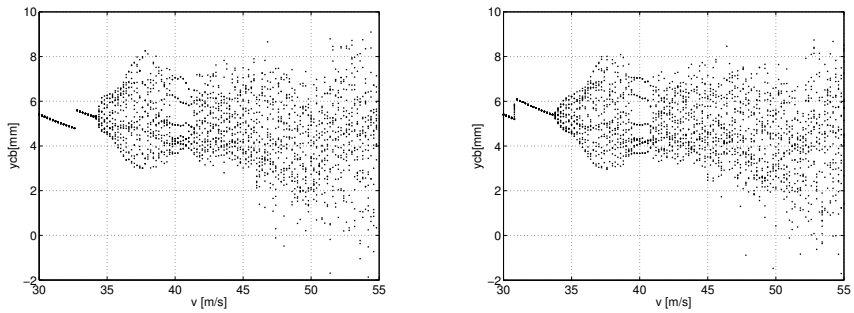

Increasing speed. Decreasing speed.

Figure 5.31: Bifurcation diagram of the carbody. Kbps (empty, SPP, 1/30).

5.3 Curved track analysis

The Hbbills 311 wagon is sent through a left hand curve to analyse its behaviour in curves. The radius of the circular part of the curve is 1000 m with a track cant of 150 mm. The transition curve is linear and has a linear ramp. Results obtained by running at 20 m/s and 30 m/s are shown in Figure 5.32 and 5.33, respectively. The equilibrium speed, i.e. the speed for which the track plane acceleration vanishes, is 31.3 m/s for this curve.

The wagon starts out in the centre of the track before it enters the curve. The stationary solution is unstable and hence the wagon is thrown out on the periodic attractor by the curve and it stays on this attractor after leaving the curve. In the curve, the wheelsets approach the right rail. Especially, the front wheelset is significantly displaced and provides the basic guiding of the wagon through the curve. The positive lateral displacement of the carbody is caused by two effects: the geometric curving overthrow and the roll of the carbody. The geometric curving overthrow is due to the fact that the mid–section of the carbody is taking a short cut through the curve. In other words, the carbody defines a chord in the circular part of the curve.

The roll angles of the bodies are influenced by the track cant. The ramp in the transition curve influences the pitch of the carbody. When the carbody enters the curve the leading part is lifted relative to the trailing part, and when it leaves the curve the opposite is true. The yaw angles of the wheelsets indicate that the wheelsets are positioning themselves almost radially in the curve with a tendency to be slightly underradial.

From the vertical suspension deformations, it is seen that at the entrance to the curve an additional deformation of the front right vertical suspension of the vehicle (FRZ) is generated. It is caused by the increasing cant. The front left vertical suspension (FLZ) is correspondingly less deformed. Leaving the curve has the opposite effect on the vertical suspension deformations. It is seen from the results at 20 m/s that the carbody is leaning slightly on the left suspension in the circular part of the curve. This is because the speed is below the equilibrium speed and consequently there is a cant excess[1]. When the wagon runs at 30 m/s (close to the equilibrium speed) the carbody suspension deformation in the circular part of the curve is seen to be equal to the deformations on straight track.

[1]The real cant is greater than the equilibrium cant (zero track plane acceleration)

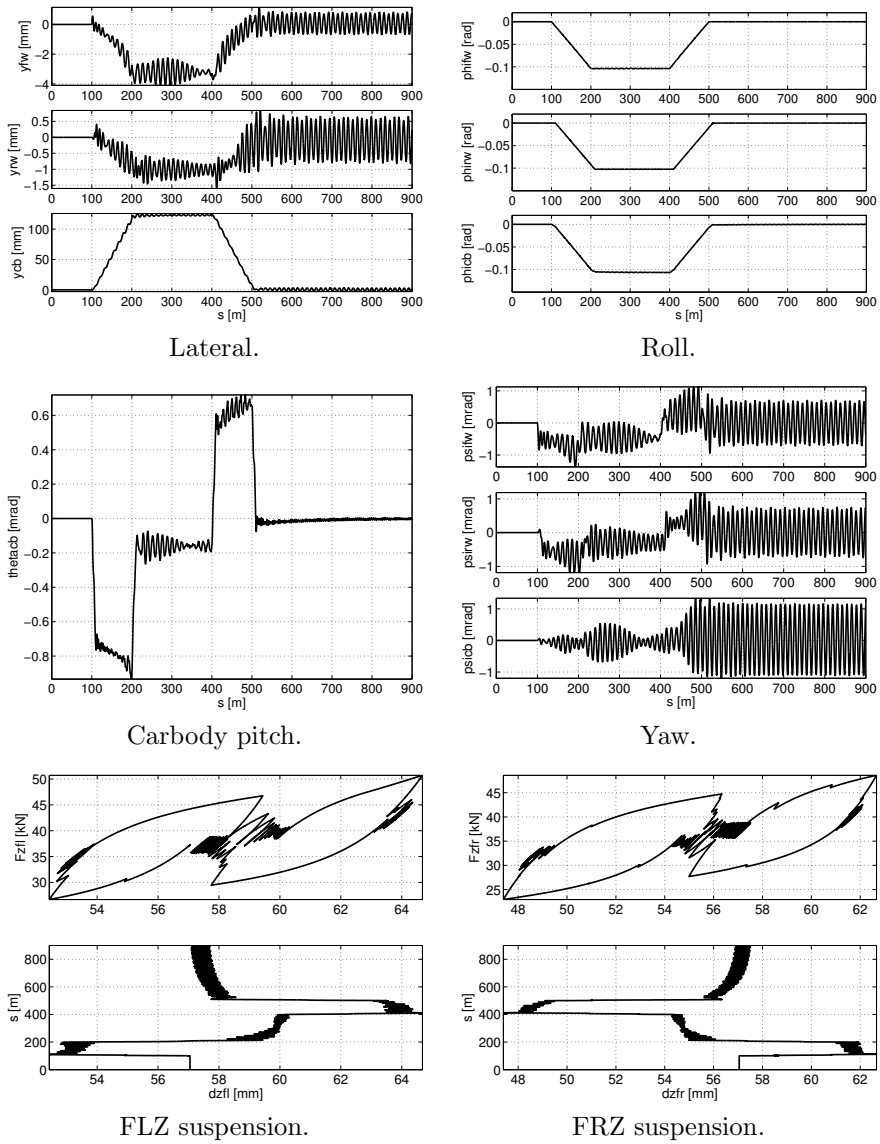

Figure 5.32: Hbbills 311 (empty, PTP, 1/40) running through a left hand curve at 20 m/s.

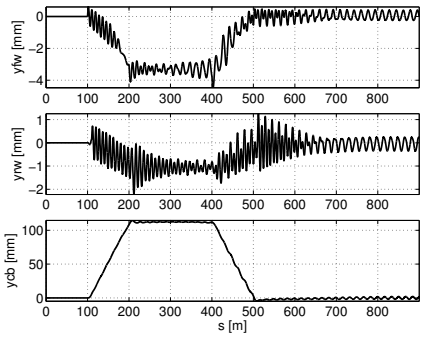

Lateral.

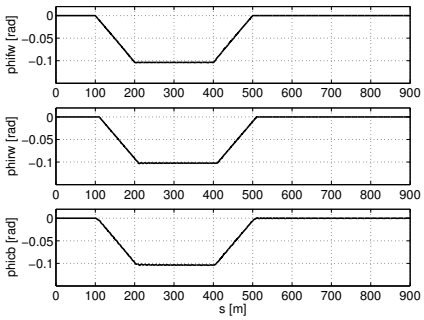

Roll.

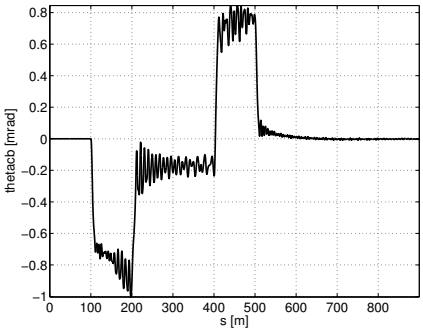

Carbody pitch.

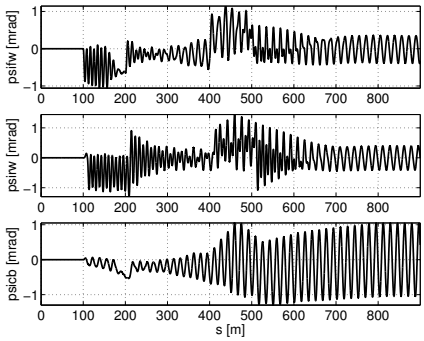

Yaw.

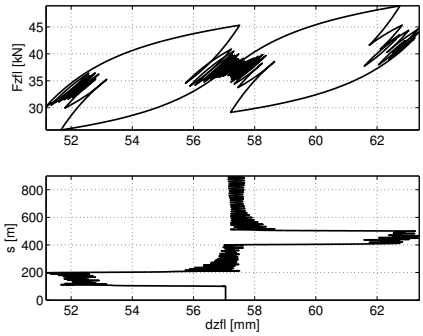

FLZ suspension.

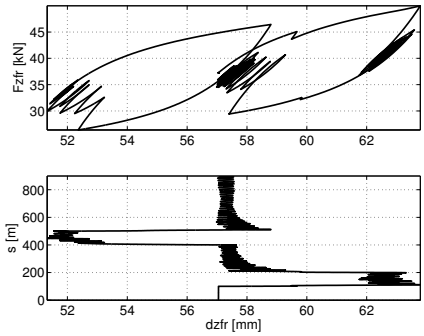

FRZ suspension.

Figure 5.33: Hbbills 311 (empty, PTP, 1/40) running through a left hand curve at 30 m/s.

5.4 Miscellaneous studies

In this section different aspects of the freight wagon model is investigated separately. In order to illustrate that the attractor in the centre of the track has a width as indicated by the bifurcation diagrams in Figure 5.1 to 5.3 let us consider the simulations in Figure 5.34 and 5.35. When all friction sliders in the suspension model are in their neutral positions then a motion will go towards the exact centre of the track. On the other hand, if the friction sliders are not in their neutral position, e.g. after a hunting motion, then the bodies will tend towards off–centred equilibrium positions.

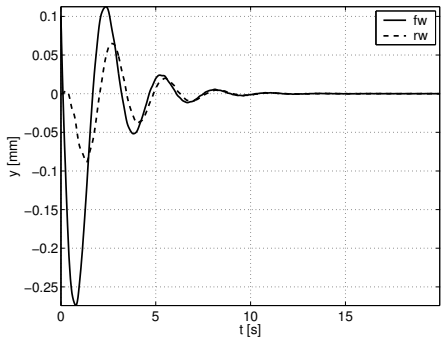

Figure 5.34: Friction sliders in neutral position. Kbps (empty, SPP, 1/30) at 10 m/s.

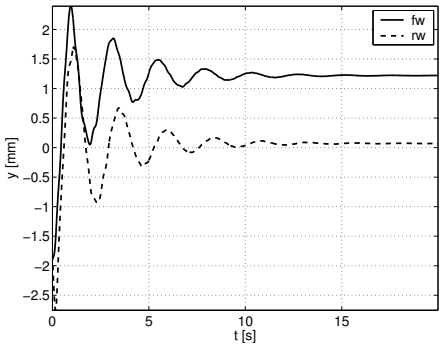

Figure 5.35: New equilibrium after returning from a hunting motion. Kbps (empty, SPP, 1/30) at 10 m/s.

The lateral suspension characteristics are illustrated by the simulation results presented in Figure 5.36 where the wagon is attracted to a flange–to–flange motion. The rolling phase and sliding phase that are characteristic for the UIC links are clearly visible. Moreover, the additional stiffness due to the interaction with the suspension bracket is also seen for displacements larger than 10 mm.

A simulation of an asymmetrically loaded wagon results in the suspension characteristics shown in Figure 5.37. The centre of mass is moved 10 cm longitudinally and laterally towards the front left suspension. It is seen that the working area for the vertical suspension is different from suspension to suspension. The left suspensions are deformed more than the right suspensions. This also influences the lateral suspension stiffnesses because the stiffness of a pendular suspension system depends on the load.

The longitudinal UIC links might exhibit a friction climbing phenomenon as illustrated in Figure 5.38 for the front left suspension. The top figure shows the hysteresis loop and the bottom figure depicts the evolution of the suspension deformation. The results are obtained from a simulation of the Kbps wagon that is attracted to a chaotic hunting motion at 50 m/s. Note how the equilibrium is shifted (about 5 mm) towards the leading guidance.

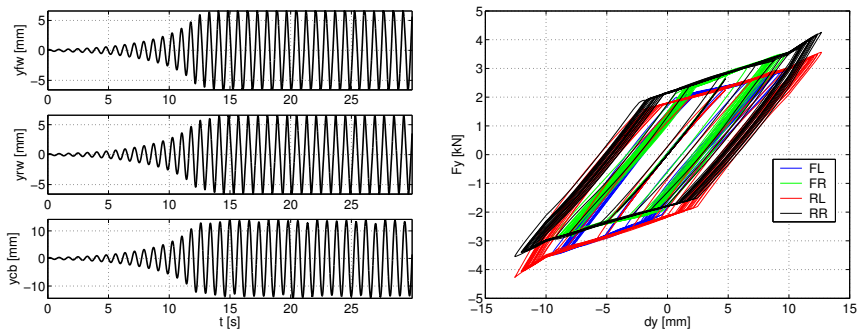

Figure 5.36: Illustrating the lateral suspension characteristics. Hbbills 311 (empty, PTP, 1/20) at 60 m/s.

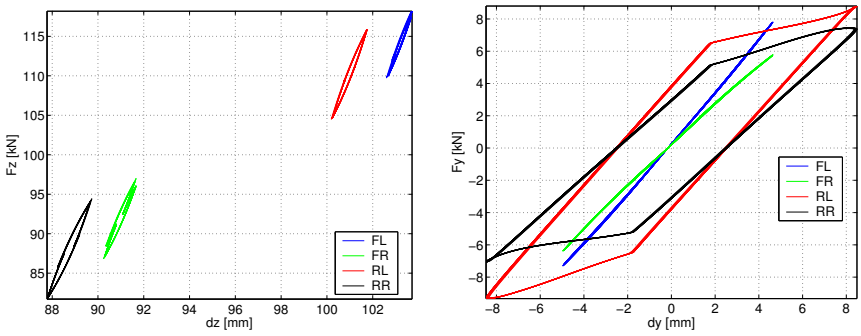

Figure 5.37: Illustrating the lateral and vertical suspension characteristics. Hbbills 311 (asym. loaded, PTP, 1/40) running at 15 m/s.

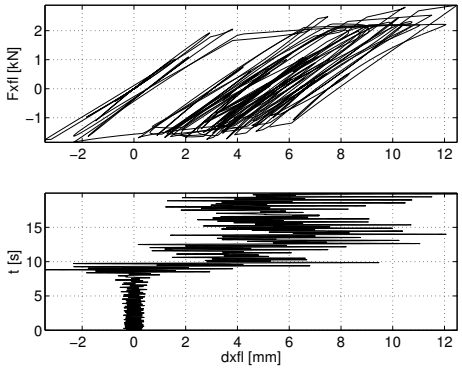

Figure 5.38: Friction climbing in the longitudinal suspension. Kbps (empty, SPP, 1/30) at 50 m/s.

The vertical suspension is most often only excited with a small amplitude around a deformation determined by the load from the carbody. To see how the leaf spring model actually works at larger amplitudes a simulation is made with the carbody pulled out from its vertical equilibrium. The vertical suspension characteristics of the front left suspension is shown in Figure 5.39. The additional leaf has been active before the carbody settles down on its equilibrium. The state changes in the four leaf spring models are illustrated by the event diagram in Figure 5.40. Each level of the signal represents a state, see Table 5.1. The AUTO state is used close to equilibrium since the model is approximately smooth here and no event detection is necessary. All models follow the state sequence:

$$1 \rightarrow 2 \rightarrow 3 \rightarrow 4 \rightarrow 1 \rightarrow 4 \rightarrow 0 \rightarrow 1 \rightarrow 4 \rightarrow 0$$

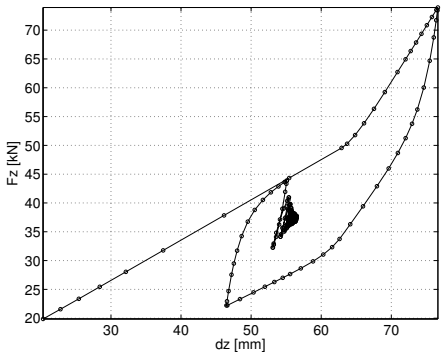

Figure 5.39: Carbody out of vertical equilibrium. Hbbills 311 (empty, SPP, 1/30) running at 20 m/s.

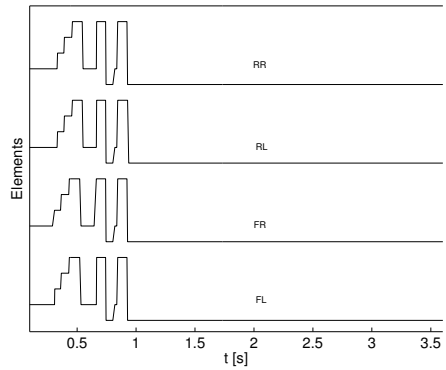

Figure 5.40: Event diagram for the four leaf spring models.

Level	State	Description
0	AUTO	Close to equilibrium
1	LoadingH	Loading main leaves only
2	LoadingHZ	Loading main leaves and additional leaf
3	UnloadingHZ	Unloading main leaves and additional leaf
4	UnloadingH	Unloading main leaves only

Table 5.1: Leaf spring states.

Even though the nonlinear model of the leaf spring is fundamentally different from that of a linear model, the dynamics were not found to be very sensitive to the linear/nonlinear modelling of the leaf spring. A comparison is given in Figure 5.41. Qualitatively, the results are similar and the positioning of the flange–to–flange attractor as well as the resonance hunting are the same.

The vertical suspension characteristics at 17 m/s are shown in Figure 5.42. The linear model has a clear discrepancy because both stiffness and damping of the leaf spring depend on the excitation amplitude and suspension load. It is possible to fit the linear parameters such that the nonlinear characteristics are more accurately resembled for a particular excitation, however, the discrepancy would reappear at any other excitation amplitude (or suspension load). It is expected that the nonlinear modelling is important in an analysis where vertical track irregularities are investigated.

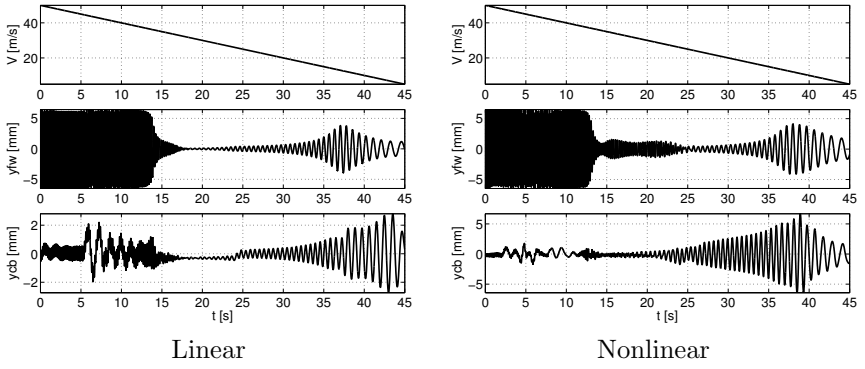

Figure 5.41: Comparing results obtained with a linear and nonlinear modelling of the leaf spring. Hbbills 311 (empty, PTP, 1/40).

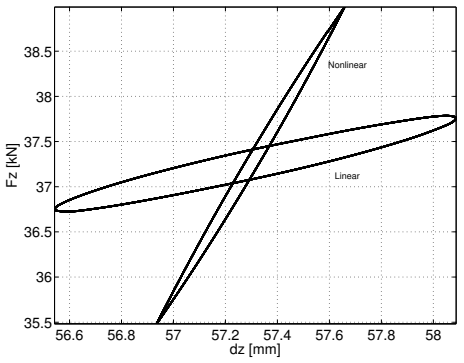

Figure 5.42: Comparing vertical suspension characteristics (front left suspension). Hbbills 311 (empty, PTP, 1/40) running at 17 m/s.

The flange–to–flange motion of the Hbbills 311 wagon has been analysed using the multibody software VOCOLIN developed at INRETS, France. Simulation results are shown in Figure 5.43. The wagon runs on a straight track having a shift of 8 mm after a distance of 20 m. The wagon starts out at 50 m/s and decelerates with 0.25 m/s^2. It is noted that the flange–to–flange motion stops at about 2000 m, which after some basic calculations is found to correspond to 38.7 m/s. After the flange–to–flange attractor disappears the motion falls down on a small amplitude attractor. The results obtained with VOCOLIN corresponds to the ones found with the model developed in this thesis, see Figure 5.9. It should be noted that VOCOLIN has been used in many simulations in which the simulation results have been verified in road tests of the real vehicle.

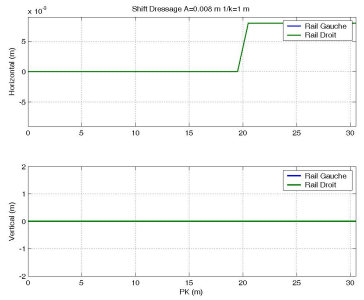

Track.

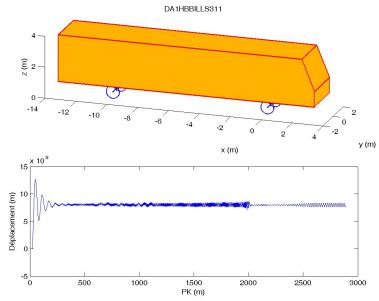

Carbody.

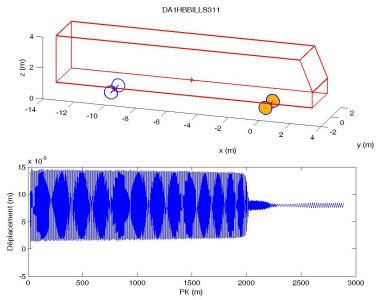

Front wheelset.

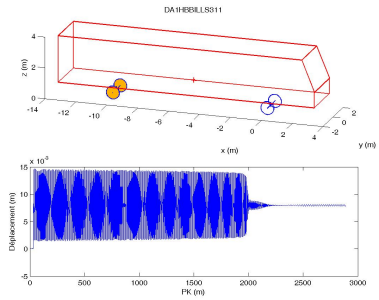

Rear wheelset.

Figure 5.43: Simulation using VOCOLIN. Hbbills 311 (empty, PTP, 1/40).

The discontinuous behaviour of the wheel–rail contact parameters is illustrated by the simulation shown below. The contact parameters are divided into continuous sections as illustrated for the contact angle in Figure 5.44. The wagon starts out close to the centre of the track but eventually ends up on a flange–to–flange attractor, see the time series in Figure 5.45. From the time series of the contact angle, Figure 5.46, it is shown how the contact angle jumps between the different sections. Double contact occurs in small regions around the points of discontinuity, and from the zoomed view in Figure 5.47 these situations are identified by the overlapping regions.

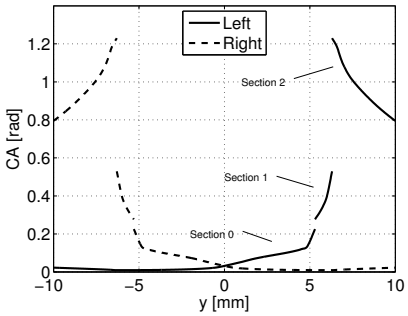

Figure 5.44: Contact angle, 1/40.

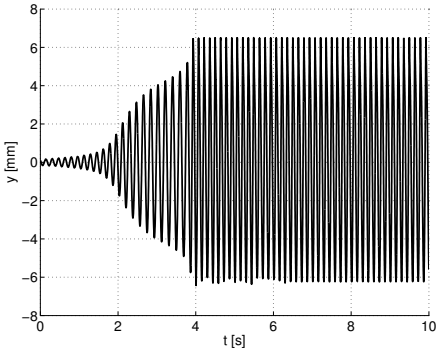

Figure 5.45: Time series of the front wheelset. Hbbills 311 (empty, PTP, 1/40) running at 50 m/s.

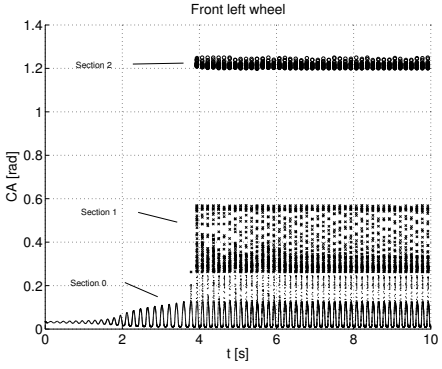

Figure 5.46: Time series of the contact angle. Hbbills 311 (empty, PTP, 1/40) at 50 m/s.

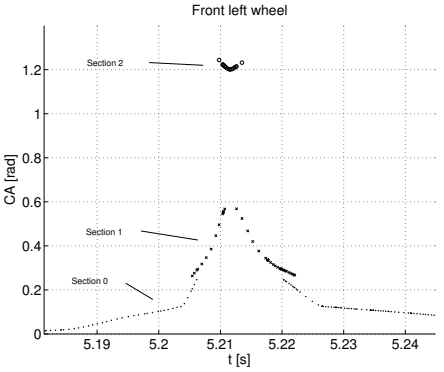

Figure 5.47: Zoomed view.

As described in section 2.2.3 each continuous section of the contact table is interpolated using cubic splines. Traditionally, a piecewise linear interpolating method is used to interpolate the contact table. Such a method, however, introduces a nonsmoothness into the system. This might cause a numerical integration scheme to be inaccurate and/or inefficient. The additional work in constructing the cubic splines (having smooth properties) was found to be very beneficial in the end. Consider the comparison between the two interpolating strategies shown in Figure 5.48 and 5.49 based on a simulation with the Hbbills 311 wagon running at 20 m/s in 20 simulation seconds. The motion of the wheelsets is periodic with a small amplitude. For the same error tolerance the cubic spline method uses only 29% of the steps taken by the piecewise linear method. Any qualitative difference in the simulated results obtained with the two interpolating strategies could not be found.

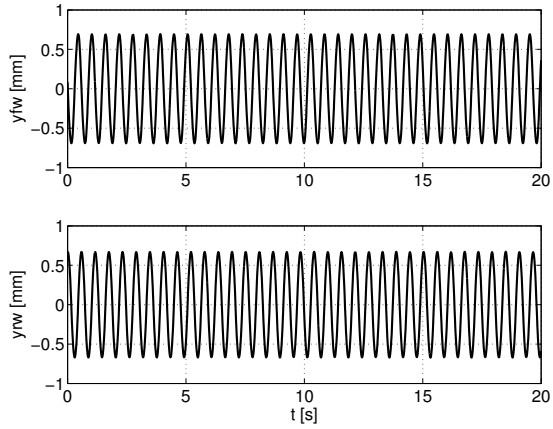

Figure 5.48: Hbbills 311 (empty, PTP, 1/40) running at 20 m/s in 20 s.

```
(CUBIC SPLINE METHOD)
steps = 5048(good) + 1011(bad) + 0(div) = 6059

(LINEAR METHOD)
steps = 17187(good) + 3755(bad) + 0(div) = 20942
```

Figure 5.49: Comparing contact table interpolation methods.

The wheel–rail contact table used in this thesis is generated using the program RSGEO [2]. From analyses of the dynamics of rail vehicles it is well known that the wheel–rail contact computations are a sensitive part of the model. The simulation of the Hbbills 311 wagon discussed previously (Figure 5.9) is compared with a simulation using the same model parameters except that the contact table is generated using the program WRKIN [104]. The comparison is shown in Figure 5.50. There is an obvious quantitative difference between the results. The flange–to–flange motion does not disappear at the same speed and the amplitude of the resonance motion is clearly less in the simulation with WRKIN. Differences are also observed in the computed contact angles obtained by the two programs.

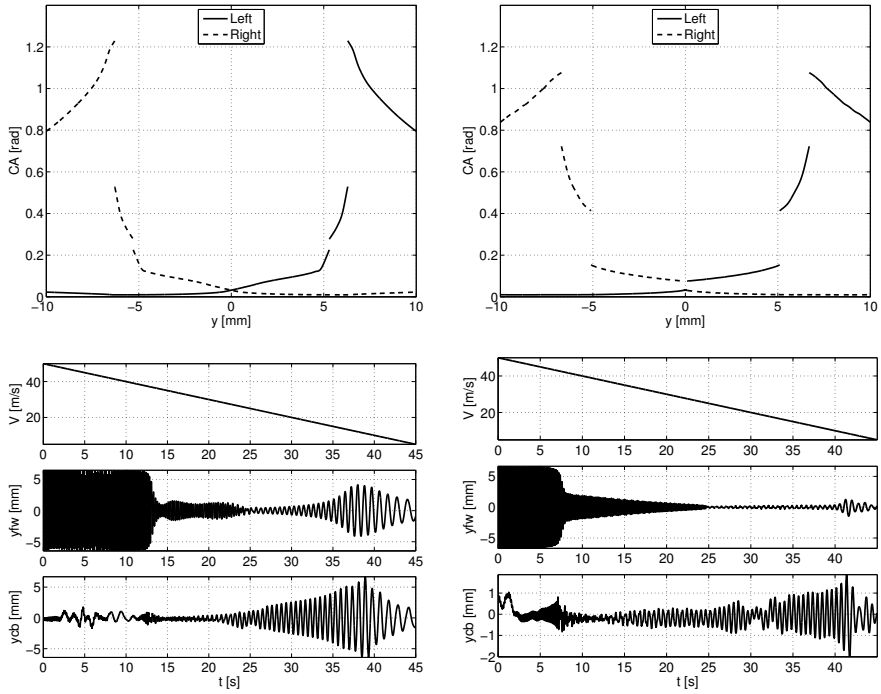

Figure 5.50: Influence of different contact tables. Hbbills 311 (empty, PTP, 1/40).

The longitudinal model of the axle guidance is seldom active in the idealised simulations considered in this thesis, i.e. straight track with no irregularities. To verify that it truly works in the entire freight wagon framework the simulation results presented in Figure 5.51 to 5.53 are made. The carbody of the Hbbills 311 wagon alone is given a deceleration of 5 m/s^2 from 45 m/s. This makes the wheelsets impact against their leading axle guidances as illustrated by Figure 5.52. The distance to the axle guidance is 22.5 mm. In the zoomed view, Figure 5.53, it is more clearly seen that the motion of the axle boxes are restricted by the 22.5 mm.

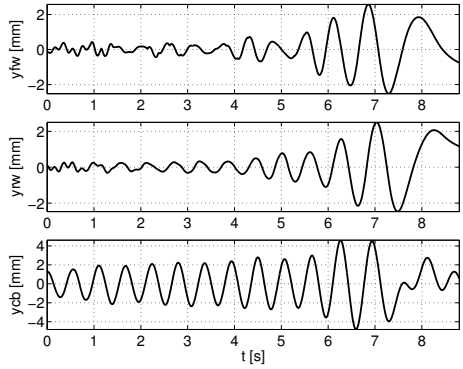

Figure 5.51: Hbbills 311 (empty, PTP, 1/40) decelerating with 5 m/s^2.

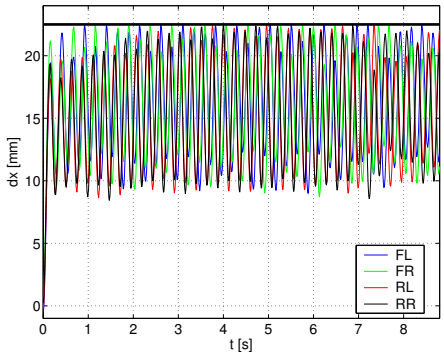

Figure 5.52: Time series of longitudinal suspension deformations.

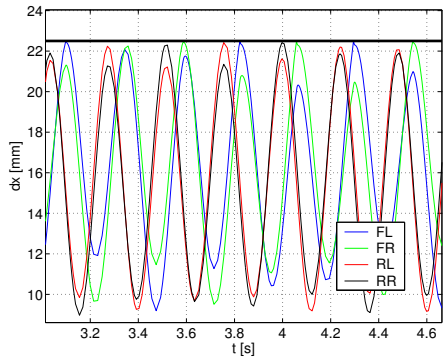

Figure 5.53: Zoomed view.

Chapter 6

Future work

Here are some suggestions for future work in relation to this project. This thesis mainly focuses on the fundamental running properties on straight track and less attention is put into the curving behaviour. A thorough analysis of the running properties in curves is of course very important. It could also be interesting to investigate the model in a scenario where measured track irregularities are taken into account. On a real track the motion of the wagon is always a transient because track irregularities (and other imperfections) prevent the wagon to settle down on one of the attractors. Transients in nonlinear systems with multiple attractors and chaotic dynamics can be severe and therefore such a study is wanted. Track forces and carbody accelerations are central quantities in the acceptance of rail vehicles according to international standards. It would be highly recommendable to include such an analysis in the simulation output.

Chapter 7

Conclusion

A mathematical model of the European two–axle freight wagon is presented and analysed in this thesis. The model is primarily used to investigate the running properties on straight track of different types of wagons. The interacting forces in the system are all nonsmooth being a consequence of the dry friction, clearances and the geometry between the wheel and rail. An effort is invested into the numerical integration of the system of differential equations. A consistent and accurate method is achieved by the application of an implicit Runge–Kutta method of order 3 linked with an event location routine that deals with the nonsmoothness of the model in an appropriate manner. The model is characterised by:

- Rigid body model with 17 DOF having two rails (fixed), two wheelsets and one carbody. The DOF of the wheelsets are: longitudinal, lateral, vertical, roll, yaw and spin perturbation. The DOF of the carbody are: lateral, vertical, roll, pitch, yaw. The longitudinal DOF of the carbody is constrained to move with a prescribed speed (or acceleration). The curvilinear track model from [5] is implemented. The track is assumed to be perfect without irregularities.

- The wheel–rail contact is based on the European standard wheel–rail profiles S1002/UIC60. Different rail inclinations have been analysed. The wheel–rail contact geometry is tabulated prior to simulation assuming that the yaw angle can be neglected. During the simulation, the current geometry is found by interpolation in the contact table using cubic splines. The normal force is computed using an elastic approach (Hertzian spring),

and the tangential contact forces are found by Shen–Hedrick–Elkins model [78].

- A general model able to simulate the suspension characteristics from a trapezoidal as well as parabolic leaf spring is developed. It is based on the work by Fancher *et al* [14]. The dry friction between the leaves is responsible for the fact that the damping and effective spring rate both depend on the excitation amplitude and suspension load. This special behaviour that cannot be linearised is taken into account in the nonlinear model developed.

- The UIC double–link connection is simulated by Piotrowski's model [61]. The model incorporates the nonsmooth behaviour of the rolling/sliding transitions in the links as well as the load dependent suspension characteristics. Moreover, a dead band spring models the effect of the clearance between the lower link and the suspension bracket.

- The lateral axle guidance is modelled using a unilateral dead band spring model, and the longitudinal axle guidance is modelled by Newton's impact law (in the LCP formulation from [60]).

- All nonsmooth models are implemented in state dependent formulations dividing the characteristics into smooth submodels.

The rail inclination has an important influence on the qualitative running properties of the two–axle freight wagon on straight track. This is due to a resonance motion of the wagon. The resonance occurs because the lateral excitation frequency of the wheelsets coincide with the yaw eigenfrequency of the carbody. Since the rail inclination influences the lateral excitation frequency of the wheelsets it implicitly determines the speed for which the resonance motion occurs. The running properties of the wagon are observed to be undercritical for 1/20 rail inclination (resonance speed at 176 km/h) and overcritical for 1/40 rail inclination (resonance speed at 43 km/h). Overcritical running properties are not the same as bad running properties. Actually, the overcritical running properties can be quite good in the operating speed range ($60 - 120$ km/h), because the only existing attractor has a small amplitude. The behaviour for 1/30 rail inclination gave a scenario somewhere in between the undercritical and overcritical. Even though the stationary solution is stable within the operating speed range, there is a potential bad running behaviour for a large speed range in the 1/30 rail inclination case because a medium amplitude attractor exists. At high speeds the wheelsets might get attracted to a flange–to–flange motion. This is observed for all rail inclinations, however, it is most severe in the 1/20 rail inclination case because the wheelsets excite the yaw eigenmode of the carbody. The yaw eigenfrequency of the carbody depends on the yaw moment of inertia of the carbody but the parameter is not found sensitive w.r.t. the resonance behaviour.

The two–axle freight wagon does not have a well defined stationary motion due to a rolling/sliding effect in the suspension links. An example of an off–centred solution is given. It is also observed that the dry friction might be responsible for a friction climbing phenomenon in the longitudinal suspension where the axle box progressively moves closer to the axle guidance.

Despite several fundamental differences between a linear and nonlinear model of the leaf spring, the running properties on straight track are not found very sensitive to the model of the leaf spring being linear or nonlinear.

The medium amplitude attractor in the 1/30 rail inclination case is investigated in some detail. It is illustrated how the attractor bifurcates from periodic to chaotic dynamics. The chaotic motion has two variants: 1) Chaotic motion imposed on top of a periodic motion having small variations in amplitude. 2) Chaotic motion with a very irregular pattern. Both of them occur at high speed (above 122 km/h).

In summary, the bad running properties of European two–axle freight wagons have two variants: a resonance motion and a flange–to–flange motion. The rail inclination has a strong influence on the resonance speed which should be outside the operating speed range for satisfying running behaviour. Too much friction in the suspension links leads to a more violent resonance motion. The flange–to–flange motion is moved to higher speeds when: the wheelbase is longer, the horizontal suspension is stiffer, the wagon is loaded. For instance, the empty Hbbills 311 wagon (long wheelbase, 1/40 rail inclination) has a flange–to–flange motion for speeds higher than 140 km/h, and if the wagon is loaded and the centre of gravity is not too high the running properties are satisfactory until 210 km/h. In contrast, the flange–to–flange motion for the empty G69 wagon (short wheelbase, 1/40 rail inclination) exists for speeds higher than 80 km/h.

Appendix A

Notation and symbols

Throughout the thesis the following notation is applied.

- Matrices and vectors are written in bold font, e.g. $\mathbf{x}, \mathbf{A}$.
- The reference base of a given vector appears from the preceding text.
- The time derivate is written by a dot, e.g. $\dot{\mathbf{x}}$.
- The Jacobi matrix, $\partial\mathbf{f}/\partial\mathbf{y}$, of the function $\mathbf{f}(\mathbf{y})$ is written in short by $\boldsymbol{\nabla}\mathbf{f}$.
- The notation $\mathbf{x} \geq \mathbf{0}$ denotes that all components of $\mathbf{x}$ are nonnegative.
- The matrix $\tilde{\mathbf{x}}$ is the skew–sym. operator expressing the crossproduct $\mathbf{x}\times$.
- Changing base of a vector is done using the rotation matrices. For instance, a vector $\mathbf{x}$ defined in the track base can be expressed in the inertial base by $\mathbf{A}_{OT}\mathbf{x}$.

See Table A.1 to A.6 for an overview of the abbreviations and symbols used.

ASZ	Parameter set for the UIC links (see Table 2.4 and 2.5)
CONTACT	Program developed by Kalker [39] for solving contact problems
DAE	Differential–algebraic equations
DOF	Degrees of freedom
GUI	Graphical user interface
INP	Parameter set for the UIC links (see Table 2.4 and 2.5)
IVP	Initial value problem
JNI	Java native interface
LCP	Linear complementarity problem
MP	Parameter set for the UIC links (see Table 2.4 and 2.5)
ODE	Ordinary differential equations
PTP	Parameter set for the UIC links (see Table 2.4 and 2.5)
RSGEO	Wheel–rail contact geometry program [2]
S1002	Standard wheel profile
SPP	Parameter set for the UIC links (see Table 2.4 and 2.5)
ESDIRK	Explicit singly diagonal implicit Runge–Kutta
TAFWA	Two–axle freight wagon analyser
UIC	Union internationale des chemins de fer
UIC60	Standard rail profile
VOCOLIN	VOitures en COurbes, Logiciel INrets
WRKIN	Wheel–rail contact geometry program [104]

Table A.1: Abbreviations.

$\mathbf{A}_{OT}$	Rotation matrix changing track coordinates to inertial coordinates
$\mathbf{A}_{TO}$	Rotation matrix changing inertial coordinates to track coordinates
$\mathbf{A}_{Tb}$	Rotation matrix changing body coordinates to track coordinates
$\mathbf{A}_{bT}$	Rotation matrix changing track coordinates to body coordinates
$\mathbf{A}_{bc}$	Rotation matrix changing contact coordinates to body coordinates
$\mathbf{A}_{cb}$	Rotation matrix changing body coordinates to contact coordinates
$\mathbf{A}_{TiTj}$	Rotation matrix changing track coordinates related the j'th body to track coordinates related the i'th body
$\mathbf{A}_{Tc}$	Rotation matrix changing contact coordinates to track coordinates
$\mathbf{A}_{x}^{(\alpha)}$	Rotation matrix. Around axis x with the angle α
$\mathbf{A}_{y}^{(\alpha)}$	Rotation matrix. Around axis y with the angle α
$\mathbf{A}_{z}^{(\alpha)}$	Rotation matrix. Around axis z with the angle α
$\mathbf{a}$	Acceleration vector
a	Longitudinal semi–axis in the contact ellipse
b	Lateral semi–axis in the contact ellipse
b_0	Half distance between the nominal rolling circles of the wheels
b_i	Runge–Kutta weights
$\bar{b}_i(\theta)$	Continuous extension weights
$\mathbb{C}$	Complex numbers
c_i	Runge–Kutta nodes
c_h, c_z	Leaf spring stiffnesses
C_{11}, C_{22}, C_{23}	Kalker's creepage coefficients
$\mathcal{D}$	Stability region
D_x	Generalised coordinate (longitudinal)
D_y	Generalised coordinate (lateral)
D_z	Generalised coordinate (vertical)
D_ϕ	Generalised coordinate (roll)
D_θ	Generalised coordinate (pitch)
D_ψ	Generalised coordinate (yaw)
D_β	Spin coordinate, $D_\beta = \dot{D}_\theta$
E	Young's modulus
$\mathbf{F}_c$	Wheel–rail contact force
$\mathbf{F}_g$	Gravitational force
$\mathbf{F}_{sl}$	Suspension force on left axle box
$\mathbf{F}_{sr}$	Suspension force on right axle box
$\mathbf{F}_{sfl}$	Suspension force at the front left position on the carbody
$\mathbf{F}_{sfr}$	Suspension force at the front right position on the carbody
$\mathbf{F}_{srl}$	Suspension force at the rear left position on the carbody
$\mathbf{F}_{srr}$	Suspension force at the rear right position on the carbody
$\mathbf{F}_{\text{ext}}$	External forces
F_r	Residual spring force
F_{tol}	Force quantifying close to equilibrium in the leaf spring model
F_{env}	Envelope function related to the modelling of the leaf spring
$\tilde{F}_x$, $\tilde{F}_y$	Creep forces according to Kalker's linear theory
$\lvert\tilde{\mathbf{F}}\rvert$	Magnitude of the creep force according to Kalker's linear theory
$\lvert\mathbf{F}\rvert$	Magnitude of the creep force according to Shen–Hedrick–Elkins' model
F_{motor}	External force in the measurements on the UIC suspension
F_{gl}	Force from the axle guidance in the lateral direction
F_{sb}	Force from the dead band spring modelling the interaction between the UIC links and the suspension bracket

Table A.2: Latin symbols (a to f).

G	Shear modulus
g_i	State transition function, event function
g_{Ni}	Constraint functions in the model of the axle guidance in the longitudinal direction
h	Stepsize in the numerical integration
h_j	Spline node spacing
$\mathbf{h}(\mathbf{q}, \dot{\mathbf{q}})$	Vector containing gyroscopical accelerations and all active forces and torques
$\mathbf{I}$	Identity matrix
$\mathbf{I}_s$	Inertia tensor
I_G	Set defining the possible contact points between the axle box and axle guidance in the longitudinal direction
I_S	Set of active constraint functions in the model of the axle guidance in the longitudinal direction
I_{xx}, I_{yy}, I_{zz}	Roll, pitch and yaw moment of inertia
$\mathbf{i}, \mathbf{j}, \mathbf{k}$	Base of the inertial coordinate system
$\mathbf{i}_T, \mathbf{j}_T, \mathbf{k}_T$	Base of the track coordinate system
$\mathbf{i}_b, \mathbf{j}_b, \mathbf{k}_b$	Base of the body coordinate system
$\mathbf{i}_c, \mathbf{j}_c, \mathbf{k}_c$	Base of the contact coordinate system
$\mathbf{J}$	Jacobi matrix used in expressing the absolute coordinates in terms of the generalised coordinates
$\tilde{\mathbf{j}}$	Vector holding additional terms in expressing the absolute velocities in terms of the generalised velocities
$\bar{\mathbf{j}}$	Vector holding additional terms in expressing the absolute accelerations in terms of the generalised accelerations
k, k_1	Spring stiffnesses
$\mathbf{k}_i$	Runge–Kutta stage derivatives
k_x	Pendular stiffness related to the modelling of the UIC links in the longitudinal direction
k_y	Pendular stiffness related to the modelling of the UIC links in the lateral direction
k_{ix}	Serial stiffness in the i'th elastic dry friction element related to the modelling of the UIC links in the longitudinal direction
k_{iy}	Serial stiffness in the i'th elastic dry friction element related to the modelling of the UIC links in the lateral direction
k_{gl}	Stiffness of the axle guidance in the lateral direction
k_{sb}	Stiffness of the dead band spring modelling the interaction with the UIC links and the suspension bracket
$\mathbf{L}$	Angular momentum
$\bar{\mathbf{M}}$	Mass matrix
$\mathbf{M}$	Mass matrix (projected form)
$\mathbf{M}_{\text{ext}}$	External torques
m_{cb}	Carbody mass
m_w	Wheelset mass
N	Normal force between the wheel and rail
n_c	Number of wheel–rail contact points
O	Origin of the inertial coordinate system
O_T	Origin of the track coordinate system
O_b	Origin of the body coordinate system
O_c	Origin of the contact coordinate system

Table A.3: Latin symbols (g to o).

P_i	Point on the i'th body
P_j	Point on the j'th body
P_y	Restoring force from the technical pendulum / UIC suspension
$P_{i1}^k(s)$	Polynomial used in expressing the curve parameters $1/\rho_h(s)$, $1/\rho_v(s)$ as functions of the track curvatures at the node points of the i'th track stage
$P_{i2}^k(s)$	Polynomial used in expressing the curve parameters $\beta_C(s)$, $\theta_C(s)$ as functions of the track curvatures at the node points of the i'th track stage
$P_{i3}^k(s)$	Polynomial used in expressing the curve parameters $T_h(s)$, $T_v(s)$ as functions of the track curvatures at the node points of the i'th track stage
$\mathbf{p}$	Linear momentum
$\mathbf{q}$	Generalised coordinates
q_{pen}	Penetration depth of the wheel into the rail
$\dot{\mathbf{q}}_A$	Generalised velocity before impact
$\dot{\mathbf{q}}_E$	Generalised velocity after impact
$\mathbb{R}$	Real numbers
$R(z)$	Rational function related to the stability of Runge–Kutta methods
R_O	Inertial coordinate system
R_T	Track coordinate system
R_b	Body coordinate system
R_c	Contact coordinate system
$\mathbf{R}_{\text{pen}}$	A vector from the contact point on the wheel to the contact point on the rail
$\mathbf{R}_R$	Vector defining the contact point on the rail
$\mathbf{R}_w$	Vector defining the contact point on the wheel
$\Delta\mathbf{r}$	Vector defining the deformation between P_i and P_j
r_0	Nominal rolling radius of the wheel
r_i	Curvature at s_i
$\mathbf{r}_{ij}$	Vector between P_i and P_j
s	Curvilinear abscissa
s_i	The position along the curvilinear abscissa where the i'th track stage begins
s_j	Parameter value at the j'th spline node
s_j''	Second derivative of the spline at the j'th node
t	Time, spline parameter
T_0	Break out force for a dry friction slider
T_i	Force from the i'th elastic element with dry friction
T_h, T_v	Auxiliary functions (defined in section 2.1.4)
ΔT_v	Adjustment to the auxiliary function in the vertical direction in modelling the track cant
T_x, T_y	Creep forces according to Shen–Hedrick–Elkins' model
V	Speed of track system, vehicle speed along the track
v_s	Relative velocity between the sliding elements
$\mathbf{v}$	Velocity vector
$\mathbf{v}_{\text{con}}$	Relative velocity between the wheel and rail

Table A.4: Latin symbols (p to v).

δW	Virtual power
$\mathbf{w}_{Ni}$	Generalised normal force direction for the i'th contact in the model of the axle guidance in the longitudinal direction
$\mathbf{W}_N$	Matrix of generalised normal force directions in the model of the axle guidance in the longitudinal direction
$\delta\mathbf{x}$	Virtual displacement of the vector $\mathbf{x}$
x_0	Longitudinal clearance between axle box and axle guidance
x_{OTj}	Longitudinal distance from i'th to j'th track system
x_j	Spline nodes
x_i, y_i, z_i	Coordinates of the centre of mass of the i'th body
x_{Pw}, y_{Pw}, z_{Pw}	Coordinates of the suspension attachment point on the wheelset
x_{Pcb}, y_{Pcb}, z_{Pcb}	Coordinates of the suspension attachment point on the carbody
y_{01}	Lateral clearance between suspension UIC links and suspension bracket
y_{02}	Lateral clearance between axle box and axle guidance
$y_{i,lo}$, $y_{i,hi}$	Boundary points of the i'th wheel–rail state
$\bar{y}_i$	Lateral equilibrium position of the centre of mass of the i'th body
$\mathbf{y}_c$	Continuous extension
$\mathbf{y}_n$	The n'th numerical solution point
$\bar{z}_i$	Vertical equilibrium position of the centre of mass of the i'th body
z_0	Position of the additional leaf

Table A.5: Latin symbols (w to z).

$\boldsymbol{\alpha}$	Angular acceleration vector
β	Decay constant related to the leaf spring model
β_C	Track yaw
Γ	Acceleration of track system
δ	Contact angle, leaf spring deflection
ϵ	Adjustment factor in Shen–Hedrick–Elkins' model
$\boldsymbol{\epsilon}_N$	Diagonal matrix containing the coefficients of restitution in the model of the axle guidance in the longitudinal direction
η	Measured acceleration
θ_C	Track gradient
θ	Pitch angle, continuous extension parameter
$\boldsymbol{\Lambda}_N$	Impact impulses in the model of the axle guidance in the longitudinal direction
μ	Friction coefficient between the wheel and rail
μ_0	Friction parameter related to the leaf spring model
ν	Poisson's ratio
$\dot{\nu}$	Spin perturbation
ξ_x	Longitudinal creep
ξ_y	Lateral creep
ξ_s	Spin creep
$1/\rho_h$	Horizontal track curvature
$1/\rho_v$	Vertical track curvature
ϕ	Roll angle, sway angle in the technical pendulum
ϕ_{SE}	Track superelevation
ψ	Yaw angle
$\boldsymbol{\Omega}$	Angular velocity of wheelset, carbody
$\boldsymbol{\Omega}_T$	Angular velocity of track system
$\boldsymbol{\Omega}_b$	Angular velocity of body system

Table A.6: Greek symbols.

Appendix B

Examples

The purpose of the examples presented here is to illustrate some of the key issues in the modelling of the two–axle freight wagon, i.e. the elastic dry friction element, dead band spring, nonlinear leaf spring and multiple impacts. The models have few DOF such that the modelling aspects will appear clearly.

B.1 Impact oscillator

The classical impact oscillator with a suspended mass impacting against a motion delimiter is investigated. The mass is assumed to be suspended by a system similar to the UIC links. The single DOF model is illustrated in Figure B.1. The friction slider is assumed to obey Coulomb's friction law. There are three reasons why this is a nonsmooth dynamical system: 1) The force from the elastic dry friction element is nonsmooth due to the stick–slip transitions of the dry friction slider. 2) The dead band spring has a nonsmooth force characteristic because of the instants were the dead band clearance is exceeded. 3) The effect of the wall is a sudden change in the moving direction of the mass, i.e. a discontinuity in the velocity coordinate.

Using Newton's second law it is seen that the dynamic motion is governed by

$$m\ddot{x} = -kx + F_1 + F_2 + F(t) \qquad x < x_d \quad , \quad t \geq 0 \tag{B.1}$$

The external force is harmonic, $F(t) = A\cos(\omega t)$. The force from the elastic dry friction element, F_1, is determined from the differential equation in equation (B.2) along with the state machine found in Figure B.2. The formulation

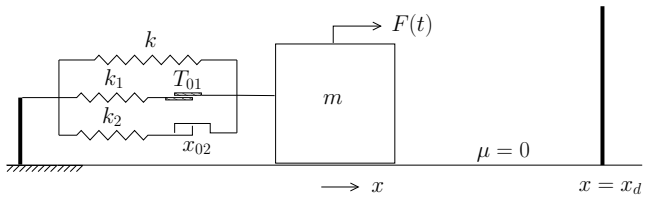

Figure B.1: The impact oscillator.

is found convenient because it does not require any tracing of the actual sliding distance of the dry friction slider. In the sticking state the element works as a linear spring and in the sliding phase the force is constant. The equilibrium of the spring changes each time the dry friction slider sticks at a new position. The force from the dead band spring, F_2, is found from equation (B.3) and the state machine in Figure B.3.

$$\dot{F}_1 = \begin{cases} -k_1\dot{x} & \text{Stick} \\ 0 & \text{SlidePos/SlideNeg} \end{cases} \tag{B.2}$$

$$F_2 = \begin{cases} 0 & \text{Idle} \\ -k_2(x - x_{02}) & \text{SpringPos} \\ -k_2(x + x_{02}) & \text{SpringNeg} \end{cases} \tag{B.3}$$

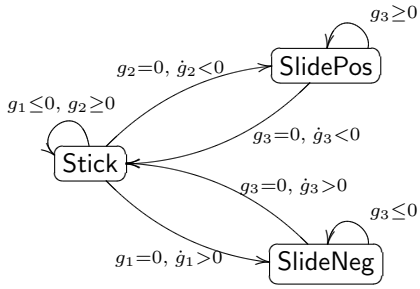

Figure B.2: Dry friction element.

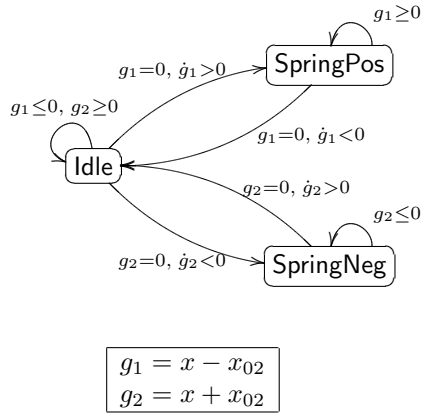

Figure B.3: Dead band spring.

The wall at $x = x_d$ is incorporated using Newton's impact law, $\dot{x}^+ = -\epsilon\dot{x}^-$. The state machine is illustrated in Figure B.4. After an impact it is necessary to perform a consistency check of the dry friction element, see Algorithm 3.

The necessity of this can be illustrated by a situation where the mass is moving towards the wall. Assume that the state of the elastic dry friction element is SlidePos prior the impact. After the impact the mass will be moving away from the wall and hence the state can no longer be SlidePos. Instead the state should be Stick because the velocity is reversed.

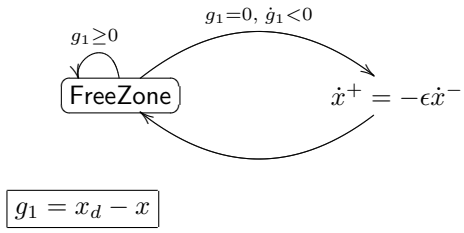

Figure B.4: Wall.

if IMPACT **then**
  if (SlidePos $\wedge$ $\dot{x}^+ < 0$) $\vee$ (SlideNeg $\wedge$ $\dot{x}^+ > 0$) **then**
    State of elastic dry friction element $\leftarrow$ Stick
  end if
end if

Algorithm 3: Consistency check.

The state transitions are all located during the simulation using an event system.

For the numerical simulation presented next, the parameters are set to: $m = 1000$ kg, $Q = 40000$ N, $k/Q = 4\ \mathrm{m}^{-1}$, $k_1/Q = 10\ \mathrm{m}^{-1}$, $k_2/Q = 2\ \mathrm{m}^{-1}$, $T_{01}/Q = 0.08$, $x_{02} = 0.015$ m, $x_d = 0.020$ m, $A = 10$ kN, $\omega = 3\pi$ and $\epsilon = 0.9$. The quantity Q represents an external load influencing the suspension parameters. The initial condition is $x(0) = \dot{x}(0) = F_1(0) = 0$. The time history of the simulation is shown in Figure B.5 and B.6. It is seen that the wall is clearly restricting the motion. The hysteresis loop and phase plot of the asymptotic solution shown in Figure B.7 and B.8 also emphasise the nonsmooth properties of the system.

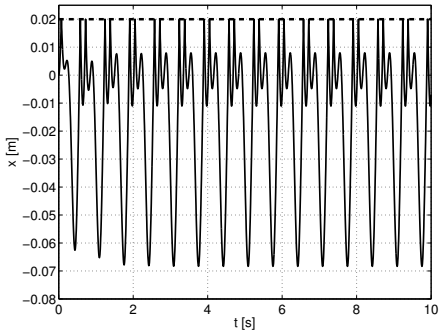

Figure B.5: Displacement history.

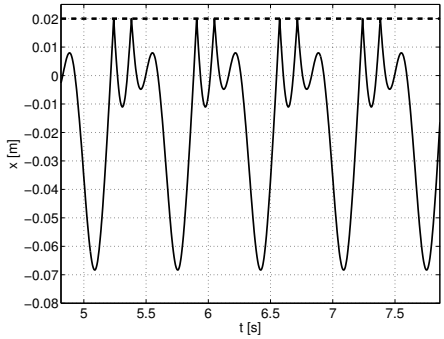

Figure B.6: Zoomed view.

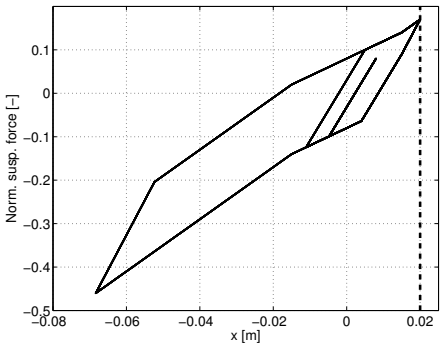

Figure B.7: Hysteresis loop.

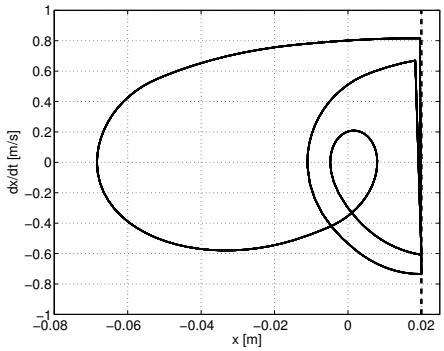

Figure B.8: Phase plot.

B.2 Leaf spring

Modelling a leaf spring is challenging because of its dry friction damping. The model presented here can simulate the characteristic hysteresis loop from trapezoidal leaf springs and two–stage parabolic leaf springs. These two leaf spring types are illustrated in Figure B.9 and B.10.

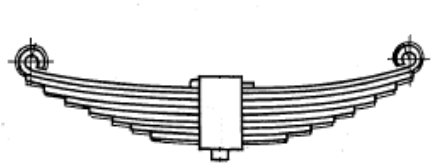

Figure B.9: Trapezoidal.

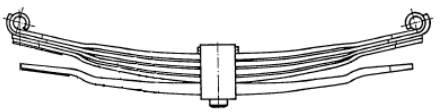

Figure B.10: Two–stage parabolic.

The restoring force is found by integrating the differential equation in equation B.4. The derivation of this equation is inspired by the work in [7, 14].

$$\dot{F} = \frac{\dot{z}}{\beta} \begin{cases} c_h z - F + c_h \mu_0 z + F_r & \text{LoadingH} \\ c_z(z - z_*) - F + c_z \mu_0 (z - z_*) + F_r & \text{LoadingHZ} \\ -(c_z(z - z_*) - F) + c_z \mu_0 (z - z_*) + F_r & \text{UnloadingHZ} \\ -(c_h z - F) + c_h \mu_0 z + F_r & \text{UnloadingH} \end{cases} \tag{B.4}$$

where z is the suspension deformation, c_h, c_z are spring stiffnesses, F_r is the residual spring force, β is a decay constant, μ_0 is a friction parameter, z_0 is the distance to the additional leaf, and $z_* = (1 - c_h/c_z)z_0$. At the switching boundary between two states, the new state is determined using the state machine in Figure B.12. To speed up the numerical integration, equation (B.4) is normalised with the static spring load. Furthermore, it can be utilised that close to equilibrium the loading/unloading transitions are approximately smooth. This is a consequence of the fact that the following condition

$$\begin{aligned} c_h z - F &\approx 0 \qquad z \le z_0 \quad , \quad |\dot{z}| \ll 1 \\ c_z(z - z_*) - F &\approx 0 \qquad z \ge z_0 \quad , \quad |\dot{z}| \ll 1 \end{aligned}$$

is satisfied close to equilibrium. Hence, near the equilibrium it is not necessary to locate the loading/unloading transitions.

The model presented can be used for modelling a trapezoidal leaf spring and a two–stage parabolic leaf spring. The main difference between these two types is the amount of dry friction damping and the interaction with the additional leaf. The parabolic leaf spring has an additional spacing between the leaves eventually providing less damping compared to the trapezoidal leaf spring.

The model can be illustrated by simulating a single mass suspended on a leaf spring, see Figure B.11. The model parameters are given in Table B.1 and the

results are presented in Figure B.13 to B.16. Note the characteristic hysteresis loop and how the model properly integrates past the corner. It is also seen that the event location is only performed far from equilibrium.

	Trapezoidal	Two–stage parabolic
β	3.0 mm	2.0 mm
μ_0	0.10	0.075
c_h	1.1 MN/m	0.65 MN/m
c_z	1.1 MN/m	1.82 MN/m
F_r	7 kN	7 kN
z_0	∞	62.9 mm

Table B.1: Parameters.

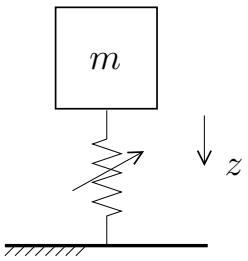

Figure B.11: Mass on leaf spring.

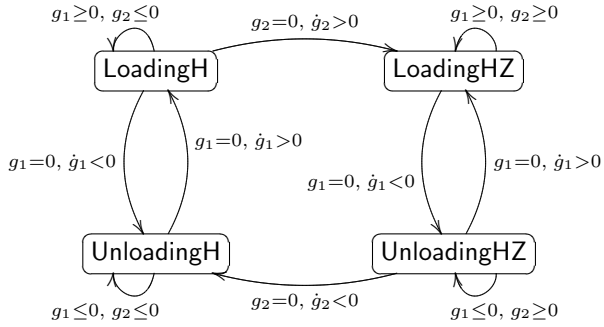

$$\begin{aligned} g_1 &= \dot{z} \\ g_2 &= z - z_0 \end{aligned}$$

Figure B.12: State machine of the leaf spring model.

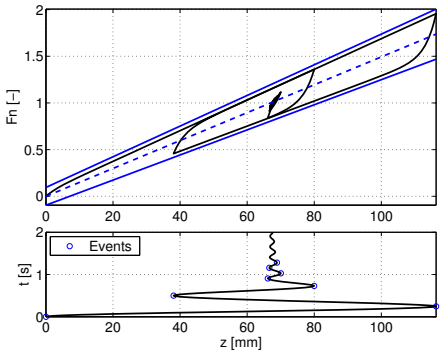

Figure B.13: Trapezoidal, $m = 7500$ kg.

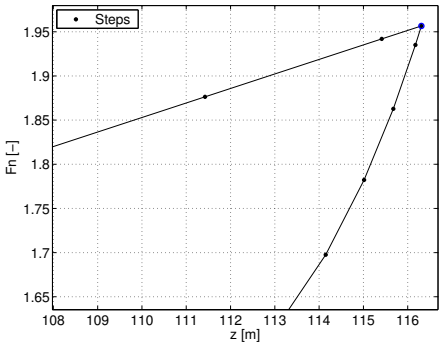

Figure B.14: Integrating the corner.

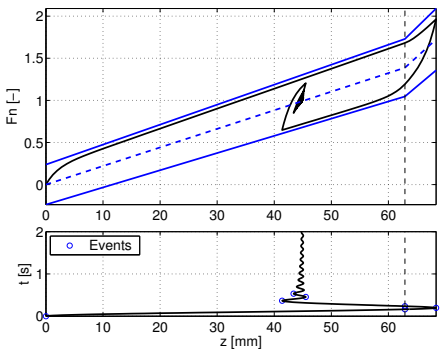

Figure B.15: Parabolic, $m = 3000$ kg.

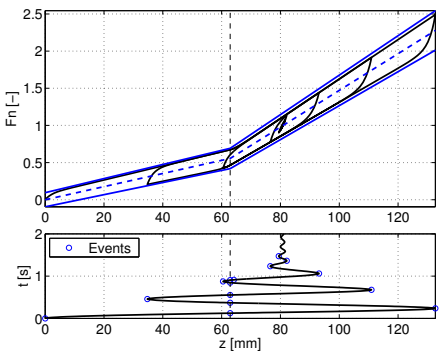

Figure B.16: Parabolic, $m = 7500$ kg.

B.3 Guided rod

The longitudinal clearance between the axle box and axle guidance on a two–axle freight wagon generates hard impacts if the clearance is exceeded. This is modelled using the generalised version of Newton's impact law from [60]. The axle box is considered as a rigid rod moving freely between four rigid contact points defined by the set

$$I_G = \{C1, C2, C3, C4\}$$

The four contact points model the axle guidance and the situation is shown in Figure B.17. The axle box has 3 DOF: x (longitudinal, positive towards C1 and C2), y (lateral, positive towards C1 and C3), ψ (yaw, positive in a counter clockwise rotation)

$$\mathbf{q} = [x, y, \psi]^T$$

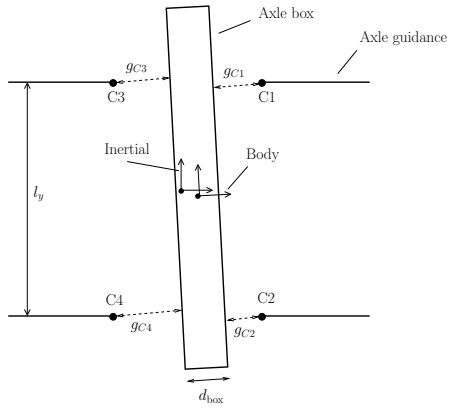

Figure B.17: Guided rod.

The coordinates of the contact points in reference to the inertial system is

$$\begin{aligned}
\mathbf{R}_1 &= [d_{\text{box}}/2 + d_{\text{clear}}, l_y/2]^T \\
\mathbf{R}_2 &= [d_{\text{box}}/2 + d_{\text{clear}}, -l_y/2]^T \\
\mathbf{R}_3 &= [-d_{\text{box}}/2 - d_{\text{clear}}, l_y/2]^T \\
\mathbf{R}_4 &= [-d_{\text{box}}/2 - d_{\text{clear}}, -l_y/2]^T
\end{aligned}$$

The constraint functions defining the distance between the axle box and the contact points are found by expressing the above contact point vectors in the body system, i.e.

$$\mathbf{R}_i = \begin{bmatrix} x \\ y \end{bmatrix} + \mathbf{A}_{IB}\mathbf{R}_i^{\text{body}} \quad \Rightarrow \quad \mathbf{R}_i^{\text{body}} = \mathbf{A}_{BI}\left(\mathbf{R}_i - \begin{bmatrix} x \\ y \end{bmatrix}\right)$$

where

$$\mathbf{A}_{BI} = \begin{bmatrix} \cos\psi & -\sin\psi \\ \sin\psi & \cos\psi \end{bmatrix}$$

Taking the local x–coordinate of $\mathbf{R}_i^{\text{body}}$ and then subtract the half width of the axle box yields the constraint functions, i.e.

$$\begin{aligned} g_{N1} &= (d_{\text{box}}/2 + d_{\text{clear}} - x)\cos\psi + (l_y/2 - y)\sin\psi - d_{\text{box}}/2 \\ g_{N2} &= (d_{\text{box}}/2 + d_{\text{clear}} - x)\cos\psi + (-l_y/2 - y)\sin\psi - d_{\text{box}}/2 \\ g_{N3} &= -(-d_{\text{box}}/2 - d_{\text{clear}} - x)\cos\psi + (l_y/2 - y)\sin\psi) - d_{\text{box}}/2 \\ g_{N4} &= -(-d_{\text{box}}/2 - d_{\text{clear}} - x)\cos\psi + (-l_y/2 - y)\sin\psi) - d_{\text{box}}/2 \end{aligned}$$

The set of active constraint functions is

$$I_S = \{i \in I_G | g_{Ni} = 0; \quad \dot{g}_{Ni} \leq 0\}$$

The equations of motion can be written as

$$\mathbf{M}\ddot{\mathbf{q}} - \mathbf{h} - \sum_{i \in I_S} (\mathbf{w}_N \lambda_N)_i = 0 \quad , \quad \mathbf{M} = \text{diag}([m, m, I_{zz}])$$

where $(\mathbf{w}_N \lambda_N)_i$ is the projection of the contact force at the i'th active contact point into the space of generalised coordinates. The vector $\mathbf{h}$ represents the sum of the external forces which, in this case, is $\mathbf{0}$, however, included for the generality of the derivation. The relative velocity in the normal direction for the i'th contact is

$$\dot{g}_{Ni} = \mathbf{w}_{Ni}^T \dot{\mathbf{q}} \quad , \quad \mathbf{w}_{Ni} = \frac{\partial g_{Ni}}{\partial \mathbf{q}} = \left[\frac{\partial g_{Ni}}{\partial x}, \frac{\partial g_{Ni}}{\partial y}, \frac{\partial g_{Ni}}{\partial \psi} \right]^T$$

In matrix–vector notation the equations of motion and the constraint functions are written as

$$\mathbf{M}\ddot{\mathbf{q}} - \mathbf{h} - \mathbf{W}_N \boldsymbol{\lambda}_N = \mathbf{0} \quad , \quad \dot{\mathbf{g}}_N = \mathbf{W}_N^T \dot{\mathbf{q}}$$

Denote the impact time by t_A and the detachment time by t_E. Assuming that the duration of the impact is very short one can rewrite the equations of motion on the impulse level

$$\lim_{t_E \to t_A} \int_{t_A}^{t_E} (\mathbf{M}\ddot{\mathbf{q}} - \mathbf{h} - \mathbf{W}_N \boldsymbol{\lambda}_N)\, \mathrm{d}t = \mathbf{M}(\dot{\mathbf{q}}_E - \dot{\mathbf{q}}_A) - \mathbf{W}_N \boldsymbol{\Lambda}_N = \mathbf{0}$$

where

$$\boldsymbol{\Lambda}_N = \lim_{t_E \to t_A} \int_{t_A}^{t_E} \boldsymbol{\lambda}_N \, \mathrm{d}t$$

The relative velocity in the normal direction at t_A and t_E is

$$\dot{\mathbf{g}}_{NA} = \mathbf{W}_N^T \dot{\mathbf{q}}_A \quad , \quad \dot{\mathbf{g}}_{NE} = \mathbf{W}_N^T \dot{\mathbf{q}}_E$$

Subtracting these two equations yields

$$\dot{\mathbf{g}}_{NE} - \dot{\mathbf{g}}_{NA} = \mathbf{W}_N^T(\dot{\mathbf{q}}_E - \dot{\mathbf{q}}_A) \tag{B.5}$$

Combining this information with the impulse formulation of the equations of motion yields

$$\dot{\mathbf{g}}_{NE} - \dot{\mathbf{g}}_{NA} = \mathbf{W}_N^T\mathbf{M}^{-1}\mathbf{W}_N\boldsymbol{\Lambda}_N \tag{B.6}$$

Newton's impact law can be expressed by the corner law in Figure B.18, see [16], [60]. This means that

$$\dot{\mathbf{g}}_{NE} + \boldsymbol{\epsilon}_N\dot{\mathbf{g}}_{NA} \geq \mathbf{0} \quad , \quad \boldsymbol{\Lambda}_N \geq \mathbf{0} \quad , \quad (\dot{\mathbf{g}}_{NE} + \boldsymbol{\epsilon}_N\dot{\mathbf{g}}_{NA})^T\boldsymbol{\Lambda}_N = 0$$

where $\boldsymbol{\epsilon}_N = \mathrm{diag}\{\epsilon_{Ni}\}$ contains the coefficients of restitution. A LCP can now be formulated by adding $\boldsymbol{\epsilon}_N\dot{\mathbf{g}}_{NA}$ to equation (B.6)

$$\underbrace{\dot{\mathbf{g}}_{NE} + \boldsymbol{\epsilon}_N\dot{\mathbf{g}}_{NA}}_{\boldsymbol{\xi}} = \underbrace{\mathbf{W}_N^T\mathbf{M}^{-1}\mathbf{W}_N}_{\mathbf{A}}\boldsymbol{\Lambda}_N + \underbrace{(\mathbf{I} + \boldsymbol{\epsilon}_N)\dot{\mathbf{g}}_{NA}}_{\mathbf{b}}$$

The matrix $\mathbf{I}$ is the identity matrix. In simplified notation the LCP problem is formulated as

$$\boldsymbol{\xi} = \mathbf{A}\boldsymbol{\Lambda}_N + \mathbf{b} \quad , \quad \mathbf{0} \leq \boldsymbol{\xi} \perp \boldsymbol{\Lambda}_N \geq \mathbf{0}$$

See Appendix D for a description on how to solve the LCP. The LCP is solved for $\boldsymbol{\xi}$ and $\boldsymbol{\Lambda}_N$. After solving the LCP the simulation is continued with an initial condition that is adjusted according to the velocity vector expressed in equation (B.7), which is deduced by combining equation (B.5) and (B.6).

$$\dot{\mathbf{q}}_E = \dot{\mathbf{q}}_A + \mathbf{M}^{-1}\mathbf{W}_N\boldsymbol{\Lambda}_N \tag{B.7}$$

The impact model presented above introduces a discontinuity into the system. The time instant of the impact is located during simulation and the state machine of the model is shown in Figure B.19.

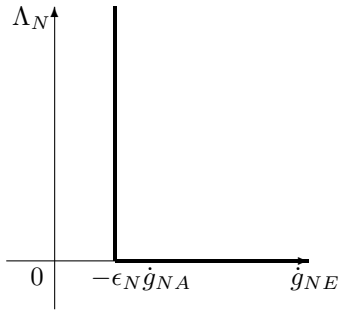

Figure B.18: Newton's impact law.

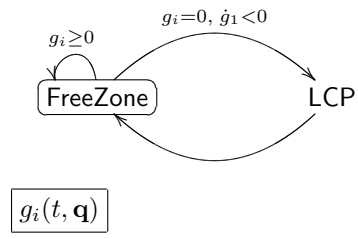

Figure B.19: State machine.

The parameters used for the numerical simulation presented in the following are $m = 1022$ kg, $I_{zz} = 678$ kg m^2, $l_y = 2.0$ m, $d_{\text{box}} = 0.265$ m, $d_{\text{clear}} = 4 \cdot 0.0225$ m. The clearance is exaggerated by a factor 4 for visualisation purposes. The simulation shown in Figure B.20 and B.21 has the initial condition

$$[x, \dot{x}, y, \dot{y}, \psi, \dot{\psi}] = [0, 0.12, 0, 0, 0, 0.001]$$

Note the irregular motion. The simulation shown in Figure B.22 and B.23 has the initial condition

$$[x, \dot{x}, y, \dot{y}, \psi, \dot{\psi}] = [0, 0.2, 0, 0, 0, 0]$$

The behaviour is still as expected even though there are double impacts. Note also the influence of the coefficient of restitution in time history of the x–coordinate where it is seen that the impacts becomes less frequent as time goes by.

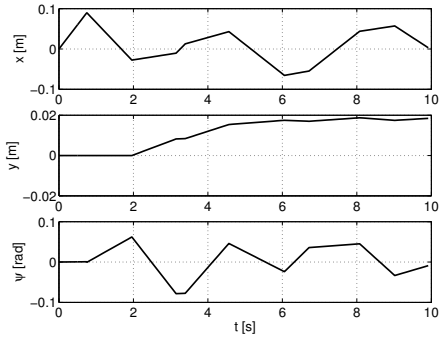

Figure B.20: Time history.

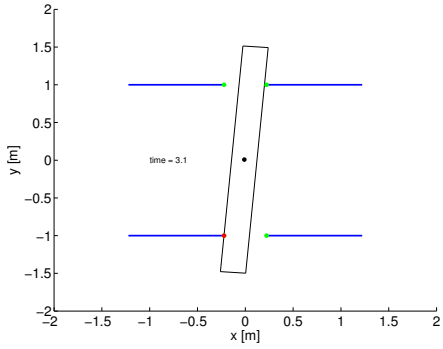

Figure B.21: Single contact.

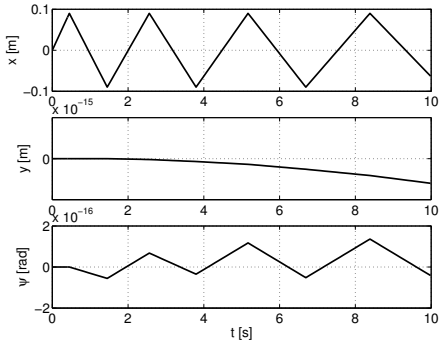

Figure B.22: Time history.

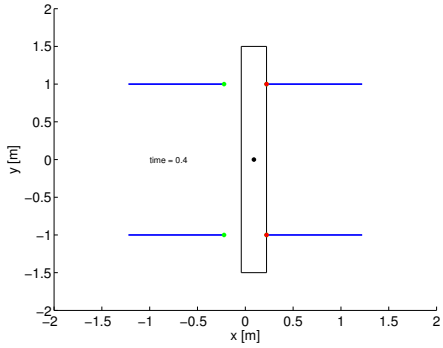

Figure B.23: Double contact.

B.4 Constrained wheel–rail contact

A single wheelset with conical profiles is simulated on a straight and level track using the theory from [74]. The wheel–rail contact is considered to be a rigid constraint eventually leading to a differential–algebraic equation (DAE) system describing the motion of the wheelset. The model is implemented in MATLAB.

Multibody system

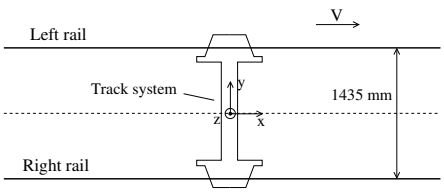

Figure B.24: Top view.

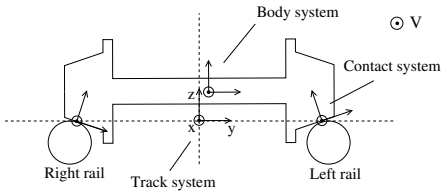

Figure B.25: Front view.

The German BA004 [68] wheelset is simulated. The mass is 1032 kg and the moments of inertia are $I_{xx} = I_{zz} = 529.8$ kg m^2 and $I_{yy} = 89.9$ kg m^2. The nominal rolling radius is $r_0 = 0.46$ m. The lateral distance from the centre of mass to the circular wheel section having radius r_0 is 0.75 m. The track gauge is 1435 mm, which is measured 14 mm below the top of the rails.

The multibody system is illustrated in Figure B.24 and B.25. Three bodies are considered: 1) Wheelset 2) Left rail 3) Right rail. The motion of the wheelset is defined relative to the track system, which moves with the constant speed V along the track. Furthermore, a body system is defined for the wheelset. The origin is in the centre of mass and the axes are aligned with the principal axes of the wheelset. The body system is obtained from the track system by two successive rotations: 1) ψ (yaw) around the vertical axis 2) ϕ (roll) around the longitudinal axis. For the computation of the tangential contact forces it is convenient to define a contact coordinate system for each contact point (see Figure B.25). The origin is in the contact point and the axes are obtained by rotating the body system around its longitudinal axis into the contact plane. All defined coordinate systems are right hand systems.

For simplicity and in order to avoid multiple contacts on a single wheel it is assumed that the wheel profiles are conical and the rail profiles are circular. The contact is also assumed to be two dimensional and hence the yaw angle is neglected in the computation of the normal contact forces. The conicity of the wheel is δ and the radius of the circular rails is $R = 0.21$ m.

The profiles are described in parametric form by $\bar{\mathbf{u}}^{ik}$, where i and k are body and contact numbers, respectively. This numbering is given in Table B.2. For each profile, the vector $\bar{\mathbf{u}}^{ik}$ refers to a local system, i.e. the wheel profiles are

defined in the body system and the rail profiles are defined in the track system. This yields the simplest (and most natural) representation of the profiles. The wheel profile parameters, s^{11} and s^{12}, measure the lateral distance w.r.t. to a reference point at r_0, and the rail profile parameters, s^{21} and s^{32}, measure the angle with vertical (see Figure B.26). Thus

$$\bar{\mathbf{u}}^{11} = \begin{bmatrix} y_0^{11} + s^{11} \\ -r_0 + s^{11}\tan\delta \end{bmatrix} \quad \bar{\mathbf{u}}^{12} = \begin{bmatrix} y_0^{12} + s^{12} \\ -r_0 - s^{12}\tan\delta \end{bmatrix}$$

$$\bar{\mathbf{u}}^{21} = \begin{bmatrix} y_0^{21} - R\sin s^{21} \\ R(\cos s^{21} - 1) \end{bmatrix} \quad \bar{\mathbf{u}}^{32} = \begin{bmatrix} y_0^{32} - R\sin s^{32} \\ R(\cos s^{32} - 1) \end{bmatrix}$$

where

$$y_0^{11} = 0.75 \text{ m} \qquad y_0^{12} = -0.75 \text{ m} \qquad y_0^{21} = 0.79 \text{ m} \qquad y_0^{32} = -0.79 \text{ m}$$

Here, y_0^{11} and y_0^{12} are the lateral distances from the centre of mass of the wheelset to the reference points at r_0 on the left and right wheels, respectively, and y_0^{21} and y_0^{32} are the lateral distances from the centre of the track to the reference points on top of the left and right rails, respectively.

	1	**2**	**3**
i (body index)	Wheelset	Left rail	Right rail
k (contact index)	Left contact point	Right contact point	–

Table B.2: Body and contact numbering.

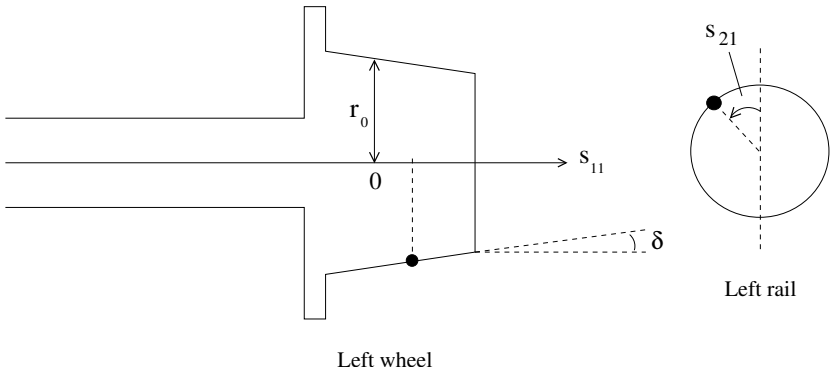

Figure B.26: Profile parameters (front view).

Equations of motion

The motion of any multibody system can be found using Newton–Euler equations [73, 60, 11]. For a single wheelset with fixed speed on a straight track the

equations of motion are

$$\begin{array}{rcl} \mathbf{M}\ddot{\mathbf{q}} & = & \mathbf{Q}(\mathbf{q},\dot{\mathbf{q}}) \\ \dot{\beta} & = & h(\mathbf{q},\dot{\mathbf{q}}) \end{array} \tag{B.8}$$

$$\begin{array}{rcl} \mathbf{Q}(\mathbf{q},\dot{\mathbf{q}}) & = & \left[\begin{array}{c} F_y \\ F_z \\ I_{yy}\dot{\psi}V/r_0 + M_x \\ -I_{yy}\dot{\phi}V/r_0 + M_z \end{array}\right] \\ h(\mathbf{q},\dot{\mathbf{q}}) & = & M_y/I_{yy} \end{array}$$

The position and orientation of the wheelset are defined by $\mathbf{q} = [y, z, \phi, \psi]^T$. The coordinate β is called the spin perturbation and defines the difference between the actual spin and the nominal value of V/r_0. The x–coordinate is fixed relative to the track system, hence the wheelset is constrained to move with the speed V along the track. This yields an energy input and is a simple way to provide a steady motion of the wheelset. It is seen that the wheelset has 5 degrees of freedom. The mass matrix is $\mathbf{M} = \mathrm{diag}(m, m, I_{xx}, I_{zz})$ and the external forces and torques affecting the wheelset are $\mathbf{F}_{\mathrm{ext}} = [F_x, F_y, F_z]^T$ and $\mathbf{M}_{\mathrm{ext}} = [M_x, M_y, M_z]^T$.

Wheel–rail constraints

By imposing two rail constraints the number of degrees of freedom is reduced. The yaw angle ψ is neglected in the computations of the normal contact forces and therefore $\mathbf{q} = [y, z, \phi]^T$ and $\mathbf{Q} = [F_y, F_z, I_{yy}\dot{\psi}V/r_0 + M_x]^T$. The coordinates $\mathbf{q}$ are only descriptor variables now and not degrees of freedom because y, z and ϕ are connected through the wheel–rail constraints. Two conditions are imposed for each wheel–rail contact

1. The contact point on the wheel and rail should be identical in space (contact point constraint)
2. The normal vectors to the wheel and rail profiles are aligned (orientation constraint)

These two conditions are written in the contact constraint equation

$$\mathbf{C}(\mathbf{q},\mathbf{s}) = \left[\begin{array}{c} \mathbf{R}^1 + \mathbf{A}^1\bar{\mathbf{u}}^{11} - \bar{\mathbf{u}}^{21} \\ \mathbf{R}^1 + \mathbf{A}^1\bar{\mathbf{u}}^{12} - \bar{\mathbf{u}}^{32} \\ \bar{\mathbf{n}}^{21T}\mathbf{A}^1\bar{\mathbf{t}}^{11} \\ \bar{\mathbf{n}}^{32T}\mathbf{A}^1\bar{\mathbf{t}}^{12} \end{array}\right] = \mathbf{0} \tag{B.9}$$

where

$$\bar{\mathbf{t}}^{ik} \equiv (\bar{\mathbf{u}}^{ik})' \quad , \quad \bar{\mathbf{n}}^{ik} \equiv \hat{\bar{\mathbf{t}}}^{ik} = (\hat{\bar{\mathbf{u}}}^{ik})'$$

and

$$\mathbf{q} = \begin{bmatrix} y \\ z \\ \phi \end{bmatrix} \qquad \mathbf{R}^1 = \begin{bmatrix} y \\ r_0 + z \end{bmatrix} \qquad \mathbf{A}^1 = \begin{bmatrix} \cos\phi & -\sin\phi \\ \sin\phi & \cos\phi \end{bmatrix}$$

The notation $(.)'$ means differentiation w.r.t. its argument. For example, the vector $\bar{\mathbf{u}}^{ik}$ depends on the parameter s^{ik} hence $(\bar{\mathbf{u}}^{ik})' = \mathrm{d}\bar{\mathbf{u}}^{ik}/\,\mathrm{d}s^{ik}$. The vector $\hat{\mathbf{v}}$ is defined by $\hat{\mathbf{v}} = [-v_2, v_1]^T$.

The profiles are described by the four parameters $\mathbf{s} = [s^{11}, s^{21}, s^{12}, s^{32}]^T$. These parameters are determined through the contact constraint equation (B.9). Since there are four unknown parameters and six constraint equations the number of degrees of freedom is reduced by two, that is $z(y)$ and $\phi(y)$.

DAE formulation

The normal contact forces are taken into account by imposing *Lagrange multipliers* to the equations of motion [73, 75, 74, 11]

$$\mathbf{M}\ddot{\mathbf{q}} + \mathbf{C}_\mathbf{q}^T\boldsymbol{\lambda} = \mathbf{Q}(\mathbf{q}, \dot{\mathbf{q}}, \mathbf{s}, \dot{\mathbf{s}}, \boldsymbol{\lambda}) \tag{B.10}$$

where $\boldsymbol{\lambda}$ is the Lagrange multipliers and $\mathbf{C}_\mathbf{q} = [\partial\mathbf{C}/\partial y, \partial\mathbf{C}/\partial z, \partial\mathbf{C}/\partial\phi]$. The external forces incorporated into the right hand side function $\mathbf{Q}$ should not include the normal forces because they are taken into account through the Lagrange multipliers $\boldsymbol{\lambda}$. The equations of motion given in equation (B.10) together with the contact constraint equation (B.9) is a DAE system of differential index 3 [92] and not directly solvable. To come around this problem a reformulation is presented using the augmented Lagrangian form [75]. The contact constraint equation is differentiated twice w.r.t. time (index reduction)

$$\mathbf{C}(\mathbf{q}, \mathbf{s}) = \mathbf{0} \tag{B.11}$$

$$\mathbf{C}_\mathbf{q}\dot{\mathbf{q}} + \mathbf{C}_\mathbf{s}\dot{\mathbf{s}} = \mathbf{0} \tag{B.12}$$

$$\mathbf{C}_\mathbf{q}\ddot{\mathbf{q}} + \mathbf{C}_\mathbf{s}\ddot{\mathbf{s}} = -(\mathbf{C}_\mathbf{q}\dot{\mathbf{q}})_\mathbf{q}\dot{\mathbf{q}} - (\mathbf{C}_\mathbf{q}\dot{\mathbf{q}})_\mathbf{s}\dot{\mathbf{s}} - (\mathbf{C}_\mathbf{s}\dot{\mathbf{s}})_\mathbf{q}\dot{\mathbf{q}} - (\mathbf{C}_\mathbf{s}\dot{\mathbf{s}})_\mathbf{s}\dot{\mathbf{s}} =: \mathbf{Q}_d \tag{B.13}$$

Since the normal contact forces are defined to be acting normal to the constraint manifold it is required that [75]

$$\mathbf{C}_\mathbf{s}^T\boldsymbol{\lambda} = \mathbf{0} \tag{B.14}$$

Combining equation (B.10), (B.13) and (B.14) it is found that

$$\begin{bmatrix} \mathbf{M} & \mathbf{0} & \mathbf{C}_\mathbf{q}^T \\ \mathbf{0} & \mathbf{0} & \mathbf{C}_\mathbf{s}^T \\ \mathbf{C}_\mathbf{q} & \mathbf{C}_\mathbf{s} & \mathbf{0} \end{bmatrix} \begin{bmatrix} \ddot{\mathbf{q}} \\ \ddot{\mathbf{s}} \\ \boldsymbol{\lambda} \end{bmatrix} = \begin{bmatrix} \mathbf{Q}(\mathbf{q}, \dot{\mathbf{q}}, \mathbf{s}, \dot{\mathbf{s}}, \boldsymbol{\lambda}) \\ \mathbf{0} \\ \mathbf{Q}_d(\mathbf{q}, \dot{\mathbf{q}}, \mathbf{s}, \dot{\mathbf{s}}) \end{bmatrix}, \quad \begin{aligned} &\mathbf{M} = \mathrm{diag}(m, m, I_{xx}) \\ &\mathbf{q} = [y, z, \phi]^T \\ &\mathbf{s} = [s^{11}, s^{21}, s^{12}, s^{32}]^T \end{aligned} \tag{B.15}$$

This equation can be solved in order to determine the accelerations and the Lagrange multipliers. Note that the right hand side is dependent on the Lagrange multipliers because the tangential contact forces depend nonlinearly on

the normal load. Thus equation (B.15) is nonlinear in $\boldsymbol{\lambda}$. To solve equation (B.15) it is necessary to know $\mathbf{C_q}$, $\mathbf{C_s}$ and $\mathbf{Q}_d$. It is seen that $\mathbf{A}^1_\phi \mathbf{v} = \mathbf{A}^1 \hat{\mathbf{v}}$ where $\hat{\mathbf{v}} = [-v_2, v_1]^T$. Utilising this information and by straight forward differentiation it is found that

$$\mathbf{C_q} = \begin{bmatrix} \mathbf{I}^{2\times 2} & \mathbf{A}^1\hat{\bar{\mathbf{u}}}^{11} \\ \mathbf{I}^{2\times 2} & \mathbf{A}^1\hat{\bar{\mathbf{u}}}^{12} \\ \mathbf{0}^{1\times 2} & \bar{\mathbf{n}}^{21T}\mathbf{A}^1\bar{\mathbf{n}}^{11} \\ \mathbf{0}^{1\times 2} & \bar{\mathbf{n}}^{32T}\mathbf{A}^1\bar{\mathbf{n}}^{12} \end{bmatrix}$$

$$\mathbf{C_s} = \begin{bmatrix} \mathbf{A}^1\bar{\mathbf{t}}^{11} & -\bar{\mathbf{t}}^{21} & \mathbf{0}^{2\times 1} & \mathbf{0}^{2\times 1} \\ \mathbf{0}^{2\times 1} & \mathbf{0}^{2\times 1} & \mathbf{A}^1\bar{\mathbf{t}}^{12} & -\bar{\mathbf{t}}^{32} \\ \bar{\mathbf{n}}^{21T}\mathbf{A}^1(\bar{\mathbf{t}}^{11})' & \bar{\mathbf{t}}^{11T}\mathbf{A}^{1T}(\bar{\mathbf{n}}^{21})' & 0 & 0 \\ 0 & 0 & \bar{\mathbf{n}}^{32T}\mathbf{A}^1(\bar{\mathbf{t}}^{12})' & \bar{\mathbf{t}}^{12T}\mathbf{A}^{1T}(\bar{\mathbf{n}}^{32})' \end{bmatrix}$$

$$(\mathbf{C_q}\dot{\mathbf{q}})_\mathbf{q}\dot{\mathbf{q}} = \begin{bmatrix} -\mathbf{A}^1\bar{\mathbf{u}}^{11}\dot{\phi}^2 \\ -\mathbf{A}^1\bar{\mathbf{u}}^{12}\dot{\phi}^2 \\ -\bar{\mathbf{n}}^{21T}\mathbf{A}^1\bar{\mathbf{t}}^{11}\dot{\phi}^2 \\ -\bar{\mathbf{n}}^{32T}\mathbf{A}^1\bar{\mathbf{t}}^{12}\dot{\phi}^2 \end{bmatrix}$$

$$(\mathbf{C_q}\dot{\mathbf{q}})_\mathbf{s}\dot{\mathbf{s}} = (\mathbf{C_s}\dot{\mathbf{s}})_\mathbf{q}\dot{\mathbf{q}} = \begin{bmatrix} \mathbf{A}^1\bar{\mathbf{n}}^{11}\dot{\phi}\dot{s}^{11} \\ \mathbf{A}^1\bar{\mathbf{n}}^{12}\dot{\phi}\dot{s}^{12} \\ \bar{\mathbf{n}}^{21T}\mathbf{A}^1(\bar{\mathbf{n}}^{11})'\dot{\phi}\dot{s}^{11} + \bar{\mathbf{n}}^{11T}\mathbf{A}^{1T}(\bar{\mathbf{n}}^{21})'\dot{\phi}\dot{s}^{21} \\ \bar{\mathbf{n}}^{32T}\mathbf{A}^1(\bar{\mathbf{n}}^{12})'\dot{\phi}\dot{s}^{12} + \bar{\mathbf{n}}^{12T}\mathbf{A}^{1T}(\bar{\mathbf{n}}^{32})'\dot{\phi}\dot{s}^{32} \end{bmatrix}$$

$$(\mathbf{C_s}\dot{\mathbf{s}})_\mathbf{s}\dot{\mathbf{s}} = \begin{bmatrix} \mathbf{A}^1(\bar{\mathbf{t}}^{11})'(\dot{s}^{11})^2 - (\bar{\mathbf{t}}^{21})'(\dot{s}^{21})^2 \\ \mathbf{A}^1(\bar{\mathbf{t}}^{12})'(\dot{s}^{12})^2 - (\bar{\mathbf{t}}^{32})'(\dot{s}^{32})^2 \\ \bar{\mathbf{n}}^{21T}\mathbf{A}^1(\bar{\mathbf{t}}^{11})''(\dot{s}^{11})^2 + 2(\bar{\mathbf{n}}^{21T})'\mathbf{A}^1(\bar{\mathbf{t}}^{11})'\dot{s}^{11}\dot{s}^{21} + \bar{\mathbf{t}}^{11T}\mathbf{A}^{1T}(\bar{\mathbf{n}}^{21})''(\dot{s}^{21})^2 \\ \bar{\mathbf{n}}^{32T}\mathbf{A}^1(\bar{\mathbf{t}}^{12})''(\dot{s}^{12})^2 + 2(\bar{\mathbf{n}}^{32T})'\mathbf{A}^1(\bar{\mathbf{t}}^{12})'\dot{s}^{12}\dot{s}^{32} + \bar{\mathbf{t}}^{12T}\mathbf{A}^{1T}(\bar{\mathbf{n}}^{32})''(\dot{s}^{32})^2 \end{bmatrix}$$

For conical wheel profiles the following is valid

$$(\bar{\mathbf{t}}^{11})' = (\bar{\mathbf{t}}^{12})' = (\bar{\mathbf{t}}^{11})'' = (\bar{\mathbf{t}}^{12})'' = (\bar{\mathbf{n}}^{11})' = (\bar{\mathbf{n}}^{12})' = (\bar{\mathbf{n}}^{11})'' = (\bar{\mathbf{n}}^{12})'' = \mathbf{0} \tag{B.16}$$

By inserting $\bar{\mathbf{t}}^{ik} = (\bar{\mathbf{u}}^{ik})'$, $\bar{\mathbf{n}}^{ik} = \hat{\bar{\mathbf{t}}}^{ik} = (\hat{\bar{\mathbf{u}}}^{ik})'$ and equation (B.16) it is found

$$\mathbf{C}(\mathbf{q},\mathbf{s}) = \begin{bmatrix} \mathbf{R}^1 + \mathbf{A}^1\bar{\mathbf{u}}^{11} - \bar{\mathbf{u}}^{21} \\ \mathbf{R}^1 + \mathbf{A}^1\bar{\mathbf{u}}^{12} - \bar{\mathbf{u}}^{32} \\ (\hat{\bar{\mathbf{u}}}^{21T})'\mathbf{A}^1(\bar{\mathbf{u}}^{11})' \\ (\hat{\bar{\mathbf{u}}}^{32T})'\mathbf{A}^1(\bar{\mathbf{u}}^{12})' \end{bmatrix} \quad , \quad \mathbf{C_q} = \begin{bmatrix} \mathbf{I}^{2\times 2} & \mathbf{A}^1\hat{\bar{\mathbf{u}}}^{11} \\ \mathbf{I}^{2\times 2} & \mathbf{A}^1\hat{\bar{\mathbf{u}}}^{12} \\ \mathbf{0}^{1\times 2} & (\hat{\bar{\mathbf{u}}}^{21T})'\mathbf{A}^1(\hat{\bar{\mathbf{u}}}^{11})' \\ \mathbf{0}^{1\times 2} & (\hat{\bar{\mathbf{u}}}^{32T})'\mathbf{A}^1(\hat{\bar{\mathbf{u}}}^{12})' \end{bmatrix}$$

$$\mathbf{C_s} = \begin{bmatrix} \mathbf{A}^1(\bar{\mathbf{u}}^{11})' & -(\bar{\mathbf{u}}^{21})' & \mathbf{0}^{2\times 1} & \mathbf{0}^{2\times 1} \\ \mathbf{0}^{2\times 1} & \mathbf{0}^{2\times 1} & \mathbf{A}^1(\bar{\mathbf{u}}^{12})' & -(\bar{\mathbf{u}}^{32})' \\ 0 & (\bar{\mathbf{u}}^{11T})'\mathbf{A}^{1T}(\hat{\bar{\mathbf{u}}}^{21})'' & 0 & 0 \\ 0 & 0 & 0 & (\bar{\mathbf{u}}^{12T})'\mathbf{A}^{1T}(\hat{\bar{\mathbf{u}}}^{32})'' \end{bmatrix}$$

$$(\mathbf{C_q}\dot{\mathbf{q}})_\mathbf{q}\dot{\mathbf{q}} = \begin{bmatrix} -\mathbf{A}^1\bar{\mathbf{u}}^{11}\dot{\phi}^2 \\ -\mathbf{A}^1\bar{\mathbf{u}}^{12}\dot{\phi}^2 \\ -(\hat{\bar{\mathbf{u}}}^{21T})'\mathbf{A}^1(\bar{\mathbf{u}}^{11})'\dot{\phi}^2 \\ -(\hat{\bar{\mathbf{u}}}^{32T})'\mathbf{A}^1(\bar{\mathbf{u}}^{12})'\dot{\phi}^2 \end{bmatrix} \quad , \quad (\mathbf{C_s}\dot{\mathbf{s}})_\mathbf{s}\dot{\mathbf{s}} = \begin{bmatrix} -(\bar{\mathbf{u}}^{21})''(\dot{s}^{21})^2 \\ -(\bar{\mathbf{u}}^{32})''(\dot{s}^{32})^2 \\ (\bar{\mathbf{u}}^{11T})'\mathbf{A}^{1T}(\hat{\bar{\mathbf{u}}}^{21})'''(\dot{s}^{21})^2 \\ (\bar{\mathbf{u}}^{12T})'\mathbf{A}^{1T}(\hat{\bar{\mathbf{u}}}^{32})'''(\dot{s}^{32})^2 \end{bmatrix}$$

$$(\mathbf{C_q}\dot{\mathbf{q}})_\mathbf{s}\dot{\mathbf{s}} = (\mathbf{C_s}\dot{\mathbf{s}})_\mathbf{q}\dot{\mathbf{q}} = \begin{bmatrix} \mathbf{A}^1(\hat{\bar{\mathbf{u}}}^{11})'\dot{\phi}\dot{s}^{11} \\ \mathbf{A}^1(\hat{\bar{\mathbf{u}}}^{12})'\dot{\phi}\dot{s}^{12} \\ (\hat{\bar{\mathbf{u}}}^{11T})'\mathbf{A}^{1T}(\hat{\bar{\mathbf{u}}}^{21})''\dot{\phi}\dot{s}^{21} \\ (\hat{\bar{\mathbf{u}}}^{12T})'\mathbf{A}^{1T}(\hat{\bar{\mathbf{u}}}^{32})''\dot{\phi}\dot{s}^{32} \end{bmatrix}$$

Forces

The external forces (track system) and torques (body system) are given by

$$\begin{bmatrix} F_x \\ F_y \\ F_z \end{bmatrix} = \mathbf{F}_g + \mathbf{F}_s + \mathbf{A}_{Tb}(\mathbf{F}_{fl} + \mathbf{F}_{fr}) + \mathbf{A}_{Tcl}\mathbf{F}_{cl} + \mathbf{A}_{Tcr}\mathbf{F}_{cr}$$

$$\begin{bmatrix} M_x \\ M_y \\ M_z \end{bmatrix} = \mathbf{R}_{cl} \times (\mathbf{A}_{bcl}\mathbf{F}_{cl} + \mathbf{F}_{fl}) + \mathbf{R}_{cr} \times (\mathbf{A}_{bcr}\mathbf{F}_{cr} + \mathbf{F}_{fr})$$

$\mathbf{F}_g$ is the gravitational force, $\mathbf{F}_s$ is a lateral suspension force, $\mathbf{F}_{cl}$, $\mathbf{F}_{cr}$ are the wheel–rail contact forces, $\mathbf{F}_{fl}$, $\mathbf{F}_{fr}$ are flange forces, $\mathbf{A}_{Tb}$, $\mathbf{A}_{Tcl}$, $\mathbf{A}_{Tcr}$, $\mathbf{A}_{bcl}$, $\mathbf{A}_{bcr}$ are rotation matrices and $\mathbf{R}_{cl}$, $\mathbf{R}_{cr}$ are position vectors from the centre of mass of the wheelset to the contact points. The gravitational force and primary suspension are modelled by

$$\mathbf{F}_g = \begin{bmatrix} 0 \\ 0 \\ -mg \end{bmatrix} \quad , \quad \mathbf{F}_s = \begin{bmatrix} 0 \\ -k_s y \\ 0 \end{bmatrix}$$

The flange is modelled by a stiff spring with a dead band

$$\mathbf{F}_{fl} = \begin{cases} \mathbf{0} & y \le y_f \\ [0, -k_f(y - y_f), 0]^T & y > y_f \end{cases}$$

$$\mathbf{F}_{fr} = \begin{cases} [0, -k_f(y + y_f), 0]^T & y < -y_f \\ \mathbf{0} & y \ge -y_f \end{cases}$$

where $k_s = 1.823$ MN/m, $k_f = 14.60$ MN/m and $y_f = 0.0091$ m. These values are from Cooperrider's bogie [8, 38]. The nonsmooth characteristic of the dead band spring is appropriately divided into its natural states and the switching boundaries between the states are located during the numerical integration. To keep focus on the treatment of the DAE issues, the event location procedure is not further discussed here. The rotation matrices are

$$\mathbf{A}_{Tb} = \begin{bmatrix} \cos\psi & -\sin\psi\cos\phi & \sin\psi\sin\phi \\ \sin\psi & \cos\psi\cos\phi & -\cos\psi\sin\phi \\ 0 & \sin\phi & \cos\phi \end{bmatrix}$$

$$\mathbf{A}_{Tcl} = \begin{bmatrix} \cos\psi & -\sin\psi\cos(\phi+\delta) & \sin\psi\sin(\phi+\delta) \\ \sin\psi & \cos\psi\cos(\phi+\delta) & -\cos\psi\sin(\phi+\delta) \\ 0 & \sin(\phi+\delta) & \cos(\phi+\delta) \end{bmatrix}$$

$$\mathbf{A}_{Tcr} = \begin{bmatrix} \cos\psi & -\sin\psi\cos(\phi-\delta) & \sin\psi\sin(\phi-\delta) \\ \sin\psi & \cos\psi\cos(\phi-\delta) & -\cos\psi\sin(\phi-\delta) \\ 0 & \sin(\phi-\delta) & \cos(\phi-\delta) \end{bmatrix}$$

$$\mathbf{A}_{bcl} = \begin{bmatrix} 1 & 0 & 0 \\ 0 & \cos(\delta) & -\sin(\delta) \\ 0 & \sin(\delta) & \cos(\delta) \end{bmatrix} \quad , \quad \mathbf{A}_{bcr} = \begin{bmatrix} 1 & 0 & 0 \\ 0 & \cos(\delta) & \sin(\delta) \\ 0 & -\sin(\delta) & \cos(\delta) \end{bmatrix}$$

The position of the contact point is found using the profile parameters

$$\mathbf{R}_{cl} = \begin{bmatrix} 0 \\ y_0^{11} + s^{11} \\ -r_0 + s^{11}\tan\delta \end{bmatrix} \quad , \quad \mathbf{R}_{cr} = \begin{bmatrix} 0 \\ y_0^{12} + s^{12} \\ -r_0 - s^{12}\tan\delta \end{bmatrix}$$

The normal forces are found using the Lagrange multipliers

$$N_l = \sqrt{\lambda_1^2 + \lambda_2^2} \qquad N_r = \sqrt{\lambda_3^2 + \lambda_4^2}$$

The tangential contact forces (creep forces) depends on the relative velocity between the wheel and rail (creep). The creep is computed using the following approximations.

$$\begin{aligned}
\xi_{x,cl} &\approx 1 + ((V/r_0 + \beta)\bar{u}_2^{11} - \dot{\psi}\bar{u}_1^{11})/V \\
\xi_{x,cr} &\approx 1 + ((V/r_0 + \beta)\bar{u}_2^{12} - \dot{\psi}\bar{u}_1^{12})/V \\
\xi_{y,cl} &\approx (-\psi V + \dot{y} - \dot{\phi}\bar{u}_2^{11})/(V\cos\delta) \\
\xi_{y,cr} &\approx (-\psi V + \dot{y} - \dot{\phi}\bar{u}_2^{12})/(V\cos\delta) \\
\xi_{s,cl} &\approx (\dot{\psi}\cos\delta - (V/r_0 + \beta)\sin\delta)/V \\
\xi_{s,cr} &\approx (\dot{\psi}\cos\delta + (V/r_0 + \beta)\sin\delta)/V
\end{aligned}$$

The creep forces T_x and T_y are calculated using the nonlinear model proposed by Shen–Hedrick–Elkins [78]

$$T_x = \epsilon\tilde{F}_x \quad , \quad T_y = \epsilon\tilde{F}_y$$

where

$$a = a_0(N/N_0)^{1/3} \quad , \quad b = b_0(N/N_0)^{1/3}$$

$$\begin{aligned}
\tilde{F}_x &= -abGC_{11}\xi_x \\
\tilde{F}_y &= -abG\left(C_{22}\xi_y + \sqrt{ab}C_{23}\xi_s\right)
\end{aligned}$$

$$|\tilde{\mathbf{F}}| = \sqrt{\tilde{F}_x^2 + \tilde{F}_y^2}$$

$$|\mathbf{F}| = \begin{cases} \mu N\left(u - \frac{1}{3}u^2 + \frac{1}{27}u^3\right) & u < 3 \\ \mu N & u \geq 3 \end{cases} \quad , \quad u = \frac{|\tilde{\mathbf{F}}|}{\mu N}$$

$$\epsilon = |\mathbf{F}|/|\tilde{\mathbf{F}}|$$

and $a_0 = 2.8134$ mm, $b_0 = 1.6745$ mm, $N_0 = 5073$ N, $C_{11} = 4.8530$, $C_{22} = 4.5548$, $C_{23} = 2.2666$, $G = 8.27 \cdot 10^{10}$ N/m^2, $\nu = 0.27$, $\mu = 0.30$. Here, C_{11}, C_{22}, C_{23} are Kalker's creepage coefficients [39]. The contact forces are

$$\mathbf{F}_{cl} = [T_{x,cl}, T_{y,cl}, N_l]^T \qquad \mathbf{F}_{cr} = [T_{x,cr}, T_{y,cr}, N_r]^T$$

Note that in computing the term $\mathbf{Q}$ in equation (B.15) the normal forces should be excluded because they are taken into account using the Lagrange multipliers.

Numerical integration

1. *Initial condition*: The coordinates $y_0, \psi_0, \dot{y}_0, \dot{\psi}_0, \beta_0$ are specified. The dependent coordinates $\mathbf{q}_{d,0} = [z_0, \phi_0]^T$, $\dot{\mathbf{q}}_{d,0} = [\dot{z}_0, \dot{\phi}_0]^T$, $\mathbf{s}$ and $\dot{\mathbf{s}}$ are determined by solving equation (B.11) and (B.12). Equation (B.11) is solved using Newton–Raphson's method (see e.g. [76]). From a simple geometric consideration the following initial value is found appropriate

$$\begin{bmatrix} z \\ \phi \\ s^{11} \\ s^{21} \\ s^{12} \\ s^{32} \end{bmatrix} = \begin{bmatrix} 0 \\ 0 \\ (y_0^{21} - y_0^{11}) - R\sin\delta \\ \delta \\ (y_0^{32} - y_0^{12}) + R\sin\delta \\ -\delta \end{bmatrix}$$

and the Jacobi matrix is

$$\mathbf{J} = [\mathbf{C}_{\mathbf{q}_d}, \mathbf{C}_{\mathbf{s}}] \qquad , \quad \mathbf{q}_d = [z, \phi]^T$$

Equation (B.12) is solved by exploiting the linearity, i.e.

$$[\mathbf{C}_{\mathbf{q}_d}, \mathbf{C}_{\mathbf{s}}] \begin{bmatrix} \dot{\mathbf{q}}_d \\ \dot{\mathbf{s}} \end{bmatrix} = -\mathbf{C}_{\mathbf{q}_i}\dot{\mathbf{q}}_i \qquad , \qquad \begin{matrix} \mathbf{q}_i = y \\ \mathbf{q}_d = [z, \phi]^T \end{matrix}$$

2. Equation (B.15) is solved using fixed–point iteration. This gives the current value of $\ddot{\mathbf{q}}$ and $\boldsymbol{\lambda}$. The static load is used as a first initial guess, however, during simulation the previous value gives a better estimate. From the static load it is found

$$\boldsymbol{\lambda}_0 = \left[\frac{mg}{2}\tan\delta, -\frac{mg}{2}, -\frac{mg}{2}\tan\delta, -\frac{mg}{2}, 0, 0\right]^T$$

3. The independent accelerations are integrated one step forward in time
4. The new value of the dependent coordinates are found through solving equation (B.11) and (B.12)
5. Repeat step 2. to 4. until the end of the simulation is reached

Implementation

In order to integrate the DAE system in MATLAB the following formulation of the system is presented

$$\mathbf{y} = [y, \psi, \dot{y}, \dot{\psi}, \beta, z, \phi, s^{11}, s^{21}, s^{12}, s^{32}]^T$$

$$\mathbf{M}\dot{\mathbf{y}} = \begin{cases} y_3 \\ y_4 \\ \ddot{y} \qquad \text{(known from equation (B.15))} \\ (-I_{yy}\dot{\phi}V/r_0 + M_z)/I_{zz} \\ M_y/I_{yy} \\ \mathbf{C}(\mathbf{q}, \mathbf{s}) \quad \text{(see equation (B.9))} \end{cases}$$

where

$$\mathbf{q} = [y_1, y_6, y_7]^T \qquad \mathbf{s} = [y_8, y_9, y_{10}, y_{11}]^T$$

and $\mathbf{M}$ is the *singular* mass matrix providing zeros on the left hand side in the 6 last equations, see equation (B.17). The dependencies of the right hand side function are important for an efficient computation of the Jacobi matrix, which is needed when using an implicit numerical integrator. The dependencies are given in $\mathbf{J}_{\text{pattern}}$, see equation (B.18). The system is integrated using the MATLAB solver `ode15s`.

$$\mathbf{M} = \left[\begin{array}{cccccccccccc} 1 & 0 & 0 & 0 & 0 & 0 & 0 & 0 & 0 & 0 & 0 \\ 0 & 1 & 0 & 0 & 0 & 0 & 0 & 0 & 0 & 0 & 0 \\ 0 & 0 & 1 & 0 & 0 & 0 & 0 & 0 & 0 & 0 & 0 \\ 0 & 0 & 0 & 1 & 0 & 0 & 0 & 0 & 0 & 0 & 0 \\ 0 & 0 & 0 & 0 & 1 & 0 & 0 & 0 & 0 & 0 & 0 \\ \hline 0 & 0 & 0 & 0 & 0 & 0 & 0 & 0 & 0 & 0 & 0 \\ 0 & 0 & 0 & 0 & 0 & 0 & 0 & 0 & 0 & 0 & 0 \\ 0 & 0 & 0 & 0 & 0 & 0 & 0 & 0 & 0 & 0 & 0 \\ 0 & 0 & 0 & 0 & 0 & 0 & 0 & 0 & 0 & 0 & 0 \\ 0 & 0 & 0 & 0 & 0 & 0 & 0 & 0 & 0 & 0 & 0 \\ 0 & 0 & 0 & 0 & 0 & 0 & 0 & 0 & 0 & 0 & 0 \end{array}\right] \tag{B.17}$$

$$\mathbf{J}_{\text{pattern}} = \left[\begin{array}{cccccccccccc} 0 & 0 & 1 & 0 & 0 & 0 & 0 & 0 & 0 & 0 & 0 \\ 0 & 0 & 0 & 1 & 0 & 0 & 0 & 0 & 0 & 0 & 0 \\ 1 & 1 & 1 & 1 & 1 & 1 & 1 & 1 & 1 & 1 & 1 \\ 1 & 1 & 1 & 1 & 1 & 1 & 1 & 1 & 1 & 1 & 1 \\ 1 & 1 & 1 & 1 & 1 & 1 & 1 & 1 & 1 & 1 & 1 \\ 1 & 0 & 0 & 0 & 0 & 0 & 1 & 1 & 1 & 0 & 0 \\ 0 & 0 & 0 & 0 & 0 & 1 & 1 & 1 & 1 & 0 & 0 \\ 1 & 0 & 0 & 0 & 0 & 0 & 1 & 0 & 0 & 1 & 1 \\ 0 & 0 & 0 & 0 & 0 & 1 & 1 & 0 & 0 & 1 & 1 \\ 0 & 0 & 0 & 0 & 0 & 0 & 1 & 0 & 1 & 0 & 0 \\ 0 & 0 & 0 & 0 & 0 & 0 & 1 & 0 & 0 & 0 & 1 \end{array}\right] \tag{B.18}$$

Results

In Figure B.27 to B.30 the results from a simulation at 20 m/s are shown. The wheelset is not suspended. The conicity is $\delta = 0.05$. The centre track solution is unstable, however, the amplitude of the oscillations are limited by the flange.

In Figure B.31 and B.32 the results from a simulation at 100 m/s are shown. The wheelset is suspended, $k_s = 1.823$ MN/m. The conicity is still $\delta = 0.05$. The centre track solution is now stable. Note that $\delta + \phi = s^{21} \approx 0.05$ because the wheel profile is conical and the rails are circular. Similarly, $\delta - \phi = -s^{32} \approx 0.05$.

In Figure B.33 and B.34 the speed is still 100 m/s. The wheelset is suspended, $k_s = 1.823$ MN/m. The conicity is set to $\delta = 0.08$. It is seen that this higher conicity makes the centre track solution unstable. Again, $\delta + \phi = s^{21} \approx 0.08$ and $\delta - \phi = -s^{32} \approx 0.08$.

These results confirm our expectations from experience.

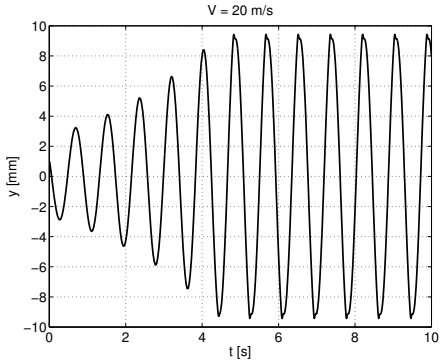

Figure B.27: $y(t)$, $\delta = 0.05$, $k_s = 0$.

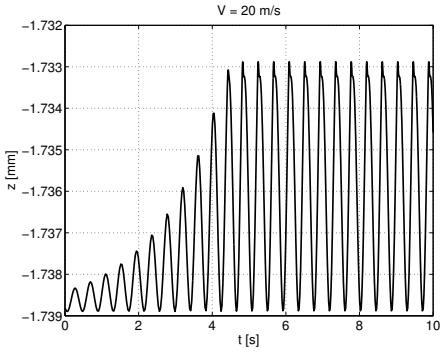

Figure B.28: $z(t)$, $\delta = 0.05$, $k_s = 0$.

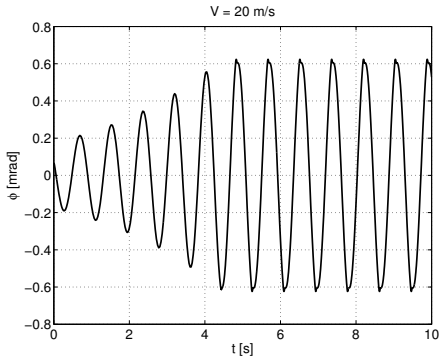

Figure B.29: $\phi(t)$, $\delta = 0.05$, $k_s = 0$.

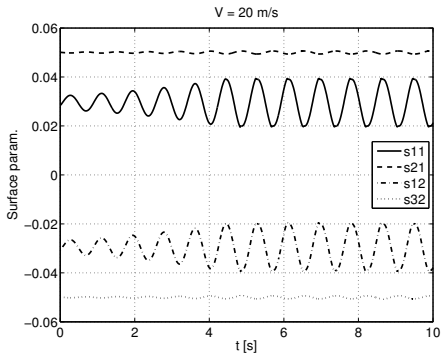

Figure B.30: $s_{ij}(t)$, $\delta = 0.05$, $k_s = 0$.

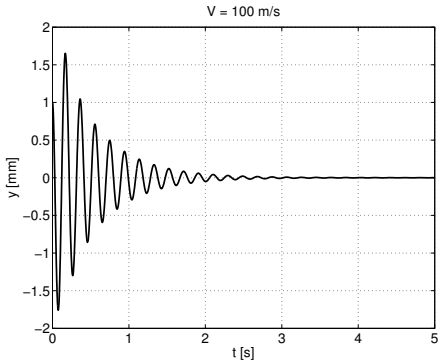

Figure B.31: $y(t)$, $\delta = 0.05$, $k_s = 1.823$ MN/m.

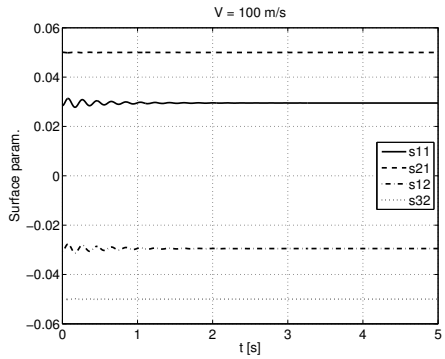

Figure B.32: $s_{ij}(t)$, $\delta = 0.05$, $k_s = 1.823$ MN/m.

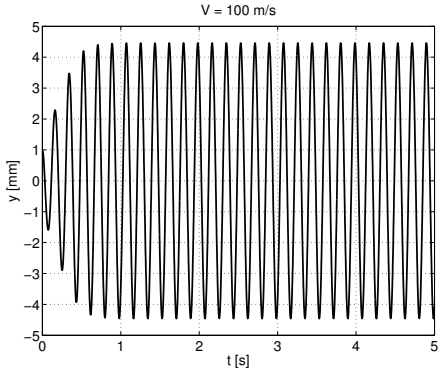

Figure B.33: $y(t)$, $\delta = 0.08$, $k_s = 1.823$ MN/m.

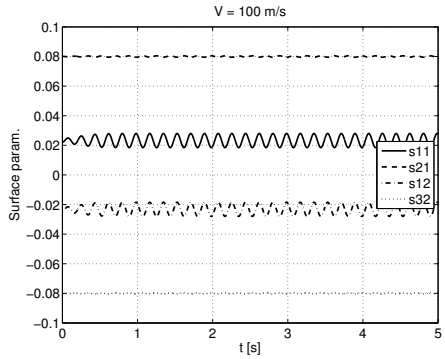

Figure B.34: $s_{ij}(t)$, $\delta = 0.08$, $k_s = 1.823$ MN/m.

Appendix C

Rotation matrices

The rotation matrices $\mathbf{A}_x^{(\alpha)}$, $\mathbf{A}_y^{(\alpha)}$ and $\mathbf{A}_z^{(\alpha)}$ are derived here. The angle α is defined to be positive in a counter–clockwise rotation.

Rotation around x

Consider the following coordinate systems

$$R_1 : (O_1; x_1, y_1, z_1) \qquad , \qquad R_2 : (O_2; x_2, y_2, z_2)$$

where R_2 is obtained by a counter–clockwise rotation of R_1 around x_1 with the angle α. The two bases are related by

$$\begin{aligned}
\mathbf{i}_1 &= (\mathbf{i}_1 \cdot \mathbf{i}_2)\mathbf{i}_2 + (\mathbf{i}_1 \cdot \mathbf{j}_2)\mathbf{j}_2 + (\mathbf{i}_1 \cdot \mathbf{k}_2)\mathbf{k}_2 = \mathbf{i}_2 \\
\mathbf{j}_1 &= (\mathbf{j}_1 \cdot \mathbf{i}_2)\mathbf{i}_2 + (\mathbf{j}_1 \cdot \mathbf{j}_2)\mathbf{j}_2 + (\mathbf{j}_1 \cdot \mathbf{k}_2)\mathbf{k}_2 = \cos\alpha\mathbf{j}_2 - \sin\alpha\mathbf{k}_2 \\
\mathbf{k}_1 &= (\mathbf{k}_1 \cdot \mathbf{i}_2)\mathbf{i}_2 + (\mathbf{k}_1 \cdot \mathbf{j}_2)\mathbf{j}_2 + (\mathbf{k}_1 \cdot \mathbf{k}_2)\mathbf{k}_2 = \sin\alpha\mathbf{j}_2 + \cos\alpha\mathbf{k}_2
\end{aligned}$$

$$\mathbf{A}_x^{(\alpha)} \equiv \mathbf{A}_{12} = \begin{bmatrix} 1 & 0 & 0 \\ 0 & \cos\alpha & -\sin\alpha \\ 0 & \sin\alpha & \cos\alpha \end{bmatrix}$$

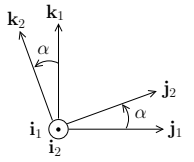

Rotation around y

Consider the following coordinate systems

$$R_1 : (O_1; x_1, y_1, z_1) \qquad , \qquad R_2 : (O_2; x_2, y_2, z_2)$$

where R_2 is obtained by a counter–clockwise rotation of R_1 around y_1 with the angle α.

$$\begin{aligned}
\mathbf{i}_1 &= (\mathbf{i}_1 \cdot \mathbf{i}_2)\mathbf{i}_2 + (\mathbf{i}_1 \cdot \mathbf{j}_2)\mathbf{j}_2 + (\mathbf{i}_1 \cdot \mathbf{k}_2)\mathbf{k}_2 = \cos\alpha \mathbf{i}_2 + \sin\alpha \mathbf{k}_2 \\
\mathbf{j}_1 &= (\mathbf{j}_1 \cdot \mathbf{i}_2)\mathbf{i}_2 + (\mathbf{j}_1 \cdot \mathbf{j}_2)\mathbf{j}_2 + (\mathbf{j}_1 \cdot \mathbf{k}_2)\mathbf{k}_2 = \mathbf{j}_2 \\
\mathbf{k}_1 &= (\mathbf{k}_1 \cdot \mathbf{i}_2)\mathbf{i}_2 + (\mathbf{k}_1 \cdot \mathbf{j}_2)\mathbf{j}_2 + (\mathbf{k}_1 \cdot \mathbf{k}_2)\mathbf{k}_2 = -\sin\alpha \mathbf{i}_2 + \cos\alpha \mathbf{k}_2
\end{aligned}$$

$$\mathbf{A}_y^{(\alpha)} \equiv \mathbf{A}_{12} = \begin{bmatrix} \cos\alpha & 0 & \sin\alpha \\ 0 & 1 & 0 \\ -\sin\alpha & 0 & \cos\alpha \end{bmatrix}$$

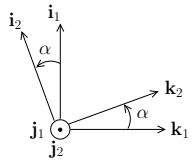

Rotation around z

Consider the following coordinate systems

$$R_1 : (O_1; x_1, y_1, z_1) \qquad , \qquad R_2 : (O_2; x_2, y_2, z_2)$$

where R_2 is obtained by a counter–clockwise rotation of R_1 around z_1 with the angle α.

$$\begin{aligned}
\mathbf{i}_1 &= (\mathbf{i}_1 \cdot \mathbf{i}_2)\mathbf{i}_2 + (\mathbf{i}_1 \cdot \mathbf{j}_2)\mathbf{j}_2 + (\mathbf{i}_1 \cdot \mathbf{k}_2)\mathbf{k}_2 = \cos\alpha \mathbf{i}_2 - \sin\alpha \mathbf{j}_2 \\
\mathbf{j}_1 &= (\mathbf{j}_1 \cdot \mathbf{i}_2)\mathbf{i}_2 + (\mathbf{j}_1 \cdot \mathbf{j}_2)\mathbf{j}_2 + (\mathbf{j}_1 \cdot \mathbf{k}_2)\mathbf{k}_2 = \sin\alpha \mathbf{i}_2 + \cos\alpha \mathbf{j}_2 \\
\mathbf{k}_1 &= (\mathbf{k}_1 \cdot \mathbf{i}_2)\mathbf{i}_2 + (\mathbf{k}_1 \cdot \mathbf{j}_2)\mathbf{j}_2 + (\mathbf{k}_1 \cdot \mathbf{k}_2)\mathbf{k}_2 = \mathbf{k}_2
\end{aligned}$$

$$\mathbf{A}_z^{(\alpha)} \equiv \mathbf{A}_{12} = \begin{bmatrix} \cos\alpha & -\sin\alpha & 0 \\ \sin\alpha & \cos\alpha & 0 \\ 0 & 0 & 1 \end{bmatrix}$$

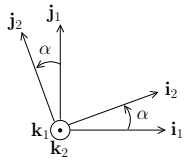

Inertial system to track system

1. Rotation around z by β_C (track yaw), $R_O \rightarrow R_{I1}$
2. Rotation around y_{I1} by θ_C (track gradient), $R_{I1} \rightarrow R_T$

$$\mathbf{A}_{OT} = \mathbf{A}_z^{(\beta_C)} \mathbf{A}_y^{(\theta_C)} \quad , \quad \mathbf{A}_{TO} = \mathbf{A}_{OT}^T$$

Track system to body system

1. Rotation around z_T by ψ (yaw), $R_T \rightarrow R_{I2}$
2. Rotation around y_{I2} by θ (pitch), $R_{I2} \rightarrow R_{I3}$
3. Rotation around x_{I3} by ϕ (roll), $R_{I3} \rightarrow R_b$

$$\mathbf{A}_{Tb} = \mathbf{A}_z^{(\psi)} \mathbf{A}_y^{(\theta)} \mathbf{A}_x^{(\phi)} \quad , \quad \mathbf{A}_{bT} = \mathbf{A}_{Tb}^T$$

Body system to wheel–rail contact system

1. Rotation around x_b by δ (contact angle), $R_b \rightarrow R_c$

$$\mathbf{A}_{bc} = \mathbf{A}_x^{(\delta)} \quad , \quad \mathbf{A}_{cb} = \mathbf{A}_{bc}^T$$

$$\begin{aligned}
\mathbf{A}_{OT} &= \mathbf{A}_z^{(\beta_C)} \mathbf{A}_y^{(\theta_C)} \\
&= \begin{bmatrix} \mathrm{c}\beta_C \mathrm{c}\theta_C & -\mathrm{s}\beta_C & \mathrm{c}\beta_C \mathrm{s}\theta_C \\ \mathrm{s}\beta_C \mathrm{c}\theta_C & \mathrm{c}\beta_C & \mathrm{s}\beta_C \mathrm{s}\theta_C \\ -\mathrm{s}\theta_C & 0 & \mathrm{c}\theta_C \end{bmatrix} \\
\mathbf{A}_{TiTj} &= \mathbf{A}_{TiO}\, \mathbf{A}_{OTj} \\
&= \begin{bmatrix} \mathrm{c}\theta_C^i \mathrm{c}\theta_C^j \mathrm{c}(\beta_C^i - \beta_C^j) + \mathrm{s}\theta_C^i \mathrm{s}\theta_C^j & \mathrm{c}\theta_C^i \mathrm{s}(\beta_C^i - \beta_C^j) & \mathrm{c}\theta_C^i \mathrm{s}\theta_C^j \mathrm{c}(\beta_C^i - \beta_C^j) - \mathrm{s}\theta_C^i \mathrm{c}\theta_C^j \\ -\mathrm{c}\theta_C^j \mathrm{s}(\beta_C^i - \beta_C^j) & \mathrm{c}(\beta_C^i - \beta_C^j) & -\mathrm{s}\theta_C^j \mathrm{s}(\beta_C^i - \beta_C^j) \\ \mathrm{s}\theta_C^i \mathrm{c}\theta_C^j \mathrm{c}(\beta_C^i - \beta_C^j) - \mathrm{c}\theta_C^i \mathrm{s}\theta_C^j & \mathrm{s}\theta_C^i \mathrm{s}(\beta_C^i - \beta_C^j) & \mathrm{s}\theta_C^i \mathrm{s}\theta_C^j \mathrm{c}(\beta_C^i - \beta_C^j) + \mathrm{c}\theta_C^i \mathrm{c}\theta_C^j \end{bmatrix} \\
\mathbf{A}_{Tb} &= \mathbf{A}_z^{(\psi)} \mathbf{A}_y^{(\theta)} \mathbf{A}_z^{(\phi)} \\
&= \begin{bmatrix} \mathrm{c}\psi \mathrm{c}\theta & \mathrm{c}\psi \mathrm{s}\theta \mathrm{s}\phi - \mathrm{s}\psi \mathrm{c}\phi & \mathrm{c}\psi \mathrm{s}\theta \mathrm{c}\phi + \mathrm{s}\psi \mathrm{s}\phi \\ \mathrm{s}\psi \mathrm{c}\theta & \mathrm{s}\psi \mathrm{s}\theta \mathrm{s}\phi + \mathrm{c}\psi \mathrm{c}\phi & \mathrm{s}\psi \mathrm{s}\theta \mathrm{c}\phi - \mathrm{c}\psi \mathrm{s}\phi \\ -\mathrm{s}\theta & \mathrm{c}\theta \mathrm{s}\phi & \mathrm{c}\theta \mathrm{c}\phi \end{bmatrix} \\
\mathbf{A}_{Tb}^{(\theta=0)} &= \mathbf{A}_z^{(\psi)} \mathbf{A}_x^{(\phi)} \\
&= \begin{bmatrix} \mathrm{c}\psi & -\mathrm{s}\psi \mathrm{c}\phi & \mathrm{s}\psi \mathrm{s}\phi \\ \mathrm{s}\psi & \mathrm{c}\psi \mathrm{c}\phi & -\mathrm{c}\psi \mathrm{s}\phi \\ 0 & \mathrm{s}\phi & \mathrm{c}\phi \end{bmatrix} \\
\mathbf{A}_{bc} &= \mathbf{A}_x^{(\delta)} \\
&= \begin{bmatrix} 1 & 0 & 0 \\ 0 & \mathrm{c}\delta & -\mathrm{s}\delta \\ 0 & \mathrm{s}\delta & \mathrm{c}\delta \end{bmatrix} \\
\mathbf{A}_{Tc} &= \mathbf{A}_{Tb}^{(\theta=0)}\, \mathbf{A}_{bc} \\
&= \begin{bmatrix} \mathrm{c}\psi & -\mathrm{s}\psi \mathrm{c}(\phi + \delta) & \mathrm{s}\psi \mathrm{s}(\phi + \delta) \\ \mathrm{s}\psi & \mathrm{c}\psi \mathrm{c}(\phi + \delta) & -\mathrm{c}\psi \mathrm{s}(\phi + \delta) \\ 0 & \mathrm{s}(\phi + \delta) & \mathrm{c}(\phi + \delta) \end{bmatrix}
\end{aligned}$$

Table C.1: Rotation matrices. Here, c = cos and s = sin.

$$
\begin{aligned}
\mathbf{A}_{OT} &\approx \begin{bmatrix} \mathrm{c}\beta_C & -\mathrm{s}\beta_C & \theta_C \mathrm{c}\beta_C \\ \mathrm{s}\beta_C & \mathrm{c}\beta_C & \theta_C \mathrm{s}\beta_C \\ -\theta_C & 0 & 1 \end{bmatrix} \\
\mathbf{A}_{T_i T_j} &\approx \begin{bmatrix} 1 & -(\beta_C^j - \beta_C^i) & \theta_C^j - \theta_C^i \\ \beta_C^j - \beta_C^i & 1 & 0 \\ -(\theta_C^j - \theta_C^i) & 0 & 1 \end{bmatrix} \\
\mathbf{A}_{Tb} &\approx \begin{bmatrix} 1 & -\psi & \theta \\ \psi & 1 & -\phi \\ -\theta & \phi & 1 \end{bmatrix} \\
\mathbf{A}_{Tb}^{(\theta=0)} &\approx \begin{bmatrix} 1 & -\psi & 0 \\ \psi & 1 & -\phi \\ 0 & \phi & 1 \end{bmatrix} \\
\mathbf{A}_{bc} &= \begin{bmatrix} 1 & 0 & 0 \\ 0 & \mathrm{c}\delta & -\mathrm{s}\delta \\ 0 & \mathrm{s}\delta & \mathrm{c}\delta \end{bmatrix} \\
\mathbf{A}_{Tc} &\approx \begin{bmatrix} 1 & -\psi \mathrm{c}(\phi+\delta) & \psi \mathrm{s}(\phi+\delta) \\ \psi & \mathrm{c}(\phi+\delta) & -\mathrm{s}(\phi+\delta) \\ 0 & \mathrm{s}(\phi+\delta) & \mathrm{c}(\phi+\delta) \end{bmatrix}
\end{aligned}
$$

Table C.2: Approximate rotation matrices. Here, c = cos and s = sin.

Appendix D

Linear complementarity problem

The formulation of the impact problem modelling the longitudinal clearance between the axle box and axle guidance is a linear complementarity problem (LCP). The general form of a LCP is given equation (D.1). The vectors $\mathbf{x}$ and $\mathbf{y}$ are the unknown quantities. Dantzig's algorithm, see [53, 6], for solving LCPs is presented in the following. It should be noted that, in the case of modelling a frictionless impact problem, the matrix $\mathbf{A}$ is positive semidefinite which is a sufficient condition for the algorithm to terminate with an unique solution. For an arbitrary matrix $\mathbf{A}$ there is no guarantee about the solvability.

$$\mathbf{y} = \mathbf{A}\mathbf{x} + \mathbf{b} \quad , \quad \mathbf{0} \leq \mathbf{x} \perp \mathbf{y} \geq \mathbf{0} \tag{D.1}$$

Dantzig's algorithm is in the class of pivoting methods for solving linear and quadratic programs. The pseudocode is given in Algorithm 4 together with the auxiliary functions in Algorithm 5 and 6. A very readable description of the algorithm can be found in [6]. About the algorithm notation: y_d means the d'th element in the vector $\mathbf{y}$, and $\mathbf{A}_{\mathsf{Cd}}$ means the vector obtained by extracting the rows corresponding to the indices in the set C from the d'th column in the matrix $\mathbf{A}$.

```
function [x, y] = lcp_dantzig(A, b)
x = 0
y = b
C = NC = ∅
while ∃d such that y_d < 0 do
  goon = true
  while goon do
    Δx = xdirection(A, d, C)
    Δy = AΔx
    [s, j] = maxstep(x, y, Δx, Δy, d)
    x = x + sΔx
    y = y + sΔy
    if j ∈ C then
      C = C − {j}
      NC = NC ∪ {j}
    else if j ∈ NC then
      NC = NC − {j}
      C = C ∪ {j}
    else
      C = C ∪ {j}
      goon = false
    end if
  end while
end while
```

Algorithm 4: Dantzig's algorithm.

```
function Δx = xdirection(A, d, C)
Δx = 0
Δx_d = 1
solve A_CC z = −A_Cd
Δx_C = z
```

Algorithm 5: xdirection.

```
function [s, j] = maxstep(x, y, Δx, Δy, d)
s = ∞
j = −1
if Δy_d > 0 then
  j = d
  s = −y_d/Δy_d
  for i ∈ C do
    if Δx_i < 0 then
      s′ = −x_i/Δx_i
      if s′ < s then
        s = s′
        j = i
      end if
    end if
  end for
  for i ∈ NC do
    if Δy_i < 0 then
      s′ = −y_i/Δy_i
      if s′ < s then
        s = s′
        j = i
      end if
    end if
  end for
end if
```

Algorithm 6: maxstep.

Appendix E

Source code

The source code of the programs developed are found on the attached CD–ROM in the directory `phdthesis/code`. The contents of this directory is shown in Table E.1.

Directory	Description
`code/daecont/`	Constrained wheel–rail contact example (MATLAB)
`code/freightwagon/`	Freight wagon model (`C++`, `Java`)
`code/guidrod/`	Guided rod example (MATLAB)
`code/impactosc/`	Impact oscillator example (`C++`)
`code/leafspring/`	Leaf spring example (MATLAB)
`code/sdirk/`	Integrator (`C++`)
`code/wrcon/`	Contact table scripts (MATLAB)

Table E.1: Source code overview.

Execute the following steps to compile and run the freight wagon simulator:

1. `./config_phd` (bash script for compilation)
2. `cd code/freightwagon` (change directory)
3. `make run` (Linux)
4. `gmake run` (Solaris)

Bibliography

[1] E. Andersson, M. Berg, and S. Stichel. *Rail Vehicle Dynamics*. Department of Vehicle Engineering, Royal Institute of Technology (KTH), Sweden, 2005.

[2] ARGECARE, `http://www.argecare.com`.

[3] J. Awrejcewicz, G. Kudra, and C.-H. Lamarque. Dynamical investigations of three coupled rods with a horizontal barrier. In *Meccanica*, volume 38, pages 687–698. Kluwer Academic Publishers, 2003.

[4] J. Awrejcewicz and C.-H. Lamarque. *Bifurcation and chaos in nonsmooth mechanical systems*, volume 45 of *A*. World Scientific, 2003.

[5] J. B. Ayasse and J. L. Maupu. *Dynamique ferroviaire en coordonnées curvilignes*, volume n^0 245. INRETS, 2003.

[6] D. Baraff. Fast contact force computation for nonpenetrating rigid bodies. In *Computer Graphics Proceedings, Annual Conference Series*. SIGGRAPH 94, July 1994.

[7] D. Cebon. *Handbook of vehicle–road interaction*. Swets & Zeitlinger, 1999.

[8] N. K. Cooperrider. The hunting behavior of conventional railway trucks. *ASME J. Eng. Industry 94*, pages 752–762, 1972.

[9] W. Deinert. *Eisenbahnwagen*. Transpress VEB Verlag für Verkehrswesen, 5. Auflage (1985) edition, 1967.

[10] M. di Bernardo *et al.* Bifurcations in nonsmooth dynamical systems. Preprint, `http://hdl.handle.net/1983/445`, 2005.

[11] E. Eich-Soellner and C. Führer. *Numerical methods in multibody dynamics.* B.G. Teubner Stuttgart, 1998.

[12] J. B. Ayasse *et al.* Computer simulation of freight vehicles with leaf springs; a comparison between four packages. Technical report, Institut National de Recherche sur les Transports et leur Sécurité (INRETS), 2001. INRETS/RE–01–046–FR.

[13] W. H. Enright, K. R. Jackson, S. P. Nørsett, and P. G. Thomsen. Interpolants for Runge–Kutta formulas. In *ACM Transactions on Mathematical Software*, volume 12, pages 193–218. ACM, 1986.

[14] P. S. Fancher, R. D. Ervin, C. C. MacAdam, and C. B. Winkler. Measurement and representation of the mechanical properties of truck leaf springs. *SAE Trans*, 1980. 800905.

[15] V. K. Garg and R. V. Dukkipati. *Dynamics of railway vehicle systems.* Academic Press, 1984.

[16] C. Glocker. On frictionless impact models in rigid–body systems. *The Royal Society*, pages 2385–2404, 2001.

[17] C. Glocker. *Set–valued force laws.* Springer-Verlag, 2001.

[18] G. Grabner and A. Kecskeméthy. Reliable multibody collision detection using Runge–Kutta integration polynomials. In *Multibody Dynamics 2003.* IDMEC/IST, 2003.

[19] G. Grabner, R. Kittinger, and A. Kecskeméthy. An integrated Runge–Kutta and polynomial root finding method for reliable event–driven multibody simulation. IFAC Workshop on Lagrangian and Hamiltonian Methods for Nonlinear Control, 2003.

[20] A. Grzelak. *Influence of wear of elements of UIC link suspension on ride dynamics of freight wagon on a straight track.* PhD thesis, Institut of Vehicles, Warsaw University of Technology, 2006.

[21] A. Grzelak and J. Piotrowski. Parametric identification of sub–models of a mathematical model of UIC link suspension with worn elements. In *Proc. of the 16^{th} international conference "Current problems in rail vehicles".* PRORAIL, 2003.

[22] E. Hairer, S. P. Nørsett, and G. Wanner. *Solving ordinary differential equations I; Nonstiff problems, Second revised edition.* Springer, 2000.

[23] E. Hairer and G. Wanner. *Solving ordinary differential equations II; Stiff and differential algebraic problems, Second revised edition.* Springer, 2002.

[24] W. Hanneforth and W. Fischer. *Laufwerke*. Transpress VEB Verlag für Verkehrswesen, 1986.

[25] H. Hertz. Über die Berührung zweier fester, elastischer Körper. *Journal für die reine und angewandte Mathematik*, 92:156–171, 1882.

[26] M. Hoffmann and D. E. Petersen. Dry friction and impact dynamics in railway vehicles. Master's thesis, Informatics and Mathematical Modelling, Technical University of Denmark, 2003.

[27] M. Hoffmann and H. True. On the dynamics of two–axle freight wagons with UIC standard suspension. In *Proc. of the 19^{th} IAVSD Symposium*. IAVSD, 2005.

[28] B. Hu and W. Schiehlen. Muti–time scale simulation for impact systems: From wave propagation to rigid body motion. In *Archive of Applied Mechanics*, volume 72, pages 883–898. 2003.

[29] B. Hu and R. Seifried. Impact induced vibrations and the loss of energy. In *Proc. of the 5^{th} international conference on vibration engineering*, pages 10–15, 2002.

[30] A. Iserles. *A first course in the numerical analysis of differential equations*. Cambridge University Press, 1996.

[31] A. D. Jensen. An object–oriented platform for dynamics simulation. Master's thesis, Informatics and Mathematical Modelling, Technical University of Denmark, 1994. IMM–EKS–1994–47.

[32] J. C. Jensen. *Teoretiske og eksperimentelle dynamiske undersøgelser af jernbanekøretøjer*. PhD thesis, Informatics and Mathematical Modelling, Technical University of Denmark, 1995. IMM–PHD–1995–9.

[33] JNI, `http://java.sun.com/j2se/1.5.0/docs/guide/jni/index.html`.

[34] A. Johansson. *Out–of–round railway wheels – causes and consequences*. Depertment of Applied Mechanics, Chalmers University of Technology, 2005.

[35] K. L. Johnson. *Contact mechanics*. Cambridge University Press, 1985.

[36] P.-A. Jönsson. *Modelling and laboratory investigations on freight wagon link suspensions, with respect to vehicle–track dynamic interaction*. PhD thesis, KTH Aeronautical and Vehicle Engineering, Royal Institute of Technology (KTH), Sweden, 2004. TRITA AVE 2004:48.

[37] P.-A. Jönsson and E. Andersson. Influence of link suspension characteristics of freight wagon lateral dynamics. In *Proc. of the 6^{th} international conference on railway bogies and running gears*, 2004.

[38] C. Kaas-Petersen. Chaos in a railway bogie. In *ACTA Mechanica*, volume 61, pages 89–108. Springer–Verlag, 1986.

[39] J. J. Kalker. *Three–dimensional elastic bodies in rolling contact*. G.M.L. Gladwell, Kluwer Academic Publishers, 1990.

[40] J. J. Kalker. Book of tables for the Hertzian creep–force law. In *Proc. of the 2^{th} MINI conference on contact mechanics and wear of rail/wheel systems*, pages 11–19. VSDIA, 1996.

[41] T. Kapitaniak and S. R. Bishop. *The Illustrated Dictionary of Nonlinear Dynamics and Chaos*. John Wiley & Sons, 1999.

[42] W. Kik. RSGEO and RSPROF programme for the simulation of the wheel/rail or the wheelset–roller kinematics, translated by J. Litzenberger. Technical report, Technical University of Denmark, 2000.

[43] W. Kik and J. Piotrowski. A fast, approximate method to calculate normal load at contact between wheel and rail and creep forces during rolling. In *Proc. of the 2^{nd} MINI conference on contact mechanics and wear of rail/wheel systems*, pages 52–61, 1996.

[44] K. Knothe and S. Stichel. *Schienenfahrzeugdynamik*. Springer–Verlag, 2003.

[45] M. R. Kristensen, J. B. Jørgensen, P. G. Thomsen, and S. B. Jørgensen. An ESDIRK method with sensitivity analysis capabilities. *Computers and Chemical Engineering*, 28:2695–2707, 2004.

[46] M. Kunze. *Non–Smooth Dynamical Systems*. Springer, 2000.

[47] A. Kværnø. Singly diagonally implicit Runge–Kutta methods with an explicit first stage. *Preprint : Numerics NO. 1*, 2004 . `http://www.math.ntnu.no/preprint/numerics/2004/N1-2004.ps`.

[48] K. Kämpfe. *Schwingungsverhalten eines zweiachsigen Eisenbahnfahrzeugs mit freien Lenkradsätzen und reibungsbehafteten Kopplungen beim Lauf im geraden Gleis*. PhD thesis, Fakultät für Maschinenwesen und Elektrotechnik der Technischen Hochschule München, 1960.

[49] Eung-Shin Lee. *Untersuchung des Entgleisungsverhaltens von Güterwagen mit Mehrkörpersystem (MKS)–Modell unter Berücksichtigung der COULOMBschen Reibung der geschichteten Blattfeder*. PhD thesis, Fakultät V – Verkehrs – und Maschienensysteme der Technischen Universität Berlin, 2003.

[50] R. I. Leine and H. Nijmeijer. *Dynamics and bifurcations of non–smooth mechanical systems*. Springer–Verlag, 2004.

[51] R. Mannshardt. One–step methods of any order for ordinary differential equations with discontinuous right–hand sides. In *Numerische Mathematik*, volume 31, pages 131–152. Springer–Verlag, 1978.

[52] J. J. Moreau. Unilateral contact and dry friction in finite freedom dynamics. *Nonsmooth Mechanics and Applications, Springer*, 302, 1988. CISM Courses and Lectures.

[53] K. G. Murty. *Linear complementarity, linear and nonlinear programming.* Heidermann–Verlag, Berlin, 1988.

[54] H. Netter. *Rad–Schiene–Systeme in differential–algebraischer Darstellung.* Fortschrittberichte VDI Reihe 12 Nr. 352, VDI Verlag, 1998.

[55] H. B. Nielsen. Cubic splines. Technical report, Informatics and Mathematical Modelling, Technical University of Denmark, 1998. J. No. H45.

[56] J. B. Nielsen. *New developments in the theory of wheel/rail contact mechanics.* PhD thesis, Informatics and Mathematical Modelling, Technical University of Denmark, 1998. IMM-PHD-1998-51.

[57] J.-P. Pascal. Oscillations and chaotic behaviour of unstable railway wagons over large distances. *Chaos, Solitons and Fractals*, 5(9):1725–1753, 1995.

[58] J. P. Pascal and G. Sauvage. New method for reducing the multicontact wheel/rail problem to one equivalent contact patch. In *Proc. of the 12th IAVSD Symposium*, pages 475–489. Swets & Zeitlinger, 1991.

[59] J. P. Pascal and G. Sauvage. The available methods to calculate the wheel/rail forces in non Hertzian contact patches and rail damaging. In *Vehicle System Dynamics*, volume 22, pages 263–275. Swets & Zeitlinger, 1993.

[60] F. Pfeiffer and C. Glocker. *Multibody dynamics with unilateral contacts.* John Wiley & Sons, 1996.

[61] J. Piotrowski. Model of the UIC link suspension for freight wagons. In *Archive of Applied Mechanics*, volume 73, pages 517–532. Springer–Verlag, 2003.

[62] J. Piotrowski. A new measurement method for determination of mechanical characteristics of pendulous systems with friction. In *3th international conference "Modelling and simulation of friction phenomena in physical and technical systems"*, 2004.

[63] J. Piotrowski and H. Chollet. Wheel–rail contact models for vehicle systems dynamics including multi–point contact. In *Vehicle System Dynamics*, volume 43, pages 455–483. Taylor & Francis, 2005.

[64] O. Polach. A fast wheel–rail force calculation computer code. In *Vehicle System Dynamics Supplement*, volume 33, pages 728–739, 1999.

[65] O. Polach and A. Vetter. Methods for running stability prediction and their sensitivity to wheel/rail contact geometry. In *Proc. of the 6^{th} international conference on railway bogies and running gears*, 2004.

[66] J. Pombo. *A multibody methodology for railway dynamics applications.* PhD thesis, Instituto Superior Téchnico, Universidade Técnica de Lisboa, 2004.

[67] K. Popp, K. Knothe, and C. Pöpper. System dynamics and long–term behaviour of railway vehicles, track and subgrade: Report on the dfg priority programme in germany and subsequent research. In *Vehicle System Dynamics*, volume 43, pages 485–538. Taylor & Francis, 2005.

[68] RAFIL, `http://www.rafil-gmbh.de/produkte/gueter/gueterw.htm`.

[69] Rail transport, `http://en.wikipedia.org/wiki/Railroad`.

[70] G. Sauvage and J. P. Pascal. Solution of the multiple wheel and rail contact dynamic problem. In *Vehicle System Dynamics*, volume 19. Swets & Zeitlinger, 1990.

[71] D. Schmidt. Parabelfedern für Schienenfahrzeuge. Technical report, Federnwerk, Langen & Sondermann GmbH & Co. KG . `http://www.langen-sondermann.de`.

[72] G. Schupp. *Numerische Verzweigungsanalyse mit Anwendungen auf Rad–Schiene–Systeme.* PhD thesis, Institut B für Mechanik der Universität Stuttgart, 2003. ISBN 3–8322–2935–3.

[73] A. A. Shabana. *Dynamics of multibody systems (second edition).* Cambridge University Press, 1998.

[74] A. A. Shabana, M. Berzeri, and J. R. Sany. Numerical procedure for the simulation of wheel/rail contact dynamics. *ASME*, 123:168–178, 2001.

[75] A. A. Shabana and J. R. Sany. An augmented formulation for mechanical systems with non–generalized coordinates: Application to rigid body contact problems. *Kluwer Academic Publishers, Nonlinear Dynamics*, 24:183–204, 2001.

[76] L. F. Shampine, Jr. R. C. Allen, and S. Pruess. *Fundamentals of numerical computing.* John Wiley & Sons, 1997.

[77] L. F. Shampine and S. Thompson. Event location for ordinary differential equations. Technical report, 2000 . `http://www.radford.edu/~thompson/webddes/ddeevt2.html`.

[78] Z. Y. Shen, J. K. Hedrick, and J. A. Elkins. A comparison of alternative creep force models for rail vehicle dynamics analysis. In *Proc. of the 8th IAVSD Symposium*, pages 591–605. Swets & Zeitlinger, 1983.

[79] E. C. Slivsgaard. *On the interaction between wheels and rails in railway dynamics*. PhD thesis, Informatics and Mathematical Modelling, Technical University of Denmark, 1995. IMM–PHD–1995–20.

[80] S. Stichel. Running behaviour of railway freight wagons with single–axle running gear – a parametric study. Technical report, Department of Vehicle Engineering, Royal Institute of Technology (KTH), Sweden, 1998. TRITA–FKT Rapport 1998:40.

[81] S. Stichel. How to improve the running behaviour of freight wagons with UIC–link suspension. In *Vehicle System Dynamics Supplement*, volume 33, pages 394–405. Swets & Zeitlinger, 1999.

[82] S. Stichel. On freight wagon dynamics and track deterioration. In *Proc. Instn. Mech. Engrs.*, volume 213. IMechE, 1999.

[83] S. Stichel. The influence of underframe structural flexibility on the hunting behaviour of a freight wagon. In *Computers in Railways*, pages 725–736, 2000.

[84] S. Stichel. Limit cycle behaviour and chaotic motions of two–axle freight wagons with friction damping. In *Multibody System Dynamics*, volume 8, pages 243–255. Kluwer Academic Publishers, 2002.

[85] M. Stiepel and S. Zeipel. Freight wagon running gears with leaf spring and ring suspension. Simpack user meeting presention, 2004 . `http://www.simpack.de/f4/s7/presentations04-pdf.html`.

[86] S. H. Strogatz. *Nonlinear dynamics and chaos*. Perseus Books, 1998.

[87] C. Studer and C. Glocker. Simulation of non–smooth mechanical systems with many unilateral constraints. In *Proc. 5th EUROMECH Non–linear Oscillations Conference, Eindhoven, August 7–12*, pages 1597–1606, 2005.

[88] T. Telliskivi, U. Olofsson, U. Sellgren, and P. Kruse. A tool and a method for FE analysis of wheel and rail interaction. Technical report, Royal Institute of Technology (KTH), Sweden . `http://www.md.kth.se/~ulfs/Publications/Pitt_5.pdf`.

[89] P. G. Thomsen. A generalized runge–kutta method of order three. Technical report, Informatics and Mathematical Modelling, Technical University of Denmark, 2002. IMM–REP–2002–07.

[90] P. G. Thomsen. Numerical solution of differential algebraic equations and applications. Technical report, Informatics and Mathematical Modelling, Technical University of Denmark, 2005. IMM–REP–2005–06.

[91] P. G. Thomsen. Discontinuities in ODE's – system with change of state. Technical report, Informatics and Mathematical Modelling, Technical University of Denmark, 2006. IMM–REP–2006–07.

[92] P. G. Thomsen and C. Bendtsen. Numerical solution of differential algebraic equations. Technical report, Informatics and Mathematical Modelling, Technical University of Denmark, 1999. IMM–REP–1999–08.

[93] H. True. Does a critical speed for railroad vehicles exist? In *ASME/IEEE joint railroad conference*, pages 125–131. ASME, 1994.

[94] H. True. On the theory of nonlinear dynamics and its applications in vehicle system dynamics. *Vehicle System Dynamics*, 31(5–6):393–421, 1999.

[95] H. True. Nichtlineare schienenfahrzeugdynamik, neue grundlagen, methoden und ergebnisse. *ZEVrail Glasers Annalen*, 128(11–12):526–537, 2004.

[96] H. True. Recent advances in the fundamental understanding of railway vehicle dynamics. *International journal of vehicle design*, 40(1–3):251–264, 2006.

[97] H. True and R. Asmund. The dynamics of a railway freight wagon wheelset with dry friction damping. *Vehicle System Dynamics*, 38:149–163, 2002.

[98] H. True, M. Hoffmann, and P.-A. Jönsson. The design and performance of the European freight wagon standard suspension. In *ASME International Mechanical Engineering Congress and Exposition*. ASME, 2005. IMECE2005–79227.

[99] H. True and P. G. Thomsen. On the problems of non–smooth railway vehicle dynamics. In *Multibody Dynamics 2005*. ECCOMAS Thematic Conference, 2005.

[100] L. Trzepacz. Railway freight vehicle dynamics. Master's thesis, Informatics and Mathematical Modelling, Technical University of Denmark, 2002. IMM–EKS–2002–48.

[101] J. D. Turner. On the simulation of discontinuous functions. *Journal of Applied Mechanics, ASME*, 68:751–757, 2001.

[102] P. J. Vermeulen and K. L. Johnson. Contact of nonspherical bodies transmitting tangential forces. *J. Appl. Mech.*, 31:338–340, 1964.

[103] A. H. Wickens. *Fundamentals of rail vehicle dynamics – guidance and stability*. Swets & Zeitlinger, 2003.

[104] F. Xia. *The dynamics of the three–piece–freight truck*. PhD thesis, Informatics and Mathematical Modelling, Technical University of Denmark, 2002. IMM–PHD–2002–104.

[105] F. Xia, C. Cole, P. Wolfs, and D. Roach. Three–dimensional geometrical contact between a wheel and rail. Technical report, Rail CRC, Department of Engineering and Physical Systems, Central Queensland University, Australia, 2003.

[106] E. Østergaard. Documentation for the SDIRK C++ solver. Technical report, Informatics and Mathematical Modelling, Technical University of Denmark, 1998.